Hyperon production in p-Be interactions at 158 GeV/c per nucleon at the WA97 CERN experiment

Paul Norman

Thesis submitted for the degree of

Doctor of Philosophy

Particle Physics Group,
School of Physics and Astronomy,
University of Birmingham

October, 1999.

Author's Contribution

The author's contribution to the WA97 and NA57 experiments can be broken down into two distinct categories. By far the larger of the two was the analysis effort for the WA97 experiment. In addition, the author also aided in the data taking of the NA57 experiment, which included a small amount of help with the setting up of the trigger.

Besides a little work on both the WA85 experiment and the WA97 Pb-Pb data, the bulk of the author's work revolved around the WA97 p-Be data, which can again be separated into two parts. The first of these was the writing and testing of the vertex finding program that would be used in the subsequent analysis, and the second was the analysis itself. The author began by working on the V^0 data, and then, once that was advanced enough, passed the final V^0 work onto colleagues. He then concentrated on the complete cascade analysis, its selection cuts, and the event weighting. This analysis culminated in the calculation of the yields and inverse slopes which are the standard results quoted by the WA97 experiment.

The author was also invited to represent the WA97 experiment at the international Moriond conference on "QCD and High Energy Hadronic Interactions". There he presented his results on behalf of the collaboration.

Synopsis

Strange particle production is one of the most useful probes of matter under extreme conditions of temperature and density. Due to the differences between quark masses in a Quark Gluon Plasma and hadron masses in a hadron gas scenario, there is a significant difference in the equilibration times for strange quark production under these two mechanisms. This difference in equilibration times will manifest itself in a much greater yield of strange particles from a QGP with respect to a hadron gas. It is believed that collisions of heavy ions at high energy may provide sufficient conditions for a QGP to be formed.

The aim of the WA97 experiment is, therefore, to investigate relativistic heavy ion collisions at the CERN OMEGA Spectrometer, following on from the work of the WA85 and WA94 collaborations. Using a lead ion beam from the CERN Super Proton Synchrotron and a lead target, data were taken in both 1995 and 1996. As a control, in the autumn of 1995, data were also taken using a proton beam incident on a lead target. In 1996 the control was changed to a proton beam incident on a beryllium target. Significant enhancements in strange particle yields had already been seen when going from the p-Pb data to the Pb-Pb data. However, the lack of symmetry in the p-Pb collisions could, in theory, give misleading results and so analysis of the more symmetric p-Be data was needed in order to confirm these enhancements. The analysis of the data from the 1996 proton-beryllium run therefore forms the basis of this thesis.

By observing the weak decays of the strange Λ, $\overline{\Lambda}$, Ξ^-, $\overline{\Xi}^+$, Ω^- and $\overline{\Omega}^+$ hyperons, the yields per interaction and transverse mass spectra can be determined. The results from the p-Be data are then compared with the results for the p-Pb and Pb-Pb data. The inverse slope parameters from the tranverse mass distributions give an indication of the temperature reached in the collisions, and a clear increase can be seen in this quantity as the size of the collision system increases. Yields are studied as a function of the number of nucleons participating in the collision, N_{part}, which is estimated using the Glauber model for the Pb-Pb data, and by averaging over impact parameter for the proton beam data. From the proton data to the Pb-Pb data, the yields per participant increase substantially. The enhancement is in agreement with QGP theory, in that it becomes more pronounced with the strangeness content of the particle, and exceeds an order of magnitude for the Ω.

Acknowledgements

First of all, I'd like to thank those three people who were most directly responsible for me getting to the stage of having a thesis to submit. My first thanks, therefore, go to my supervisor, Dr David Evans, and also to Professor John Kinson and Dr Orlando Villalobos Baillie. They helped make my PhD the most rewarding and enjoyable course that I have studied for and showed me that you can still get students to work, without standing over them and cracking a bullwhip.

From the other Physics group staff, I'd like to give thanks to Drs Andrew Kirk and Frank Votruba for their company during many entertaining evenings at CERN, and to Drs Lawrence Lowe and Steve Hall for their support in computer matters.

Thanks should go to those teachers and lecturers responsible for helping me get to the stage where I could do a PhD, or even a degree - from my first Science teacher, Mr Thomas, to my GCSE and A level teachers, Clive Bryan, Danny O'Brien, Ian Ward, Alan Bright, Graham Dibble, Ian Gover and Roger Bowden. Then, at University, I'd like to thank Dr Trevor Preist and the rest of the Theoretical Physics staff at Exeter University, who took me for my Undergraduate degree and Dr David Weaver of Birmingham, who was my tutor during my MSc in Nuclear Reactor Physics.

From outside of Birmingham I'd like to give thanks to Professor Emanuele Quercigh for his faith in me and for giving me the honour of representing our collaboration at a highly enjoyable international conference such as Moriond. My gratitude also goes out to Dr Håvard Helstrup, for help with much of the computer code that I used and wrote during my PhD.

A mention should also go to those fellow students who studied with me at Birmingham during my time here, most notably the other two students in the same year as me - Mike Thompson and Shaun Ashby - and to Mark Venables, who helped me to settle into the joys of Heavy Ion Particle Physics. The up and coming next generation of students have all settled in well and I'd like to wish the best of luck in their PhDs to Alun Lloyd, Dave Lamb and Carrie Goodwin.

Heartfelt thanks go to those friends of mine who don't actually live in Birmingham, but did their best to keep in touch with letters, phone calls, emails, and the occasional visit. So a big thank you to Maivelyn Lim, Karl Wraight, Jonathan Vincent and Francis Chiu.

Last, but by no means least, I'd like to thank my immediate family for their love and support during my PhD and all the years that led up to it. So deepest thanks to my parents and to my sister Alison for all of their efforts. They were much appreciated.

My sincerest thanks to everyone I've mentioned here, and to those many others who helped in smaller ways, but are too numerous to include in these Acknowledgements. Thank you,

Paul Norman, October 1999.

Contents

List of Figures

List of Tables

Chapter 1

The Quark-Gluon Plasma

1.1 Introduction

Since the dawn of time the Universe has posed countless questions that demanded answers. The most fundamental of these questions were "What is the Universe made of?", and "Which laws do its constituents obey?". In the early years of civilised man, the Ancient Greeks believed in the existence of an "Atom" - a single, indivisible particle, that could be the building block of the Universe. Many hundreds of years later, Mendeleev composed the periodic table of the elements, arranging each of the known elements into distinct groups in his table. It became clear that each of the "Atoms" in the table were composed of a positive and negative part, and many theories set about to explain this. The early "Plum Pudding" model, for example, suggested that the atom was composed of positive and negative particles, clustered into a pudding-like ball. After Rutherford's work in 1911, however, the existence of a positively charged nucleus orbited by negatively charged electrons was established. Later, the nucleus itself was found to be composed of protons and neutrons, which at the time were thought to be fundamental particles. Particle Physics emerged as the science that would search to find all truly fundamental particles, and the nature of the laws which they obeyed. Subsequent work in this field went on to show that these protons and neutrons (collectively known as nucleons) were not actually fundamental particles at all, and are themselves composed of sets of three quarks held together by gluons (particles which mediate the interaction between the quarks). The fundamental strong interaction is based at this level of quarks and gluons (or "partons", as they are collectively known). The actual forces which hold the nucleus together then arise naturally as residue interactions from one nucleon to another - in much the same way as Van der Waals forces act between atoms. Up until 10^{-5} seconds after the Big Bang, however, conditions of temperature and energy density were too extreme for matter to exist in this form. The theory of Quantum Chromodynamics (QCD) predicts that in this epoch (and perhaps even in the cores of neutron stars today) these extreme conditions give rise not to individual, well-defined nucleons, but to an unconfined "soup" of quarks and gluons in which the quarks are essentially free [1]. This phase of matter is known as the Quark-Gluon Plasma (QGP). Being a test of QCD theory, and also having implications for both the early Universe and astrophysics [2], the search to find and prove the existence of the QGP is, therefore, an interesting and wide-ranging branch of modern Particle Physics.

1.2 The Theory of QCD

1.2.1 The Prediction of the Quark-Gluon Plasma

When particle physicists found that protons and neutrons were composed of sets of three quarks, it was clear that in order to form these two different types of nucleon, it was necessary that two different types of quark, or $flavours$ existed. These two distinct quark flavours were given the names "up" (u) and "down" (d), with the up having a charge of $+\frac{2}{3}$ of the electronic charge and the down having a corresponding charge of $-\frac{1}{3}$. In this way, the positively charged proton could be made up of two u quarks and a d quark, for a net charge of $+1$, and the uncharged neutron could be composed of one u quark and two d quarks. Anti-matter revealed the existence of corresponding anti-quarks

($\overline{u}$ and $\overline{d}$) and further insights into quark matter also revealed that heavier quark flavours existed - each of which had a charge of $+\frac{2}{3}$ or $-\frac{1}{3}$. A summary of the mass and charge of the six known quarks is given in table 1.1. More will be said on the dynamical and current masses later in this chapter.

Table 1.1: Quark charges and masses

Quark Flavour	Q/|e|	Spin	Dynamical mass	Current mass
u (up)	$+\frac{2}{3}$	$\vec{\frac{1}{2}}$	$m_u \sim m_d \sim 350$ MeV/c^2	$m_u \sim m_d \sim 6$ MeV/c^2
d (down)	$-\frac{1}{3}$	$\vec{\frac{1}{2}}$		
s (strange)	$-\frac{1}{3}$	$\vec{\frac{1}{2}}$	$m_s \sim 550$ MeV/c^2	$m_s \sim 150$ MeV/c^2
c (charm)	$+\frac{2}{3}$	$\vec{\frac{1}{2}}$	$m_c \sim 1.8$ GeV/c^2	$m_c \sim 1.4$ GeV/c^2
b (bottom)	$-\frac{1}{3}$	$\vec{\frac{1}{2}}$	$m_b \sim 5.3$ GeV/c^2	$m_b \sim 4.8$ GeV/c^2
t (top)	$+\frac{2}{3}$	$\vec{\frac{1}{2}}$	Not determined	$m_t \sim 174$ GeV/c^2

The existence of the Δ^{++} baryon, with its spin of $\frac{3}{2}$, required quarks to have another property or "quantum number". It was composed of three u quarks, which gave the correct charge. Its spin of $\frac{3}{2}$, however, required that all three of these quarks had their spins aligned - which was in apparent contradiction to the Pauli Exclusion Principle, which states that no two fermions (ie. particles with half-integer spin) can have the same quantum numbers if they have the same wave function. This problem was overcome by the suggestion that quarks had a further degree of freedom, which was given the name "colour" to distinguish the different types. In this way a bayron (three quark state) can be made up of a red, green, and blue quark for an overall colour which is white, and a meson (a bound state of a quark and an anti-quark) can be composed of a colour and its own anti-colour - also for a net colour which is white.

In the field theory of electromagnetic interactions, known as Quantum Electrodynamics (QED) [3], the electromagnetic interaction between charges is carried by particles known as *photons*. The photons themselves do not carry charge, however, and so do not interact with other photons. The interaction which holds quarks together is known as the "strong interaction" and occurs not between conventional charge, but between this so called "colour charge" of the quarks. The field theory which describes these strong interactions is known as Quantum Chromodynamics (QCD) and its force-carrier is not the photon, but the *gluon* [4]. It differs from QED in that QCD is "non-Abelian", the implication of which is that gluons themselves carry colour charge and so can also interact with other gluons (and even themselves).

The electromagnetic potential between two charges can be written as

$$V_{em} = -\frac{\alpha_{em}}{r}$$

with

$$\alpha_{em} = \frac{q_1 q_2}{4\pi\epsilon_0}$$

where α_{em} is the electromagnetic coupling constant for the charges q_1 and q_2. Likewise, the colour potential between two quarks can be written as [5]

$$V_s = -\frac{4}{3}\frac{\alpha_s}{r} + kr$$

where α_s is the strong coupling constant, r is the distance between the quarks, and k is a constant determined by experiment. Now, at distances of the order of 1 fm and above it is the linear term which dominates and is analogous to a thin flux tube of colour, or "string", in which the tension increases as the quarks are pulled apart [4]. Since the force which results from a potential is given by

$$F = \frac{-\partial V}{\partial r}$$

this linear term, therefore, gives rise to a *constant* force once it starts to dominate. Therefore it takes an infinite amount of energy to separate the two quarks and so the principle of quark *confinement* arises naturally as a consequence of the colour potential.

Another interesting difference between QED and QCD arises when one considers the effect of *charge screening*. In QED, an electron is constantly emitting and reabsorbing photons, which can themselves convert into electron-positron pairs. Since the positrons will be attracted to the initial electron, and the electrons repelled from it, this has the net effect of directly surrounding the electron with positrons from the vacuum. A test charge sitting some distance from the electron will therefore see an electron of lower charge because of this nearby cloud of positrons. However, a test charge which is able to penetrate more closely (ie. of higher Q^2) will be able to pass through the positron cloud and so see a much enhanced charge of the electron. In QCD a similar thing can occur, with gluons converting into a $q\overline{q}$ pair and, indeed, the two scenarios would be identical were it not for the fact that a gluon can itself convert into two gluons while a photon cannot convert directly into two photons. A single quark is, therefore, not only surrounded by $q\overline{q}$ pairs from the QCD vacuum but also by gluon pairs which has the net effect that a quark with a red colour charge becomes preferentially surrounded by a cloud of other red colour charges. This is shown in figure 1.1.

The implication for a test charge is, therefore, the complete opposite of QED because a test colour charge will see enhanced colour when it lies some distance from the quark but the colour then becomes reduced when sufficient Q^2 is present to penetrate the surrounding cloud and see only the bare colour of the original quark [6]. The variation with charge strength as a function of distance for both a bare electron and a bare quark are shown in figure 1.2.

The implication of this aspect of QCD is that at sufficiently high temperature and density, the colour force between quarks becomes so small that they can behave as essentially non-interacting free particles. Therefore, if the conditions are extreme enough, the quarks should lose their confinement and a phase transition to a "new" form of matter should occur [7, 8]. This "new" form of matter is known as the Quark-Gluon Plasma (QGP).

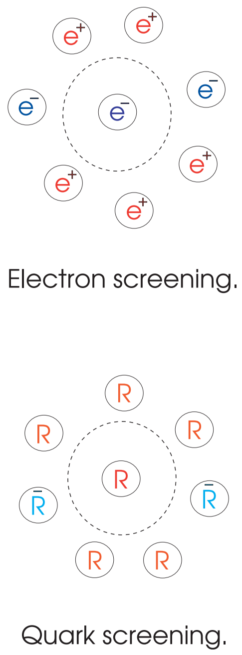

Figure 1.1: Schematic diagram of electron screening (top) and screening of a bare quark (bottom).

1.2.2 The Phase Diagram of QCD

Since certain temperatures and densities can induce the phase change from normal hadronic matter to the QGP, there effectively exists a phase diagram of QCD in temperature and baryon density space. This phase diagram could be seen as analogous to that of a liquid which becomes gaseous under certain conditions of varied temperature and pressure. Figure 1.3 shows a schematic representation of the QCD phase diagram, including the high temperature/low baryon density early Universe [1] and the low temperature/high density area of neutron stars [2]. Experimentally, the easiest way to reproduce the conditions of the QGP should be through the collision of heavy ions at high energy. Such collisions should provide both the high temperatures and energy densities required to get close to, and hopefully past, the QGP phase boundary. Also shown schematically in figure 1.3 are the approximate positions of current and planned heavy ion experiments - RHIC (Relativistic Heavy Ion Collider) at Brookhaven, and the CERN experiments at the SPS

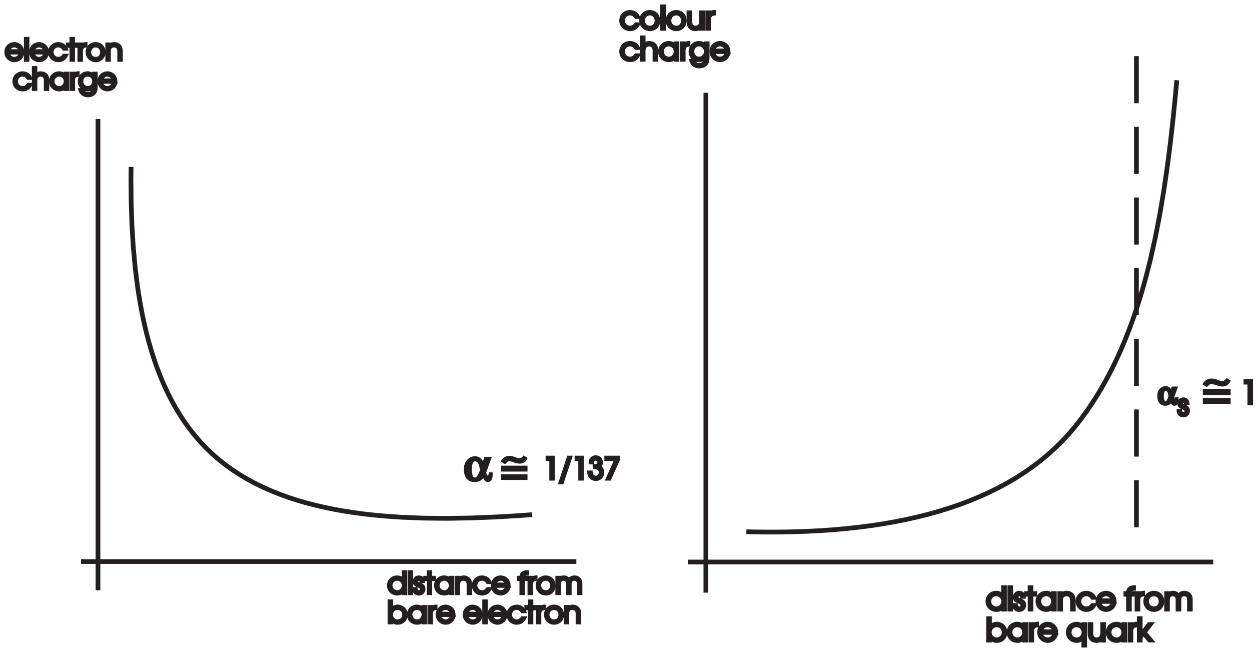

Figure 1.2: The effective charge as a function of distance for a bare electron (top) and a bare quark (bottom).

(Super Proton Synchroton) and ALICE (A Large Ion Collider Experiment) at the LHC (Large Hadron Collider).

1.2.3 The Partial Restoration of Chiral Symmetry

Before electroweak symmetry breaking, the standard model Lagrangian contains only kinetic terms and can be written as [9]

$$\mathcal{L}_0 = i\overline{\psi}\partial\!\!\!/\psi$$

This form of the Lagrangian exibits a property known as *chiral symmetry*, since it can be expanded into separate right-handed and left-handed terms

$$\mathcal{L}_0 = i\overline{\psi}_L\partial\!\!\!/\psi_L + i\overline{\psi}_R\partial\!\!\!/\psi_R$$

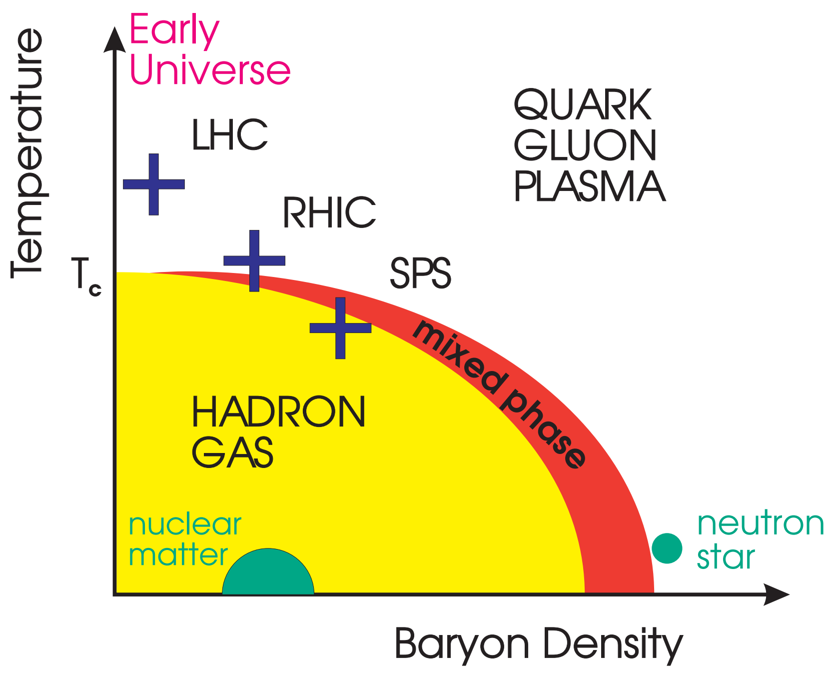

Figure 1.3: Phase diagram in the Temperature-Density plane.

Breaking of electroweak symmetry generates a mass term ($\overline{\psi} m \psi$) in the Lagrangian, however, which removes the chiral symmetry because this mass term contains mixed right and left-handed parts

$$\mathcal{L} = \mathcal{L}_0 + m(\overline{\psi}_L \psi_R + \overline{\psi}_R \psi_L)$$

If this new term were to go to zero, then that would remove it from the Lagrangian, thus restoring the chiral symmetry. While this does not happen exactly, the symmetry can be partially restored by decreasing the value of m, the quark mass, such that the mass term in the Lagrangian is small. This is possible in the Quark-Gluon Plasma because the mass of a quark effectively has two parts, the first part of which is its inherent mass which comes from interactions with the Higgs field (the *current* quark mass) and the second part is caused by the surrounding medium (much like an electron has an "effective mass" when it is trying to move through a solid). Since quarks should behave as essentially non-interacting free particles in conditions of high temperature and density, this second part of the quark mass should go to zero, reducing the quark mass from its dynamical mass to its current mass and thus partially restoring chiral symmetry in the QGP.

1.3 Heavy Ion Kinematics

Experimentally, forming the conditions of high temperature and density in which the QGP is expected to be formed is carried out with a lead ion beam incident upon a lead target (as in the current WA97 [10] and NA57 [11] experiments) although future experiments such as ALICE plan to use the collision of two ion beams [12]. Out of the multitude of events produced by such collisions, only those which are *central* (as opposed to peripheral) are likely to have enough overlap between the two colliding nuclei to produce conditions of sufficient temperature and energy density to form a QGP (see figure 1.4). For this reason these are the events which are selected out, or "triggered" on, by the experiment. In such collisions of heavy ions the colliding ions move through each other and a central fireball region is formed where the temperature and energy density is greatest. In general, heavy ions are preferable to lighter ions because they create denser conditions and larger fireballs which then tend to live longer. These central fireballs are predicted to have lifetimes of the order of 10^{-23} seconds [13]. After this period, formation of hadrons (hadronisation) will occur once the temperature and density have fallen sufficiently via processes such as thermal expansion and, later, by pion emission.

When attempting to validate any apparent phenomenon in physics, or indeed science in general, it is almost invariably necessary to prove new results against a scientific control and attempting to prove the existence of the QGP is no exception. For this reason, heavy ion experiments have also performed runs with proton beams on the same fixed targets as used for the collisions of heavy nuclei, since the proton beam should not generate sufficient conditions of baryon density for a QGP to be formed. A number of experiments (including

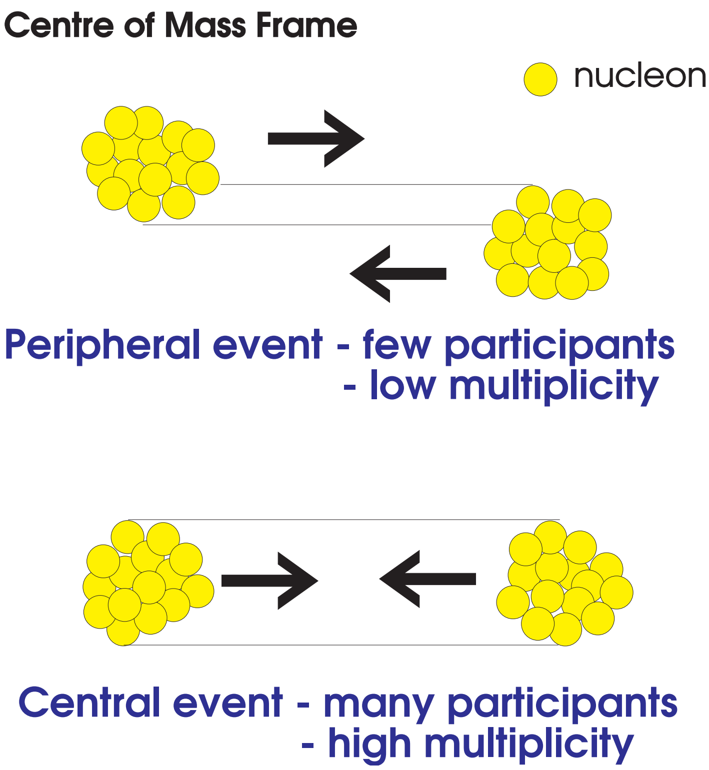

Figure 1.4: The difference between central and peripheral events.

WA97) have also performed proton control runs with light hydrogen or beryllium targets, because this creates a much more symmetric collision system than in proton-lead.

1.4 Signatures of a QGP

The evolution of a QGP with time is shown in figure 1.5. After the QGP phase the system continues to expand while going through a mixed phase and, from there, into a hadron gas (which is the point at which normal hadronic collisions should begin). The observed particles are then produced during hadronisation so it is imperitive that any useful signature of the QGP involves quantities which either remain constant or change very little during hadronisation. At $\sim 5 \times 10^{-23}$ seconds, the lifetime of the QGP fireball is comparable to the lifetime for strong interaction processes, but shorter than that for weak or electromagnetic interactions. This means that any quantum numbers which are conserved in the strong interaction (eg. strangeness) will also be conserved in the central fireball, because weak or electromagnetic interactions cannot occur during the timescale for which it exists. For this reason, signatures which rely on quantities such as strangeness and charm tend to be used. Likewise, particles such as leptons and photons can also prove to be good signatures since they do not couple to the strong interaction and, therefore, emerge unchanged from the hadronisation process. Unfortunately, they also tend to be plagued by significant background from hadronic decays. What follows is a brief description of the most promising QGP signatures together with a collection of the more significant results.

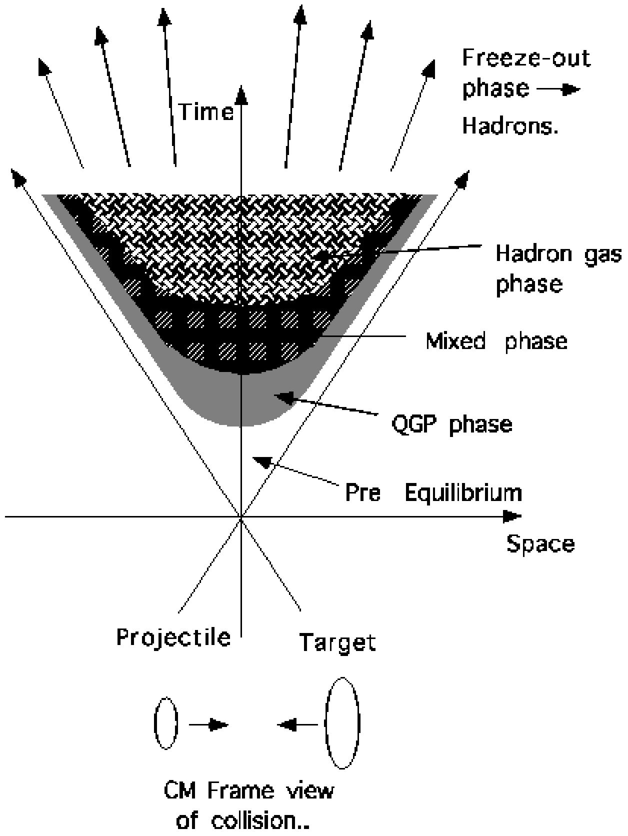

Figure 1.5: Evolution of a QGP in space and time.

1.4.1 Strangeness Enhancement

Since the onset of the QGP should bring about the partial restoration of chiral symmetry, the energy required to produce an $s\bar{s}$ pair in the plasma is approximately 300 MeV in a QGP scenario. Therefore, in typical temperatures of about 200 MeV a number of first order Feynmann diagrams should readily produce $s\bar{s}$ pairs in the plasma. These first order diagrams are shown in figure 1.6. In addition, u and d quark production should be initially surpressed by Pauli blocking [14] due to the many u and d quarks present in the original ions. Strangeness is conserved by the strong interaction, so a signature of strange hadrons should be observable after the plasma cools and hadronises.

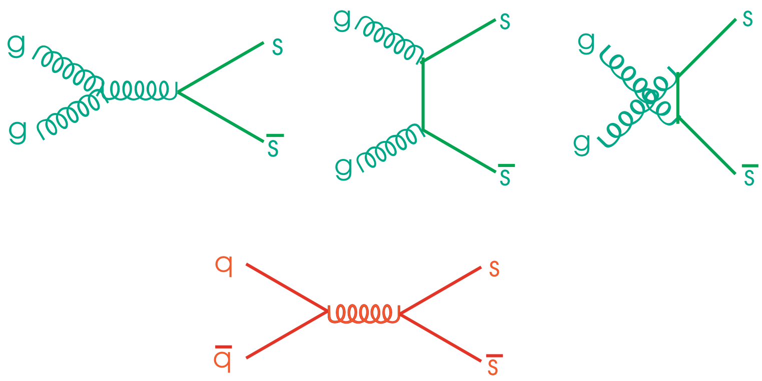

Figure 1.6: Strangeness producing interactions in a QGP.

Strangeness production need not by itself be conclusive evidence for a QGP, however, because strange particles may also be produced from a hadron gas phase. In a QGP phase though, strangeness chemical equilibrium will be reached (or very nearly reached) by the time the fireball cools and the hadronisation process starts. This is not the case in a hadron gas fireball, however, because in a hadron gas the production of particles occurs on the level of hadrons, not quarks. This means that for a particle like the triply-strange

Ω, a lot of energy is required for production.

The production of strange hadrons in a hadron gas phase is *via* reactions of the type $h_1 + h_2 \rightarrow$ hadrons. Some examples of such interactions that occur between the nucleons of the target and projectile are

$$pp \rightarrow pK^+\Lambda,$$

$$pp \rightarrow ppK^+K^-$$

and

$$pp \rightarrow pp\Lambda\overline{\Lambda}.$$

Further (secondary) interactions, such as

$$\pi^- p \rightarrow \Lambda K^0$$

and

$$\pi^+\pi^- \rightarrow K^+K^-$$

can also contribute to the overall strangeness production. The distinctions that need to be made between the hadron gas and QGP phases, however, are the two different strangeness production mechanisms and the fact that in a hadron gas phase the limits on the lowest threshold centre-of-mass energies for production of the various particles is considerably larger than that for the production of $s\bar{s}$ pairs in the QGP (for Λs this threshold is 670 MeV and for $\overline{\Lambda}$s it is 2.23 GeV *via* the first and third reactions respectively). This means that the time required for strangeness production to saturate in a hadron gas will be much longer than in a QGP and should be much longer than the lifetime of the fireball

[15]. A much greater yield of certain particles (in particular, the heavy, multistrange baryons such as the Ξ and Ω) would, therefore, only be expected from the QGP phase [7, 13]. In hadronic interactions it also becomes progressively more difficult to form these multistrange hyperons, so with this mechanism Ωs should be enhanced less than Ξs, which should in turn be enhanced less than Λs. In contrast, in a QGP, Ωs should be enhanced more than the Ξs, which should in turn be enhanced more than the Λs.

Because of the much greater yield of strange quarks from QGP interactions, several enhanced yields and ratios should be observed when compared with hadronic interactions. The many $s\overline{s}$ pairs created should lead to an increase in the number of s quarks relative to u and d quarks, and more significantly the number of $\overline{s}$ quarks relative to $\overline{u}$ and $\overline{d}$ (since, unlike u and d, there are no $\overline{u}$ and $\overline{d}$ present to begin with). Of course, experimentally these enhancements of strangeness will be observeable via the strange hadrons which are formed once the fireball cools. Most significant among these are the strange hyperons consisting of the singly-strange Lambda (Λ), the doubly-strange Xi (Ξ), and the triply-strange Omega (Ω) particle.

The author's collaboration, WA97, has studied the yields of strange hyperons as a function of the number of nucleons participating in the collision [16]. Figure 1.7 shows the yields per interaction of Λs, Ξs and Ωs for the WA97 p-Pb and Pb-Pb data where the Pb-Pb data have been split into four centrality bins to provide four different Pb-Pb points on the plot. The yields re-scaled so that the p-Pb data points are equal to 1 are shown in the second part of this figure. The solid line has a gradient of one and, therefore, shows where data would be expected to lie if the yields simply scaled with the number of participants. The Pb-Pb data shows a significant enhancement with respect to the p-Pb data for all hyperon species and, in particular, that the enhancement follows a distinct hierarchy such that it increases with the strangeness content of the particle (ie. the enhancement of Ωs is greater than the enhancement of Ξs, which is greater than the enhancement of Λs).

In order to view this enhancement more clearly the normalised yields can be divided

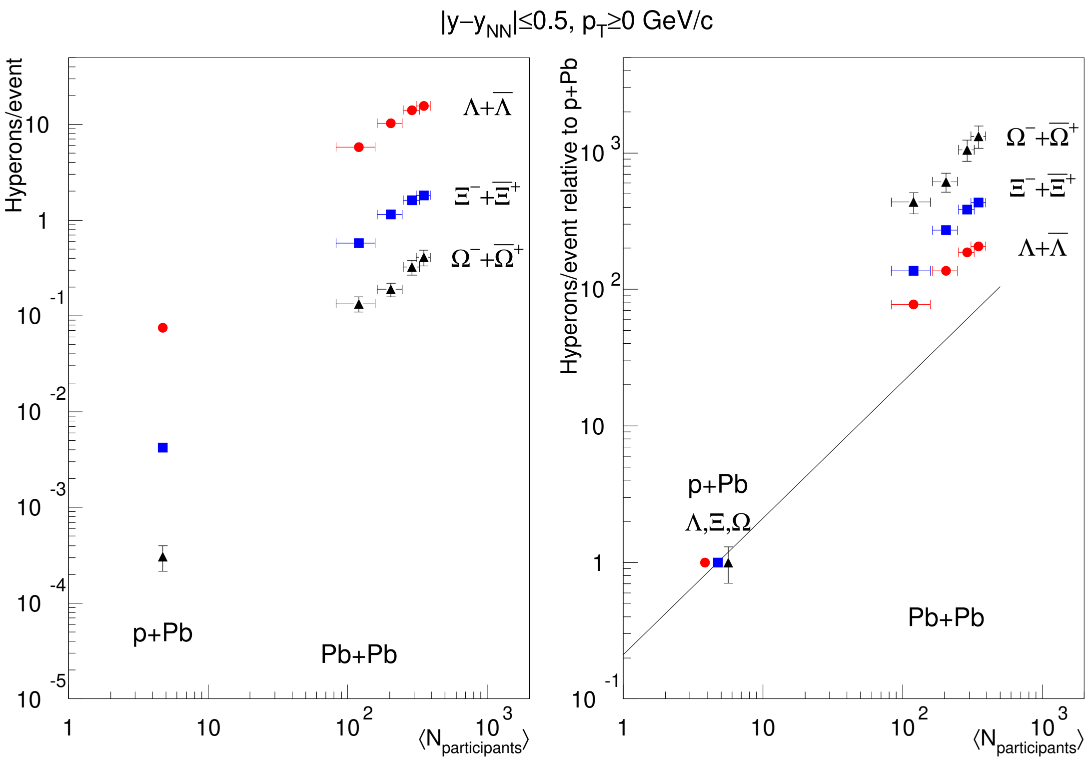

Figure 1.7: Hyperon yields per interaction (left), and hyperon yields per interaction rescaled so that the p-Pb value is 1 (right).

by the number of participants in which case the solid line in figure 1.7 maps onto a flat line at yield per participant = 1. This plot is shown in figure 1.8. The enhancement of Ξs in Pb-Pb (with respect to p-Pb) in this plot is by just over a factor of five, and for Ωs the enhancement exceeds an order of magnitude.

Also of some interest are transverse mass distributions and (where normalised yields are not available) particle ratios because these are related to the conditions of the fireballs in which they are produced. Typical ratios studied are $\frac{\Xi}{\Lambda}$, $\frac{\overline{\Xi}}{\overline{\Lambda}}$, $\frac{\Omega}{\Xi}$, $\frac{\overline{\Omega}}{\overline{\Xi}}$ and also the particle to anti-particle ratios $\frac{\overline{\Lambda}}{\Lambda}$, $\frac{\overline{\Xi}}{\Xi}$ and $\frac{\overline{\Omega}}{\Omega}$ [17, 18, 19]. The transverse mass distributions give an inverse slope parameter which is closely related to the temperature and for this reason it is a useful means of comparing the temperatures reached in collisions of different types and determining at what stage in the fireball cooling different particles are produced.

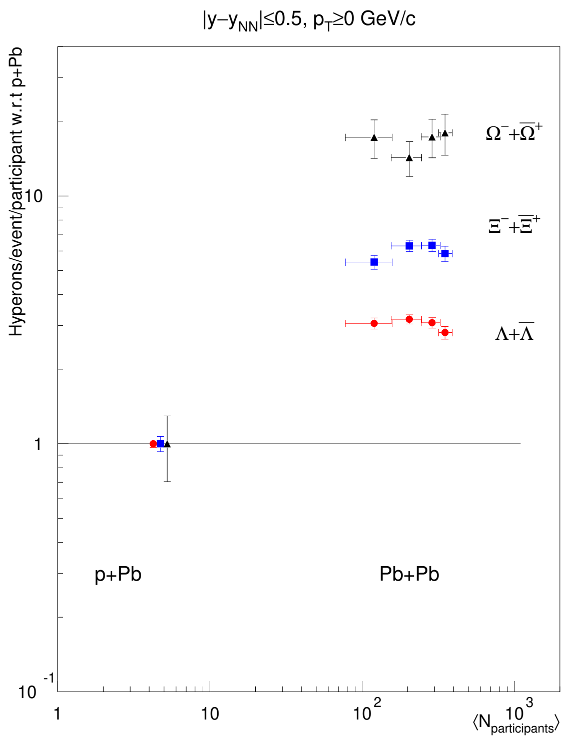

Figure 1.8: Hyperon yields per interaction, normalised to the p-Pb values and divided by the number of participants.

1.4.2 J/Ψ and Ψ′ Suppression

It has been predicted that the conditions of high baryon density which exist in the QGP are such that the formation of certain states which have large bound state radii (such as the J/Ψ or Ψ′) should be suppressed [20]. This is caused by the colour-screening of the quark and anti-quark by other strongly interacting matter in the high-density plasma, meaning that they effectively do not "see" each other and can, therefore, drift off to form other states such as D mesons. The Ψ′ has a slightly larger bound state radius and so is expected to be suppressed even more than the J/Ψ.

The NA38 [21] and NA50 [22] collaborations identify the J/Ψ and Ψ′ resonances through their decays into muon pairs. The number of events of each type are obtained from the analysis of the muon pair invariant mass spectrum, taking into account production from open charm decays and combinatorial background. Figure 1.9 shows the invariant mass spectrum of opposite-sign muon pairs obtained from the NA50 Pb-Pb data.

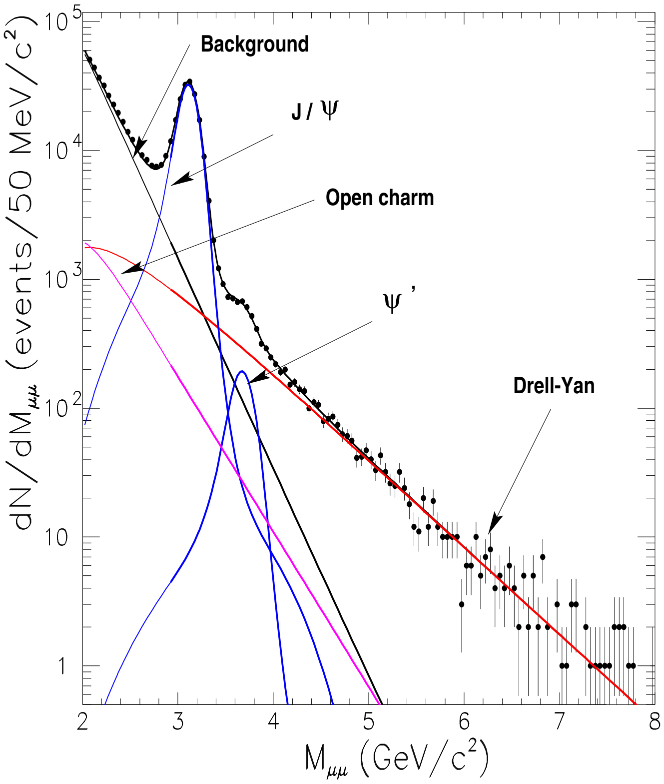

Figure 1.9: Opposite-sign muon pair invariant mass spectrum for Pb-Pb collisions at 158 GeV/c incident momentum.

The quantity which both the NA38 and NA50 collaborations calculate is $B_{\mu\mu}\sigma_{J/\Psi}/\sigma_{DY}$, which is the ratio of J/Ψ to Drell-Yan cross-sections, multiplied by the branching ratio of the J/Ψ into two muons. If the production of J/Ψ becomes suppressed, this quantity will therefore also be decreased. Figure 1.10 shows a plot of $B_{\mu\mu}\sigma_{J/\Psi}/\sigma_{DY}$ as a function of centrality for the NA50 Pb-Pb data, with the solid line showing the prediction from the Gerschel-Hüfner model [23] for ordinary nuclear absorption. As more central collisions are reached, a definite suppression of the J/Ψ with respect to light nuclei is observed. It has, however, been suggested by theorists that a suppression of the J/Ψ in this region could be caused by melting of the χ state, which would therefore require *two* dips in the observed curve for Pb-Pb collisions. It is as yet unclear whether or not this is the case.

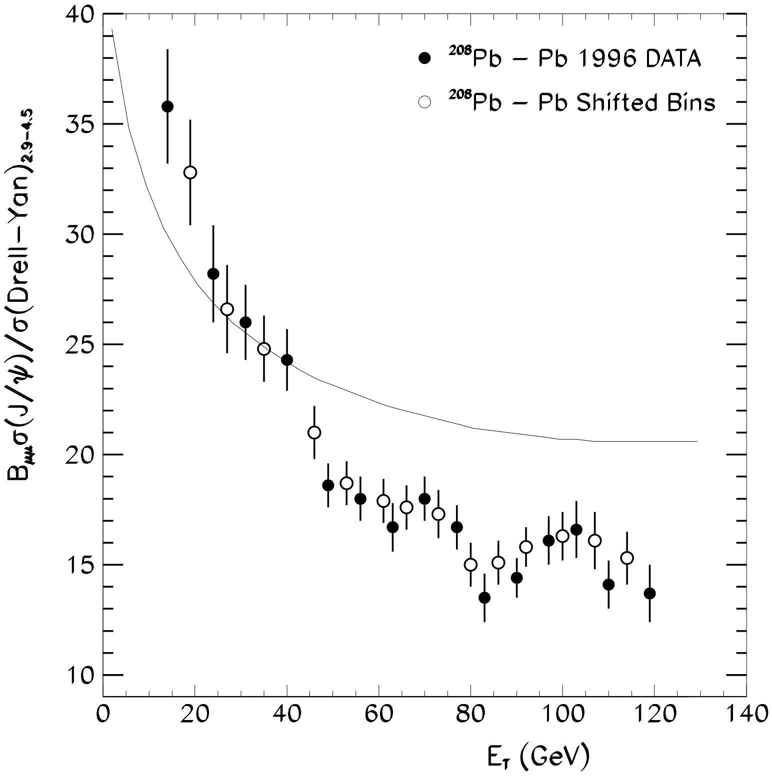

Figure 1.10: Ratios of J/Ψ to Drell-Yan cross-sections as a function of centrality in Pb-Pb collisions at 158 GeV/c per nucleon.

1.4.3 Direct Photons

Along with dileptons, direct photons are one of only two possible QGP signatures which can reach the detector directly because, once they are created, the timescale for the electromagnetic interaction prevents them from interacting in the much shorter lived plasma [24, 25]. The principal methods of producing photons in the plasma are through the annihilation of quarks and anti-quarks

$$q\overline{q} \rightarrow \gamma g$$

or via quark-gluon interactions

$$gq \rightarrow \gamma q$$

Unfortunately, such processes tend to be swamped by background from meson decays, such as

$$\pi^0 \rightarrow 2\gamma$$

and

$$\eta \rightarrow 2\gamma \quad or \quad 3\pi^0$$

Although experiments in the current energy range have shown little change in the direct photon production for hadron gas and QGP scenarios, it is expected that under conditions where the temperature reached in the fireball greatly exceeds the critical temperature for a QGP, direct photons should become much more dominant. Such conditions should be created in heavy ion collisions at the LHC and the ALICE photon spectrometer is being built with the intention of measuring this effect. Thus far, direct photon experiments have only been able to place upper limits on the numbers of photons per event as a function of p_T. Figure 1.11 shows such a plot from the WA80 collaboration [26]. The only real conclusion that can be made from the WA80 data is that the upper limits, shown with arrows, are consistant with the predictions from various theoretical models. While this shows that there is not a huge discrepancy between theory and experiment, further work is needed to draw more concrete conclusions from this field of inquiry.

1.4.4 Dileptons

Being particles which interact only via the weak and electromagnetic interactions, leptons should, in principle, be a good probe of a QGP [21, 27]. However, the study of single lepton production struggles against a large background from a series of hadronic decays. Searching for high energy lepton pairs appears to be much more promising however. Dileptons are produced via the Drell-Yan mechanism

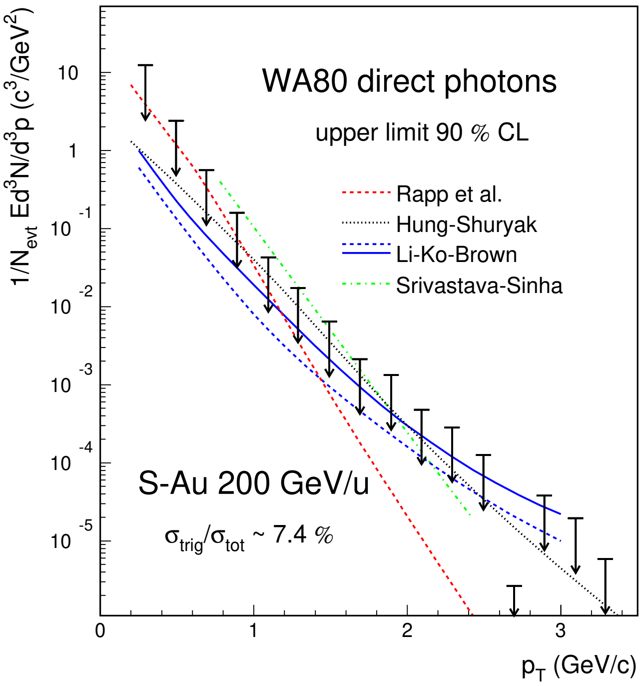

Figure 1.11: The upper limits placed on the yields of direct photons by the WA80 experiment, shown against the various theoretical predictions.

$$q\overline{q} \rightarrow l^+l^-$$

for which the main background comes through pion annihilation although this is much reduced with respect to the single lepton background. The NA45/CERES collaboration [28] have taken data with Pb-Au interactions and compared them to data from proton-proton interactions. When these data are normalised, by considering the number of charged particles per event, the Pb-Au data shows a clear excess in the yield of e^+e^- pairs in the effective mass range between 0.4 and 0.7 GeV/c^2. A plot showing the effective mass of e^+e^- pairs, along with the expected yields from the various decay modes, is shown in figure 1.12. Just as with the results from charmonium suppression, there is clearly an effect seen in the heavy ion data but it is not completely clear what the implications of this are in terms of the QGP. One suggestion is that because of the partial restoration of chiral symmetry mentioned earlier in this chapter, the mass of the ρ meson (which has a dynamical mass of 0.77 GeV/c^2) becomes shifted to a lower value in the QGP. Since the ρ has a fairly broad width (and hence a short lifetime) it should decay before it can escape the plasma and will, therefore, give rise to an enhanced yield of dileptons in the reduced mass region.

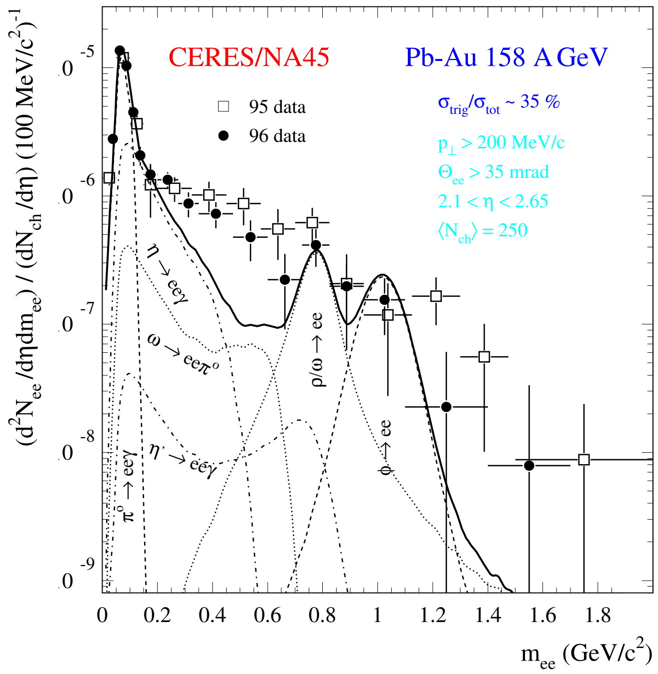

Figure 1.12: Yields of e^+e^- pairs normalised to the number of charged particles per event, and plotted as a function of the e^+e^- effective mass.

1.4.5 Entropy per Baryon

As one moves to a QGP scenario, the gluons present can give rise to a large increase in the number of degrees of freedom of the system. In turn, this gives rise to a large increase in S, the entropy of the system. A lattice QCD calculation was performed to calculate S/B, the entropy per baryon, for a system of three quark flavours in both the hadron gas and QGP scenarios. It was found that the QGP system had a value of S/B that was at least twice as large as that for a hadron gas [29].

Experimentally, S/B is difficult to measure but can be inferred from other experimental observeables. By measuring the multiplicities of positively and negatively charged particles (N^+ and N^-), it can be assumed that the baryon number is the difference between the two and the entropy the sum, giving a formula for S/B of

$$\frac{S}{B} = \frac{N^+ + N^-}{N^+ - N^-}$$

This measurement was effectively carried out by the EMU05 collaboration [30] when they measured the charge asymmetry D_Q, given by

$$D_Q = \frac{N^+ - N^-}{N^+ + N^-}$$

which, given the definition above, is of course the inverse of the entropy per baryon. The charge asymmetry was found to be 0.088 ± 0.007 which cannot be reproduced by current hadronic models. The NA57 experiment plans to make a further measurement of the entropy per baryon at two different beam energies once its data have been fully processed [11].

1.4.6 Strangelets

It has been proposed that Strange Quark Matter (SQM or strangelets) might also be formed in a QGP [31, 32]. Work from Witten *et al* [33] has shown that this Strange Quark Matter may be inherently more stable than ordinary nuclear matter [34]. Indeed, a series of bag model calculations have shown that droplets of nuclear matter of relatively low baryon number may be stable. Although a multitude of such objects could exist, the simplest is the H^0 dibaryon, a six quark object consisting of two up, two down and two strange quarks. Although the search for the H^0 has thus far given null results, heavy ion collisions at the CERN fixed target experiments provide an ideal environment in which to search for such particles. Some details will be presented in the following chapters, where a brief description of a search for the H^0 decay into $\Lambda\Lambda$ in S-W interactions is described.

1.5 The Aims of the WA97 and NA57 Experiments

To compare and contrast the yield of strange particles from the QGP and hadron gas phases, the WA97 and NA57 collaborations run under several different beam conditions. The basic heavy ion mode of running takes the form of a 158 GeV/c per nucleon (33 TeV total) lead beam incident on a lead target. These runs should include interactions where a QGP may be formed. A proton run on a lead target was also taken as a "control" because these interactions should not form a QGP. Therefore, one would expect a definite enhancement in the strange particle yields from Pb-Pb data (when compared with p-Pb data) if a QGP is produced in Pb-Pb interactions. The Omega group at Birmingham have also been involved in the previous West Area experiments WA85 [35] and WA94 [36]. These experiments have already shown an enhancement of Ξs by a factor of three going from proton-ion to ion-ion interactions. Both experiments used a normalisation to the number of negative hadrons produced from the two different types of collisions. The WA97 experiment has used the number of participating nucleons as a means of normalizing its different data sets. Data taken with a lead target has shown an enhancement of Ξs by just over a factor of five going from p-Pb to Pb-Pb and for Ωs the enhancement exceeds an order of magnitude. However, because the p-Pb is not a symmetric collision system, analysis of a more symmetric control sample is desirable. Therefore, a further control of a proton beam on a beryllium target was also used because this corresponds very closely to proton-proton interactions (which are difficult to do because they require a very thick target which then gives problems with vertex finding). In fact two out of every three p-Be collisions involve only two participating nucleons so the approximation to proton-proton interactions is a good one. The bulk of this thesis concentrates on the analysis of the WA97 p-Be data and then compares the results with the p-Pb and Pb-Pb data, some of the results of which have been briefly described in this chapter.

1.6 Summary

QCD theory suggests that under sufficient conditions of temperature and energy density a "new" phase of matter, the Quark-Gluon Plasma, should be formed. Collisions of ultra-relativistic heavy ions could provide the conditions necessary to prove the existence of a QGP through one of the predicted signals, one of the most promising of which is strangeness enhancement. The previous experiments, WA85 and WA94 have already shown evidence of strangeness enhancement from the ratios of Ξ and Λ particles (with Ξs enhanced by a factor of three in ion-ion interactions). The WA97 and NA57 collaborations have performed runs with even heavier (lead) ions (with p-Pb as a control). Current results from WA97 show an enchancement of Ξs by just over a factor of five going from p-Pb to Pb-Pb, and for Ωs the enhancement exceeds an order of magnitude. Current theory cannot explain this by a hadron gas phase alone. It is, however, very desirable to compare the Pb-Pb data with a more symmetric control system than p-Pb, and for this reason analysis of the p-Be data is essential, to see if it confirms the same level of enhancement that was seen with respect to the p-Pb data. The following chapters concentrate on the p-Be analysis.

Chapter 2

The WA97 Experiment

2.1 Introduction

The WA97 [10] and NA57 [11] experiments are designed to investigate the central fireball region created in ultra-relativistic heavy ion interactions. The aim is to search for a phase transition from normal hadronic matter to a QGP. Although this was also true of the previous WA85 [35] and WA94 [36] experiments, which used sulphur beams, the advent of lead beams at CERN has enabled WA97 and NA57 to study the interactions of truly heavy nuclei. WA97 has now finished its experimental running time and is in the analysis stage. NA57 has only just started its experimental run and has yet to begin data analysis. It will, therefore, be mentioned only briefly in this thesis.

In order to observe the phenomenon of strangeness enhancement, it is also neccessary to run a control version of the experiment. Thus both experiments run with a Pb beam on a Pb target and also with a proton beam on a Pb target. In Pb-Pb interactions the energy density in central events may be great enough to form a QGP, whereas in p-Pb the excited nuclear matter should not be able to form a QGP. Thus an enhanced yield of strange and multistrange baryons (and anti-baryons) should be observed if QGP formation occurs in the Pb-Pb collisions. The Weak (ie. flavour changing) decays are the ones both experiments concentrate on. Specifically, the channels

$$\Lambda(uds) \rightarrow p\pi^-,$$

$$\Xi^-(dss) \rightarrow \Lambda\pi^-,$$

$$\Omega^-(sss) \rightarrow \Lambda K^-,$$

and those of the corresponding anti-particles. Detecting such decays amongst the 1000 or so charged tracks produced in a central Pb-Pb interaction would be extremely difficult. However, the WA97 and NA57 experiments make use of only a small phase space window in transverse momentum (p_T) and rapidity (Y). Particles produced in the central fireball tend to come out at all angles in the centre of mass and so should be preserved when a relatively high p_T cut ($p_T > 0.5$ GeV/c) is made. The rapidity Y is a kinematic variable defined as

$$Y = \frac{1}{2} ln \frac{E + p_L}{E - p_L}$$

where E and p_L are the energy and longitudinal momentum of the particle respectively. Rapidity essentially gives a measure of how forward a particle is in the centre of mass. Figure 2.1 shows an idealised schematic diagram of an ultra-relativistic heavy ion collision in the centre of mass frame. It also shows how different regions of the collision relate to the rapidity $Y^* = Y_{CM}$. The NA49 experiment covers a wide range of rapidity and so looks at participants and spectators from the beam and target, as well as particles produced in the central region. To obtain much greater statistics and identification of strange and multistrange baryons, WA97 and NA57 concentrate on only the central rapidity range $\mid Y - Y_{NN} \mid \leq 0.5$, where Y_{NN} is central rapidity for the nucleon-nucleon system. This therefore concentrates on identifying those particles produced from the central fireball region only.

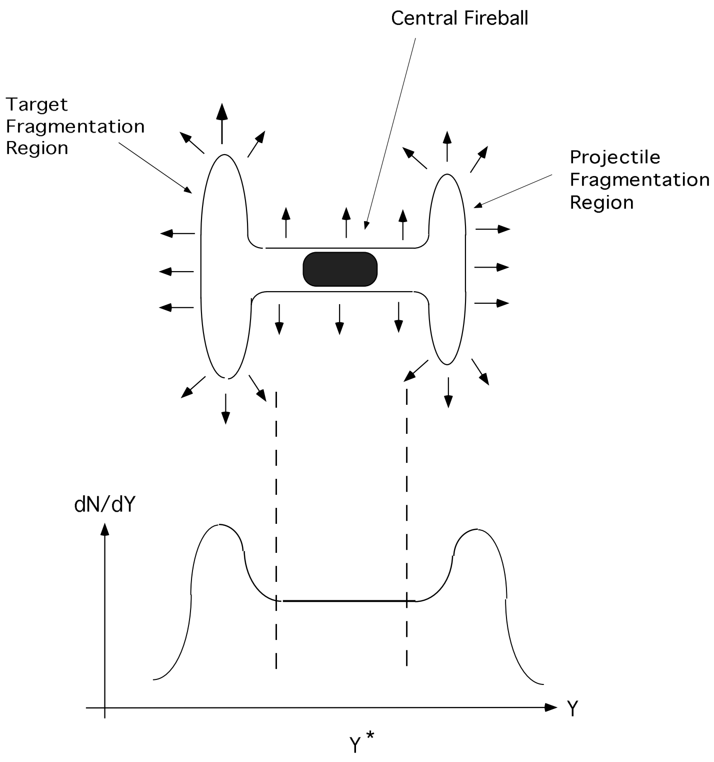

Figure 2.1: Schematic diagram showing a heavy-ion collision and the particle multiplicity as a function of rapidity in the centre of mass frame.

2.2 Beam

The CERN Super Proton Synchroton (SPS) produces a beam of protons with momentum 450 GeV/c. The Pb beam has momentum 158 GeV/c per nucleon, and so the SPS proton beam is focused into a beryllium target in order to give a proton beam which is also 158 GeV/c. These beams are then passed through a series of quadrupole and dipole magnets to select those beam particles of the correct momenta, and then on to the lead or beryllium target in the OMEGA (WA97) or GOLIATH (NA57) spectrometers.

2.3 The OMEGA Spectrometer

The OMEGA spectrometer consists of a superconducting magnet whose two Helmholtz coils produce a magnetic field of 1.8 T. The target and most of the detectors for track identification sit inside the 36 m^2 region of field produced by the magnet. Lead and proton data were taken for both field polarities. Although the system is symmetric, reversing the field is important to reduce residual systematic errors in the fine alignment of the detectors.

A useful system of co-ordinates is that which is defined relative to the centre of the OMEGA spectrometer. In this system the beam crosses the $x = 0$ cm ($x_\Omega = 0$ cm) plane at $y_\Omega = 0$ cm and $z_\Omega = -0.5$ cm. The beam travels along the x-axis of this system. The main component of the magnetic field is in the OMEGA z-direction.

2.4 The Target

The position of the lead target for the Pb-Pb data was $x_\Omega = -60$ cm. For the 1995 lead run the target thickness was chosen to be 1 % of an interaction length. This corresponds to a thickness of ~ 400 μm. For the proton beam data the position of the lead and beryllium targets was $x_\Omega = -90$ cm and had a thickness of 8 % of their respective interaction lengths. For the beryllium target this corresponded to a thickness of approximately 3.2 cm.

2.5 Detector Descriptions

In WA97, detectors were used for two different purposes [37], tracking and triggering. Figure 2.2 shows the experimental layout for the 1995 Pb run. A number of beam counters, namely V2, S2, S4 and VØ, are used to trigger on the desired beam signal. Multiplicity detectors are then used to trigger on central events and the tracks themselves are identified

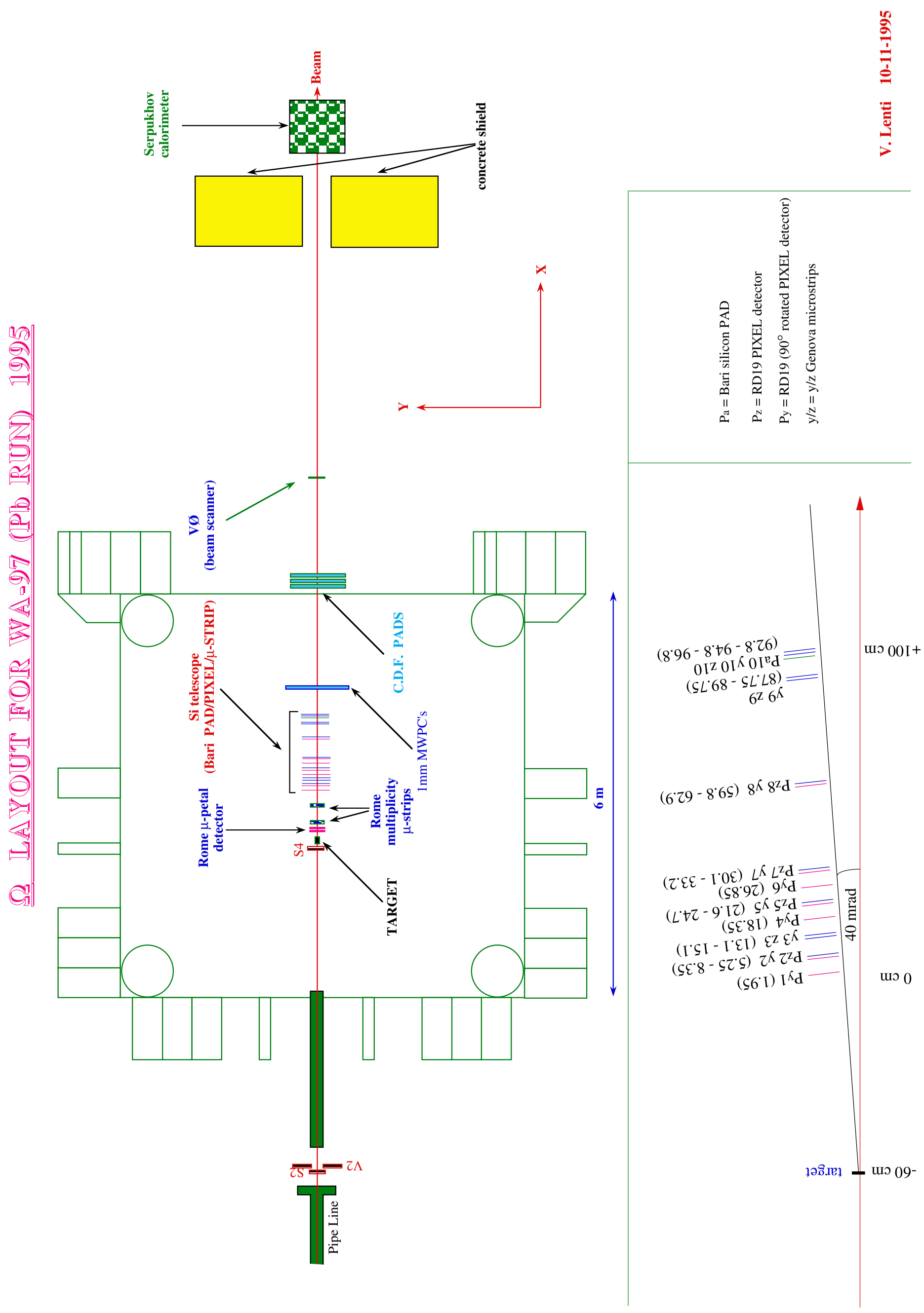

Figure 2.2: WA97 experimental layout for Pb-Pb data taking.

in a silicon telescope which points back to the interaction point.

The experimental layout for the 1996 p-Be run is shown in figure 2.3. The most noteable change is the addition of the beam microstrips. The petal detectors are used for triggering in high multiplicity interactions such as Pb-Pb and so do not play a role as such in the much lower multiplicity proton beam data. The same can also be said of the multiplicity microstrips which sample the charged track multiplicity, since the multiplicity is so low in p-Be or even p-Pb collisions.

The silicon telescope is composed of pixel planes [38, 39] and silicon microstrips with a 50 μm pitch. Figure 2.4 shows a view looking down the silicon telescope at reconstructed tracks in a no-field event. The magnetic field actually points in the z direction, and so charged particles bend in the xy plane. Since the apparatus is symmetric in the bend direction, the geometrical acceptance is the same for both particles and anti-particles.

2.5.1 Silicon Pixel Detectors

The basic building block of the WA97 pixel detectors is the ladder. Each silicon pixel plane consists of two arrays, each containing six ladders. The two arrays are mounted several millimetres apart but, because of overlap between the ladders, the whole 5cm $\times$ 5cm array is covered with sensitive material. The layout of such a plane is shown in figure 2.5. Each ladder consists of 96 columns and 64 rows of rectangular diodes (the pixels), which have been ion-implanted on a high-resistivity n-type silicon substrate. The pixels are 500 μm $\times$ 75 μm in size. Also, each ladder has six chips, each containing 16 x 64 pre-amplifier cells (ie. one per pixel). Each of these cells contains a front-end amplifier followed by a comparator with an adjustable threshold, adjustable delay line, and some coincidence and memory elements, which are used to store the bit indicating that a particle hit has occurred during a time frame determined by an external strobe.

Since each ladder contains $96 \times 64 = 6144$ pixels, and there are 12 ladders in all, this corresponds to over 70,000 pixels per plane. Of course because the pixels themselves

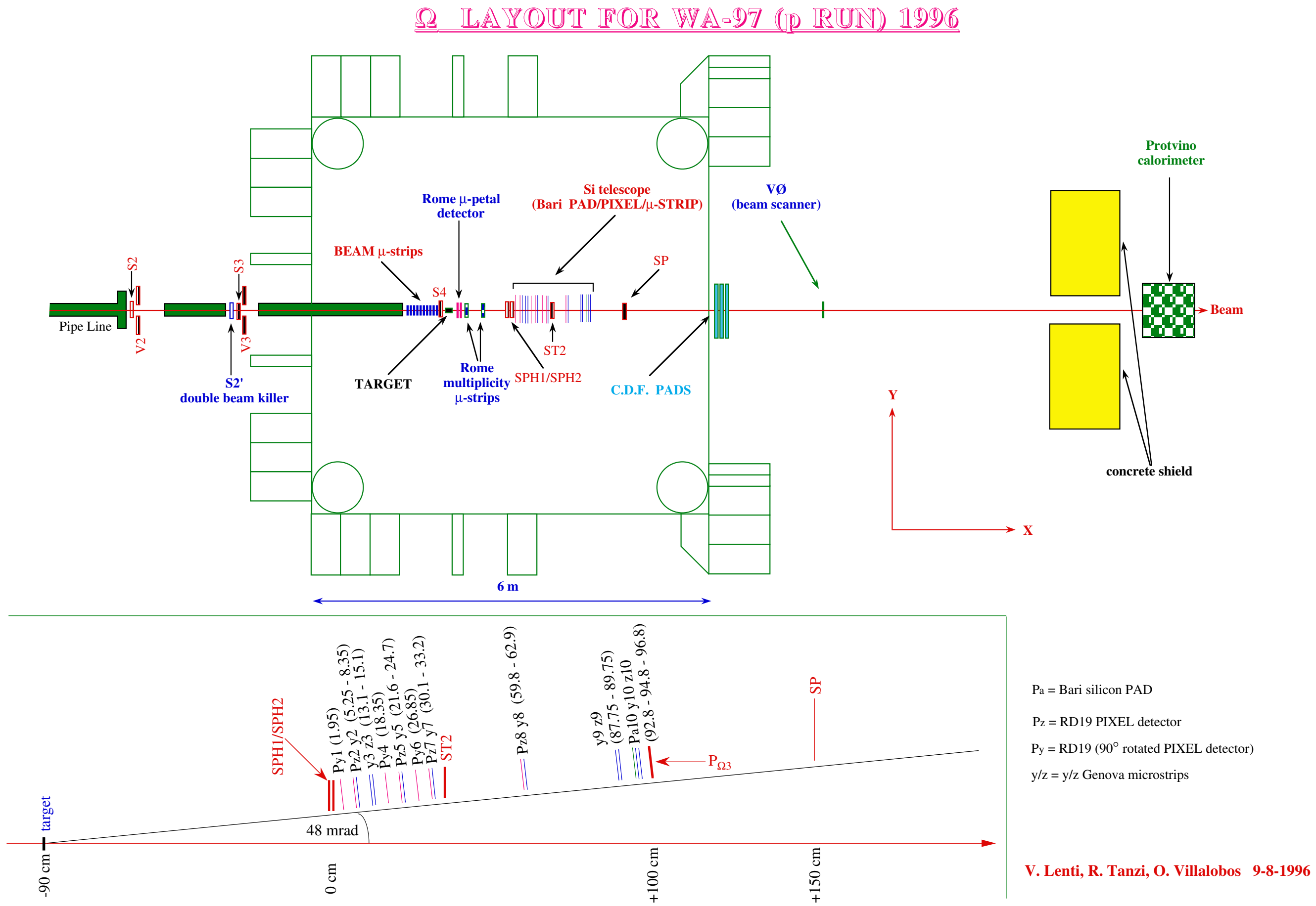

Figure 2.3: WA97 experimental layout for p-Be data taking.

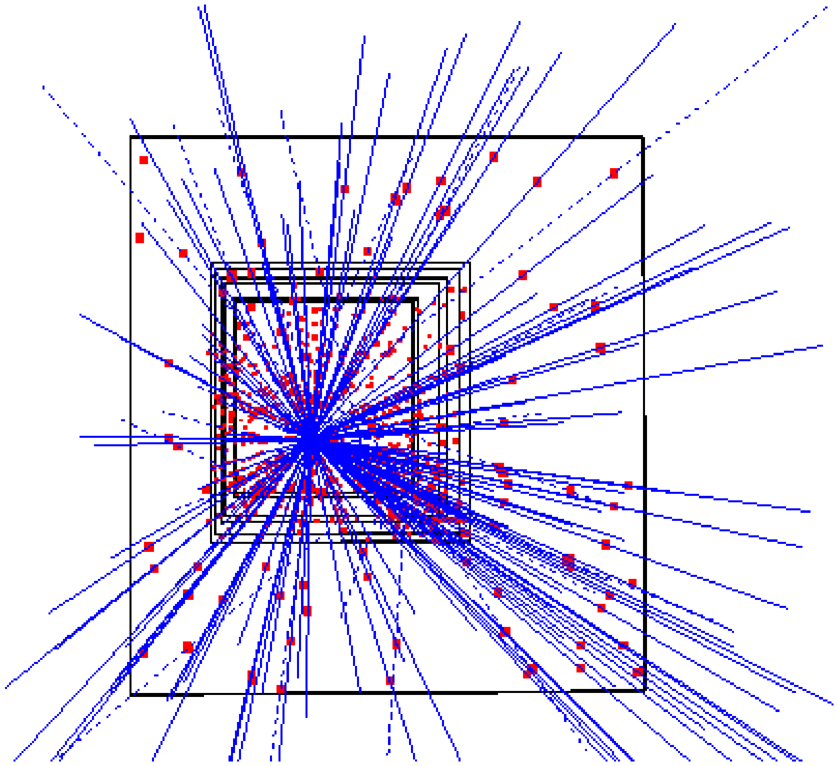

Figure 2.4: Reconstructed tracks in the WA97 pixel telescope in a no-field event.

are rectangular rather than square they will give greater resolution along one direction than the other. To compensate for this the pixel telescope contains a mixture of two orientations (one of which is simply a 90^o rotation of the other) in order to provide more accurate coverage in both the y and z directions. The WA97 set-up used some microstrips as well as pixel planes in its silicon telescope. Pixel planes have slowly been taking over, however, and the NA57 set-up consists of a telescope made entirely of pixel planes.

2.5.2 The Beam Microstrips

In the p-Be run a set of five microstrips formed a beam telescope which was used to store the parameters of the beam track for each triggered interaction. This was used for vertex finding, which will be described in more detail in the following chapter. The first of the beam microstrips was placed at $x_\Omega = -175.5$ cm, and the fifth at $x_\Omega = -131.5$ cm (with

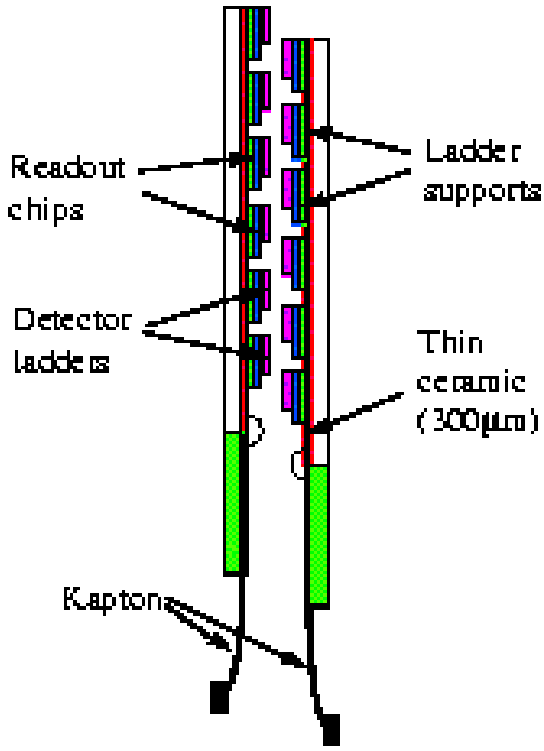

Figure 2.5: Layout of a silicon pixel plane consisting of two arrays containing six ladders each.

the others at 11 cm intervals in between). The complete layout is shown in figure 2.6.

In Pb-Pb interactions such a telescope is not needed, because the multitude of tracks produced in a Pb-Pb collision point back to a much clearer interaction point than in the lower multiplicity proton beam data. Attempting to use beam microstrips with a lead beam would also give rise to a huge background, providing yet another reason for not using a beam telescope when taking Pb-Pb data.

2.5.3 Beam Counters

As the readouts from the beam counters are the fastest of all, they are used at the lowest trigger level. There are four counters, labelled S2, V2, S4, and VØ on the layout shown

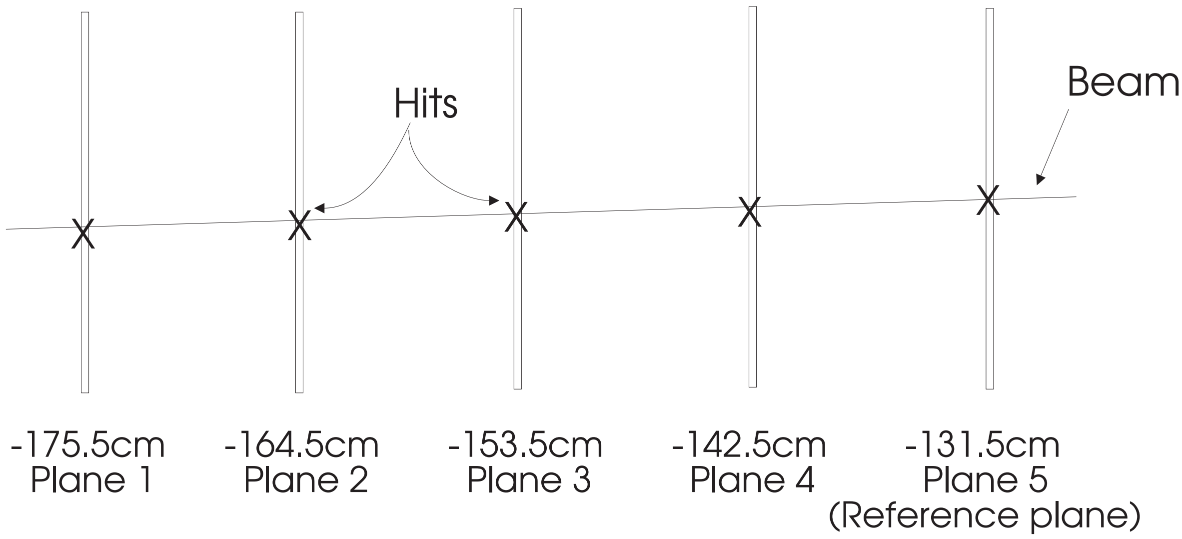

Figure 2.6: Diagram of the WA97 beam telescope.

in figure 2.2. S2 and S4 were aligned in the beam and positioned upstream of the target. V2 is a square veto counter with a circular hole in the centre to allow the beam to pass through. The veto counter was also placed upstream of the target and was used to detect particles that were not running truly along the beam axis and also to reduce background due to interactions in S2. The final counter, VØ, was placed downstream of the target. If the beam particle interacted with a target particle, it would be deflected away from the beam axis by the magnetic field and so should not pass through VØ. S2 and VØ were quartz Čerenkov counters for the lead beam and scintillators for the proton beam, while V2 and S4 were scintillators in both set-ups.

2.5.4 Multiplicity Detectors

Located close to the target, the multiplicity detectors provide a centrality trigger in Pb-Pb interactions of approximately 30 % of the cross section. The petal detector is hexagonal in shape and divided into six "petals". In a central event one would expect the multiplicity (number of hits) on each petal to be roughly equal, meaning that the petals can be used to select these events. Two planes of silicon μ-strips then sample the charged particle multiplicity and allow for more detailed off-line analysis of centrality dependences.

2.5.5 Trigger Logic

The first trigger level is called *BEAM*. There must be a signal from S2 which is in coincidence with a signal from S4. This reduces the possibility of triggering on noise in S2. From the description in the Beam Counters subsection, it is clear that there must be no signal in V2. Thus *BEAM* is defined by

$$\mathbf{BEAM} = \mathbf{S2} \cdot \mathbf{S4} \cdot \overline{\mathbf{V2}}.$$

There are two further requirements for the beam definition. *CLEAN BEAM* or *CB* requires that there must be no further signals in S2 during the resolution time of the silicon detectors ($\pm$ 30 ns). This would occur if there had been a pair of beam protons arriving at the target with too small a separation between them. Part of the signal from the S2 counter is passed to an updating discriminator. If a second signal arrives from S2 during the time Δt after the first signal arrives, then the inverse of the signal from the updating discriminator, $\overline{S2_p}$, which is lengthened by Δt, will be in anti-coincidence with S2, BEAM and $S2_{p'}$ and so the event will be vetoed. The idea that has been described here, *CB*, is also known as *past-future protection* [40]. The final requirement in the beam logic involves the beam counter VØ. If this fired, then there was no interaction between the beam and target particle, meaning that the beam particle continued along its original trajectory. Thus the full beam logic requires *CB* plus the absence of a signal in VØ, which indicates an interaction. For reference, the trigger diagram is shown in figure 2.7, although only its basic principles are mentioned here.

As mentioned in the previous section, the petal detector is used to trigger on central Pb-Pb events, based on the principle that the multiplicity of each petal should be roughly equal (and above a certain threshold) for such events. In fact the threshold was set to 10 mips (minimally ionizing particles). The trigger required that at least 5 of the 6 petals

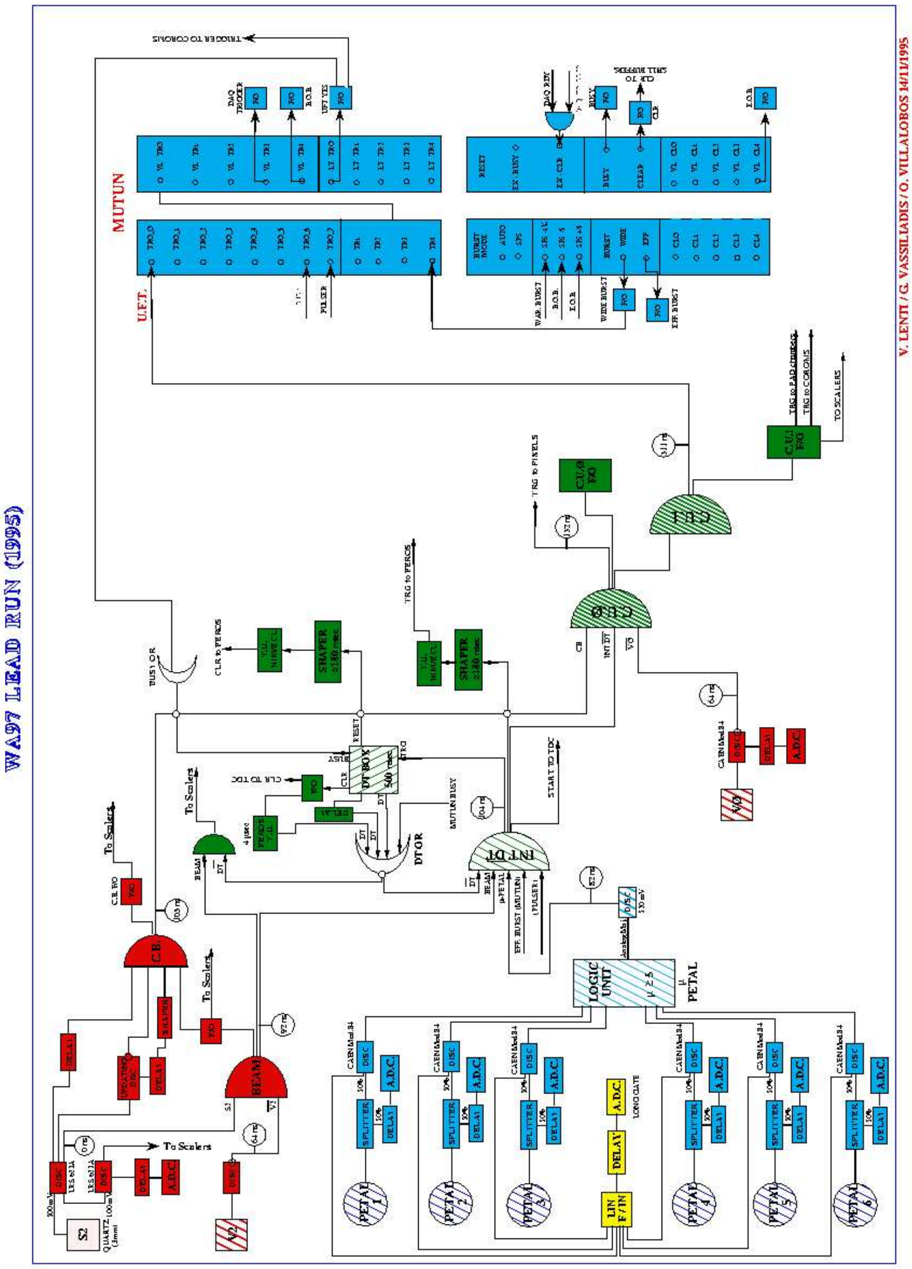

Figure 2.7: Trigger diagram for the WA97 experiment.

exceed this threshold. With this experimental set-up triggers are frequent, and so the experiment is limited by the time it took to read out all of the detectors (dead time). In the 1995 Pb-Pb run this was approximately 1400 μs per event. This results in $\sim$ 70 % of the burst being dead time for WA97.

The total number of triggers taken between 1994 and 1996 is summarised in table 2.1.

Table 2.1: No. of triggers taken between 1994 and 1996.

Year	Beam-Target	Number of triggers
1994	Pb-Pb	12×10^6
1995	Pb-Pb	120×10^6
1995	p-Pb	290×10^6
1996	Pb-Pb	330×10^6
1996	p-Be	200×10^6

2.6 Offline processing

Once hits have been recorded in the beam microstrips and silicon telescope, this information is stored onto tape in a machine independent, 16 bit EPIO [41] format in a ROMULUS block structure [42]. Knowing this structure, the relevent information on hits in different planes can later be extracted. In this raw stage the data from the silicon telescope is processed by the track identification program ORHION [43]. The program uses the independent information from each pixel plane to build up tracks. A fitting routine then produces a three-dimensional track. The data taken with the different field polarities were used to determine the alignment of the individual planes. The details of the beam track fitting were of great relevance to the vertex finding discussed in the next chapter, and so a brief description of the beam track fitting follows.

2.6.1 Beam Track Fitting

In the xz plane the points measured in the beam microstrips are fitted to a straight line. The last measured point and angle of this straight line are then recorded onto tape. In xy the situation is a little more complicated, because this plane is perpendicular to the magnetic field and so the beam track bends in the plane. What is stored on tape in this case, is once again the point at the last plane (known as the "reference plane"), together with the angle of another straight line. Obviously all of the points do not lie on this straight line (only the last), but the deviation of earlier points from the line can be parameterised by a polynomial. Although the trajectory of the particle in the magnetic field is a helix, it is convenient to approximate it by a quadratic expression $dy = ax^2$. Adding small polynomial correction terms, this gives

$$dy = ax^2(1 + \frac{x}{b} + \frac{x^2}{c} + \frac{x^3}{d})$$

where

$a = -1\times$ BFIELD $\times 1.4760 \times 10^{-6} mm^{-1}$

$b = 9267.0 mm$

$c = -9839.0 \times 10^3 mm^2$

$d = -2381.0 \times 10^7 mm^3$

In the first expression, dy and x are both in millimetres, and x is the distance from the reference plane. The parameter BFIELD is set to $+1$ for field up, and -1 for field down. There are therefore five key parameters from the beam microstrips which are later used for the vertex finding, these being

XREF - The x coordinate of the reference plane (which is always -131.5cm)

YREF - The y coordinate of the last measured point at XREF

ZREF - The z coordinate of the last measured point at XREF

PHIBM - The angle of the *straightened* beam track in the xy plane

DIPBM - The angle of the straight line beam track in the xz plane

These parameters are then used to define equations of the beam in order to find the vertex. Figure 2.8 shows the way in which the straightened beam track is found in the xy plane and the way in which the respective shifts dy relate the true beam track and the straightened beam track at each measured point.

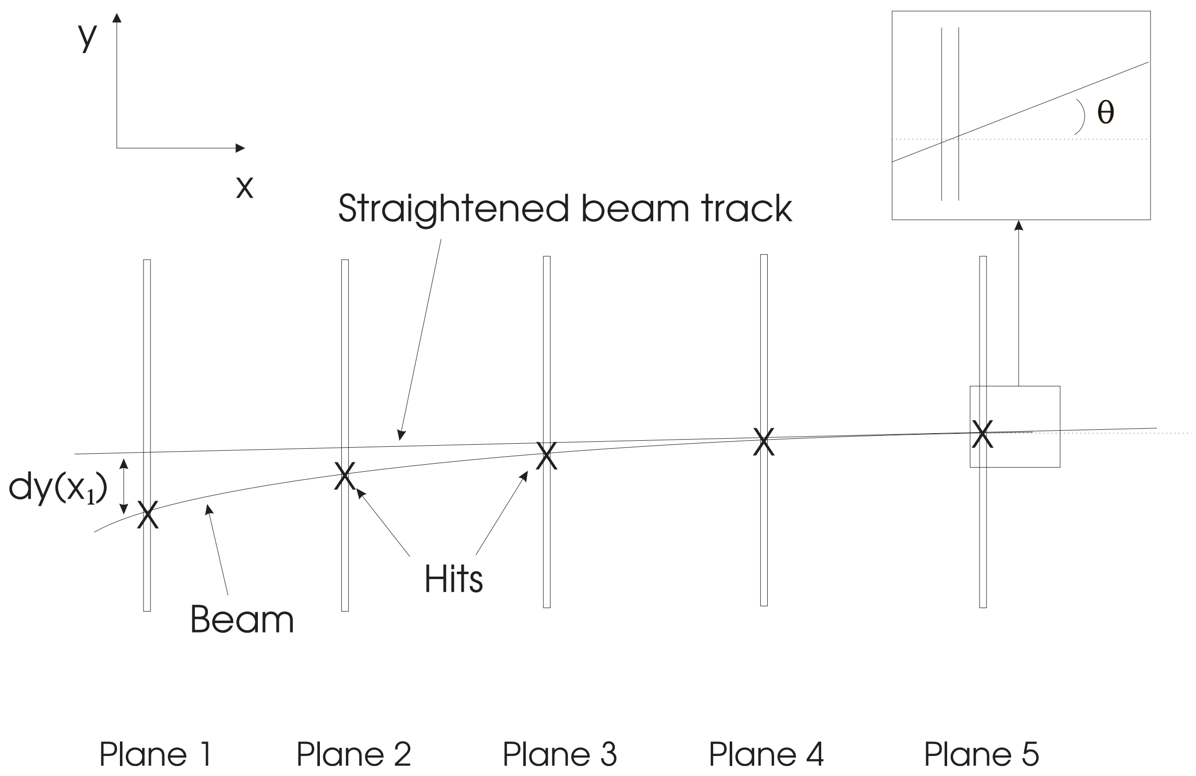

Figure 2.8: Relation between the straightened and actual beam track, and the meaning of the angle PHIBM = θ.

2.7 The NA57 Set-up

While data from NA57 have, at the time of writing, gone through only the most preliminary stages of processing, a few words should be said on the layout of current and future heavy-ion experiments. Apart from having a telescope composed totally of pixel planes, the NA57 experiment uses a number of the upgraded OMEGA-3 planes in its telescope (which have a finer pixel size than the previous OMEGA-2 planes). The ALICE experiment intends to take the use of pixels even further, with a fully cyclindrical tracking barrel surrounding the interaction point. It has also been proposed that because of the relative ease with which pixel detectors can handle high multiplicity environments, the NA57 experiment could attempt to indentify charm decays (in much the same way that they have looked at strangeness) by moving the pixel telescope closer to the target in the hope of picking up a signal of these somewhat shorter lived decays.

Chapter 3

Reconstruction of Hyperon Decays

3.1 Introduction

As previously mentioned, the WA97 experiment searches for the hyperon decays

$$\Lambda(uds) \rightarrow p\pi^-,$$

$$\Xi^-(dss) \rightarrow \Lambda\pi^-,$$

$$\Omega^-(sss) \rightarrow \Lambda K^-.$$

Therefore, the signature for a Λ decay is two oppositely charged tracks which intersect some distance from the target, and the signature for a Ξ^- or Ω^- decay is a negatively charged track which intercepts with a Λ and has a resultant cascade candidate that traces back to the target [44]. A schemematic diagram of such a decay is shown in figure 3.1. The name "V^0" is given to neutral tracks which decay into two charged particles, which, therefore, includes Λs (and the charge conjugate $\overline{\Lambda}$s), and also K^0s.

When a neutral particle decays into two charged tracks in a magnetic field, two basic topologies are possible. One is where the two tracks come off in the directions in which

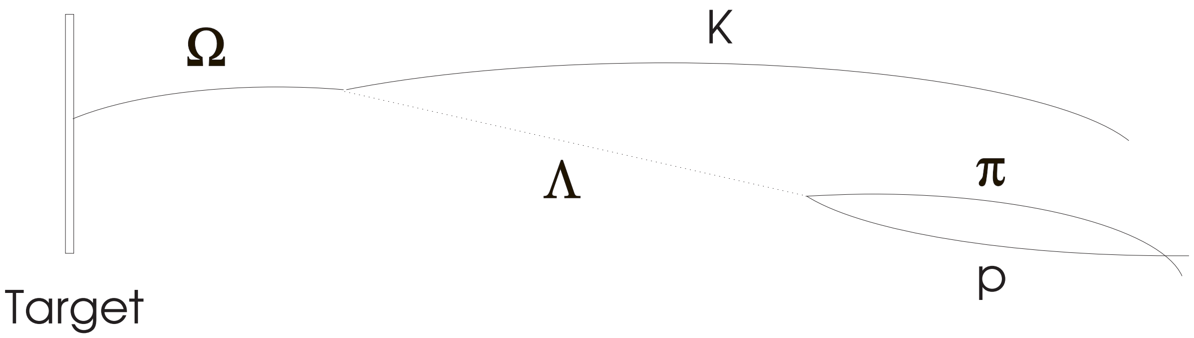

Figure 3.1: Schematic diagram of an Ω decay in a magnetic field.

they will bend in the magnetic field, and is called the *Sailor* topology. The other is when the two tracks go off in the opposite direction to which they will bend in the magnetic field, and so will cross again, in the bend plane, at some point later in time. This is known as the *Cowboy* topology. The acceptance in the WA97 experiment favours the Cowboy topology, since in this configuration the tracks will have separated by a smaller distance by the time they reach the silicon telescope. The Cowboy and Sailor topologies are shown in figure 3.2.

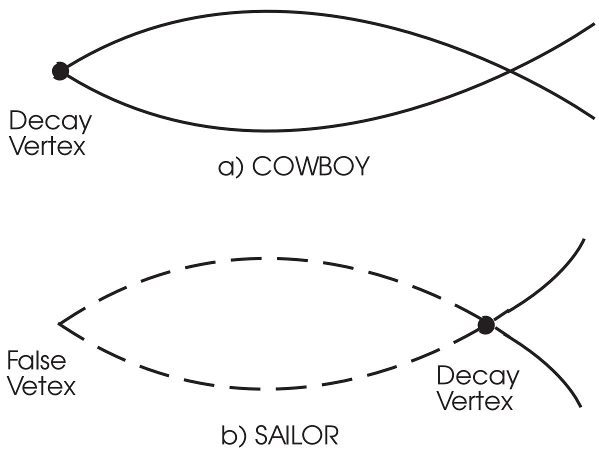

Figure 3.2: The Cowboy and Sailor topologies.

3.2 Reconstruction of V^0 Candidates

The track identification program ORHION reconstructs tracks from the hits recorded in the silicon telescope. V^0s are then found by a program called STRIPV0, which makes use of a NAGLIB [45] minimising routine in order to find the point of closest approach between oppositely charged tracks. An initial loose cut can then be imposed on the distance of closest approach, and candidates written to a data summary tape (DST). A schematic diagram, showing a reconstucted V^0 decay and the parameters d (the distance of closest approach) and B_y (the impact parameter of a track in the y direction with respect to the interaction vertex) are shown in figure 3.3.

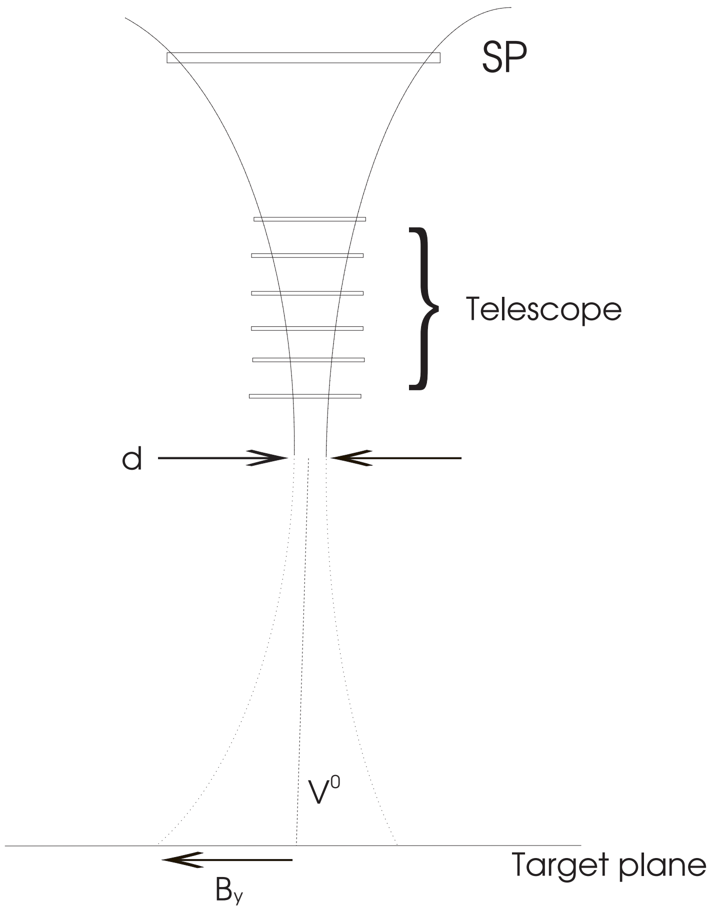

Figure 3.3: Reconstruction of a V^0 decay.

The distance of closest approach is defined as the distance that separates the closest points on the two oppositely charged tracks. The V^0 decay vertex is then defined as half way along the line that joins these two points.

V^0 candidates are selected by use of the Armenteros-Podolanski variables α and q_t [46]. α is defined such that

$$\alpha = \frac{q_L^+ - q_L^-}{q_L^+ + q_L^-}$$

where q_L^+ and q_L^- are the longitudinal momenta components of the +ve and -ve decay tracks respectively, with respect to the line of flight of the V^0. Therefore, if the longitudinal momentum of the -ve track is greater than that for the +ve track, α will be negative. Similarly, if q_L^+ is greater than q_L^- then α will be positive. This separates Λ from $\overline{\Lambda}$, since Λ decays into proton and π^-, which means that when boosted into the lab the proton should have the higher momentum, and so q_L^+ is greater than q_L^-, and therefore α is positive. Conversely in $\overline{\Lambda}$ decay, the anti-proton should have higher momentum than the π^+, and so α would be negative. K^0s decay via $K^0 \rightarrow \pi^+ + \pi^-$, and since the oppositely charged pions should have similar q_L in the Lab frame, α for K^0s should have a distribution centred about $\alpha = 0$. One can therefore plot q_t against α and see the V^0 candidates separate out into three distinct bands of Λ, $\overline{\Lambda}$ and K^0 respectively. There will also be an extra (horizontal) band for γs unless a cut is made at low q_t. Figure 3.4 shows the three bands (or loci) in such a plot. A derivation of the equations which describe these loci is presented in Appendix A. Note that, once background has been removed with an appropriate q_t cut, K^0 candidates can be selected unambiguously from Λs and $\overline{\Lambda}$s in the region $|\alpha| < 0.45$.

3.3 Reconstruction of Cascade Candidates

Once V^0s have been found by the V^0 finding routine STRIPV0, it is possible to search for the cascade signature of a V^0 intersecting with a charged track. Just as there is a

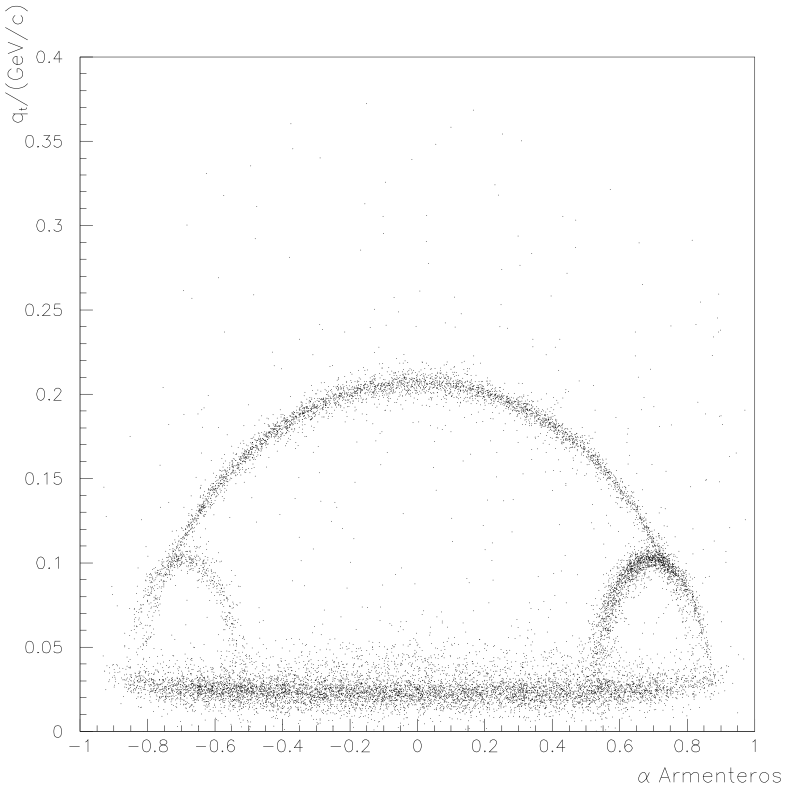

Figure 3.4: Armenteros-Podolanski plot showing K^0, Λ and $\overline{\Lambda}$ bands.

distance of closest approach for the two decay tracks from a V^0 decay, so there is a similar distance of closest approach between the charged track and V^0 in a cascade decay. As in the V^0 case, loose cuts can be applied on this closest approach parameter and it is similarly defined as the distance between the two closest points on the V^0 and charged track. A schematic diagram of a cascade decay is shown in figure 3.5.

3.4 p-Be Beam Reconstruction and Vertex Finding

Once V^0s and cascades have been reconstructed through the closest approach of the appropriate tracks found in the telescope, it is then necessary to find where in the target the particle was produced (ie. the primary vertex). In Pb-Pb events there are many charged tracks pointing back to a single interaction point, and so the interaction vertex

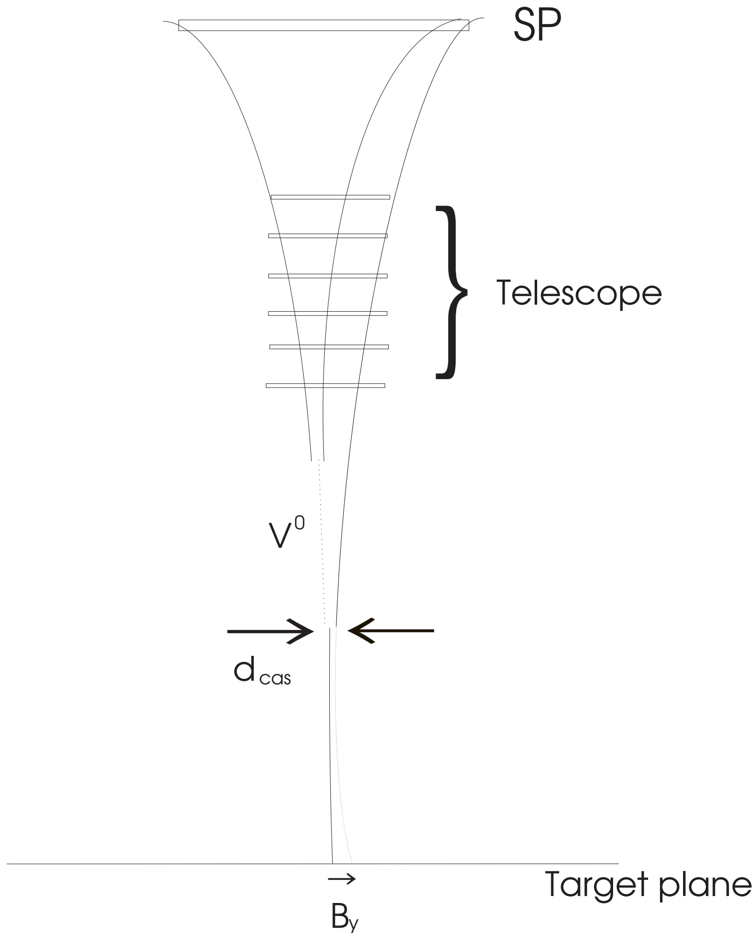

Figure 3.5: Reconstruction of a cascade decay.

is relatively easy to find by minimising the distance between the extrapolated tracks. In p-Be, however, there may only be two or three tracks and so the position of the interaction vertex is not always obvious. In order to do this on an event-by-event basis it is necessary to reconstruct the beam as it passes through the series of beam microstrips on its way to the target. This means finding an equation which describes the beam within the target region, and then finding out where it intersects with the Λ, Ξ or Ω.

The equation of the beam is deduced by first recording its x, y and z coordinates at the reference plane, along with the two angles DIPBM and PHIBM. The problem is then separated into two orthogonal planes; xy and xz. The magnetic field is in the z direction

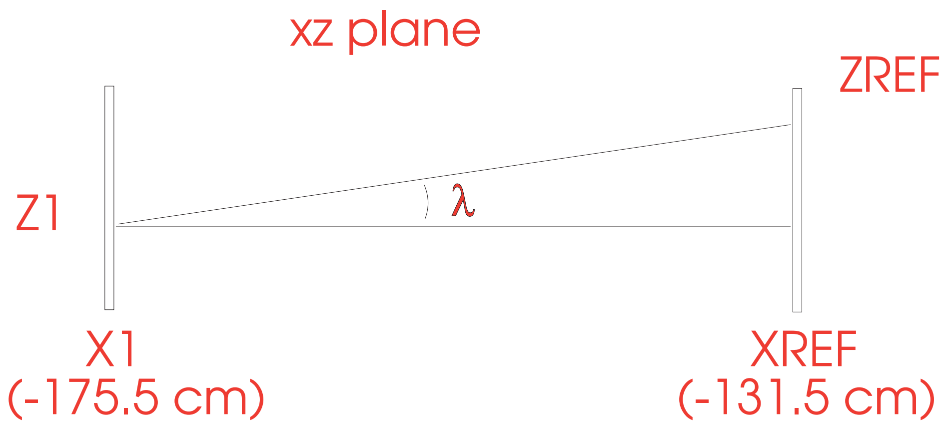

Figure 3.6: Diagram of the reference planes used for beam tracking.

and so causes charged particles to bend in the xy plane. Therefore, the beam will follow a circle in the xy plane, for a homogeneous field, and a straight line in the xz plane where bending of the track should be negligible. Figure 3.6 shows the path taken by the beam in the xz plane. The equations the beam follows in the xy and xz planes are of the form

$$(x - x_0)^2 + (y - y_0)^2 = R^2$$

$$z = mx + c$$

respectively, where x_0 and y_0 are the coordinates at the centre of the circle, R is its radius, and m and c are the standard gradient and intercept in a straight line fit. Of these, the radius R is known because it is related to the momentum of the track ($\sim$ 158 GeV/c) and the strength of the magnetic field (which is a known quantity). In the xy plane this leaves x_0 and y_0 unknown, but since the radius is fixed, both x_0 and y_0 can be determined once a second point on the circle is known. This can be accomplished by finding the y coordinate of the straightened beam track at the same x coordinate as one of the beam microstrip planes and then deducing the position of the actual hit by calculating the size of the dy shift from the straightened track at that x position. This gives two points on the circle, which are almost enough to uniquely define it - the only other piece of information required is the polarity of the field (which basically just defines whether the circle is bending one way or the other). In the xz plane the situation is a little less complicated, since the gradient m of the line is just the angle DIPBM expressed in radians. The next stage of calculating the interaction point is forming an equation for the Λ, Ξ, or Ω particles that come from the target. In p-Be interactions, the vast majority of hyperons produced are going to be Λs. The Λ information which is stored on tape are the momentum components, p_x, p_y and p_z at the decay point with coordinates x, y, z. Λs (or indeed $\overline{\Lambda}$s) are neutrally charged and so follow a straight line in both planes of the magnetic field. Once the equations of the beam and Λ are known, calculating the x and z coordinates of the interaction point is then done by finding the intercept of the beam and Λ in the xz plane. This is defined by

$$x_{int} = \frac{c_2 - c_1}{m_1 - m_2}$$

where m_1, m_2, c_1 and c_2 are the gradient and intercepts which describe the x and z coordinates of the beam and Λ respectively, through the equations $z_1 = m_1 x_1 + c_1$ for the beam, and $z_2 = m_2 x_2 + c_2$ for the Λ. Since both beam and Λ follow these straight lines in this plane, there is therefore a single, well-defined interaction point where the two lines cross. In the xy plane one therefore only needs to work out the y coordinate of the beam at this value of x. This is given by the formula

$$y_{int} = y_0 \pm \sqrt{R^2 - (x_{int} - x_0)^2}$$

where the plus or minus term arises from the fact that there are two possible centres for a circle defined by two points. The correct solution is found by knowing in which direction the beam is curving, which is determined of course by whether the field is up or down. In this approach the cascades can be treated in exactly the same way as the V^0s - by finding the intersection of two straight line equations in the xz plane and then deducing the circular beam's position in y at that particular value of x. Further details on the calculation of the primary vertex can be found in Appendix B.

3.4.1 Beam Telescope Alignment

When calculating the intersection of a hyperon with the beam, one is considering first information from the beam microstrips, and second information from the silicon telescope. In principle, some misalignment could exist here, such that a coordinate x, y, z as measured by one telescope is not quite equal to exactly the same x, y and z coordinates with respect to the other. Such effects should of course be small, but the possibility of such deviations needs to be considered when finding the vertex. This is particularly true of the x coordinate of the vertex, since the beam and hyperon lines tend to be fairly parallel (particularly in the xy plane) and so small deviations in y and z of the order of less than a millimetre can lead to significant deviations in x of the order of centimetres.

In order to check whether any alignment was needed, a simple test was performed on the raw STRIPV0 output. STRIPV0 attempts to make V^0s from pairs of oppositely charged tracks. However, not all such tracks will be true V^0s and, indeed, close to the target region most candidates will simply be oppositely charged tracks which come from an interaction at the primary vertex. Therefore, if no alignment shift was needed, then what one would expect would be that if one traced the beam in such interactions to the x coordinate of the "V^0 decay point", then the differences dy and dz between the beam and the y and z coordinates of the V^0 decay vertex should have a distribution centred about zero. When this was checked on the data it was found that small shifts were present in both the y and z directions. Figure 3.7 shows the distribution of dz, the difference in z between the beam and V^0 at the x coordinate of the V^0 decay vertex. The events are separated into different plots for field up and field down to ensure that no field effects are present. Both plots show a common shift in the positive z direction of about half a millimetre. The shift in y was of a similar size and so the final shifts applied to the recorded beam position for vertex finding were a 0.82 mm shift in y, and a 0.54 mm shift in z. A number of tests were performed to ascertain the size of the effect this would have on the x coordinate of the primary vertex. The answer was indeed found to be that it shifted the x coordinate by the order of a centimetre.

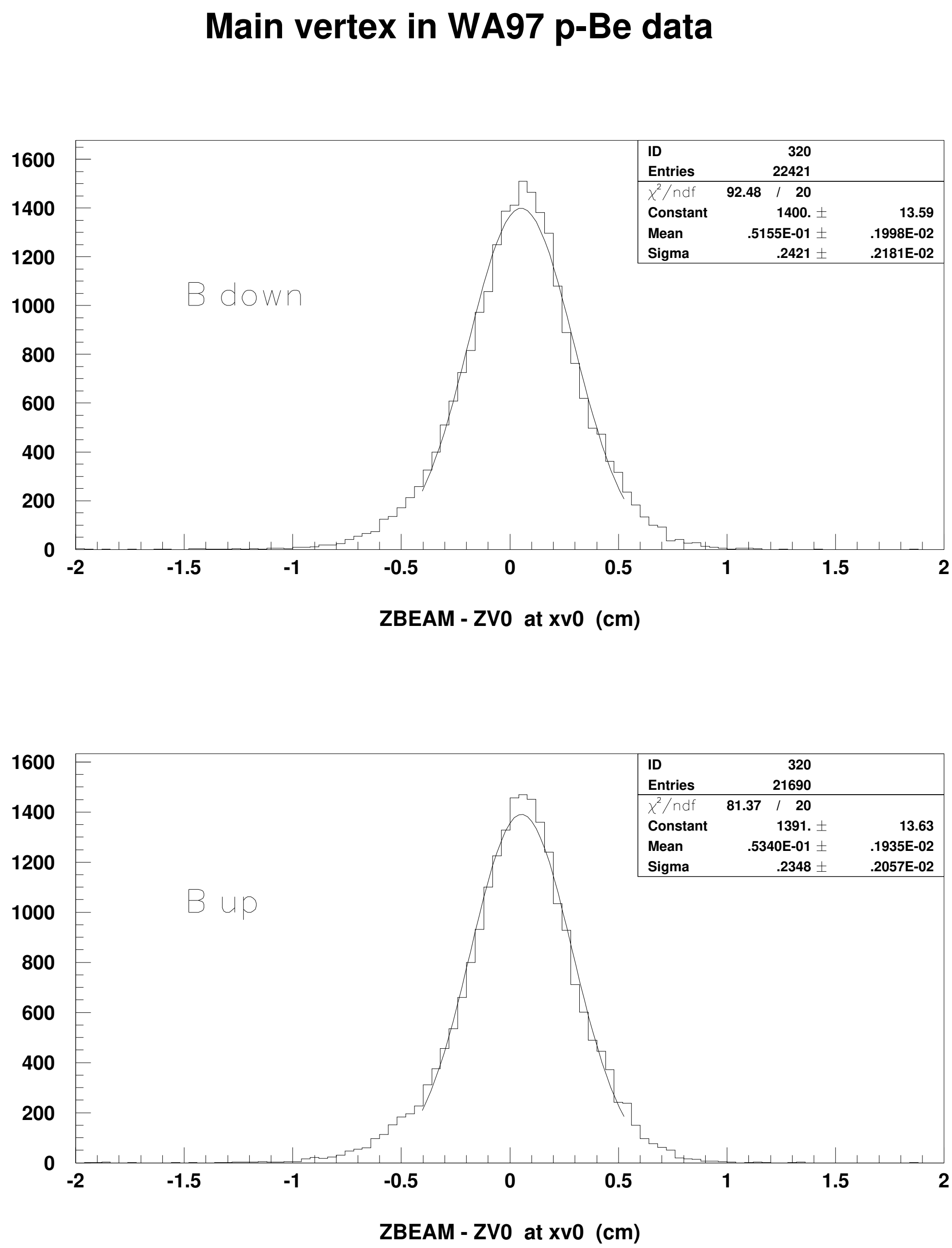

Figure 3.7: The difference between the z coordinate of the beam and the z coordinate of the V^0 at the x coordinate of the V^0 decay vertex, for field down (top), and field up (bottom).

Once the primary vertex has been calculated, it can then be used in selection cuts and also plays a vital role in the event weighting procedure (since a particle that originates from one interaction point will tend to have a different geometrical acceptance than one that originates from another).

3.5 Preliminary Cuts

Once the raw data have undergone the first stage of processing (ie. track finding), the V^0 and cascade finding programs ANALYZE and CASCADE are used to perform a series of loose cuts on the sample. The idea of this is to provide an "ntuple" in which more stringent cuts can be performed in order to select out the final sample of good or "gold-plated" candidates.

Preliminary selection of Λ and $\overline{\Lambda}$ candidates is made from the raw p-Be data by applying the following cuts

- The decay must have cowboy topology.
- $|\alpha| \geq 0.45$
- $q_t \leq 0.40$ GeV/c
- At the V^0 decay vertex the distance of closest approach of the V^0 decay tracks must be less than 0.1 cm.

This leads to a number of interesting mass distributions. Figure 3.8 shows the $p\pi^-$ effective mass distribution for a fraction of the sample. Besides the Λ peak that is visible at close to the Particle Data Group (PDG) value of 1.116 GeV [47], there are also two other clear peaks on top of the background. These correspond to the K^0s and $\overline{\Lambda}$s, because for the K^0 the positive track is actually a pion, not a proton, and for the $\overline{\Lambda}$ the signs of the tracks are reversed, such that the negative track is an anti-proton and not a pion, and (as with the K^0) the positive track is a pion and not a proton.

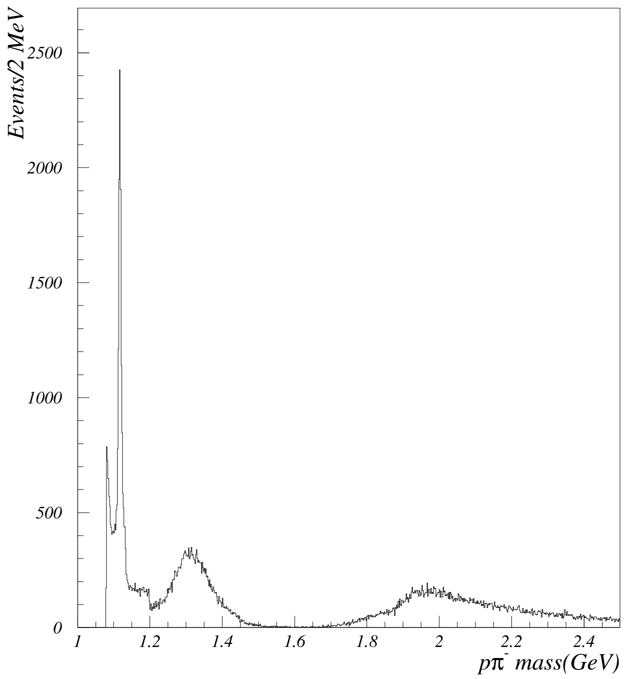

Figure 3.8: $p\pi^-$ effective mass distribution after preliminary cuts.

Similar plots can be made for the $\overline{\Lambda}$s and K^0s. Figure 3.9 shows the $\overline{p}\pi^+$ effective mass distribution for the same sample of the data. Again, the two apparently spurious peaks are K^{0}s and Λs, which do not have genuine $\overline{p}$ and π^+ tracks. Figure 3.10 shows the $\pi^+\pi^-$ effective mass distribution, with the K^0 peak visible at around the PDG value of the K^0 mass (498 MeV). This time, the fact that $\pi^+\pi^-$ is a symmetric combination leads to the Λs and $\overline{\Lambda}$s combining into a single extra peak at around 0.8 GeV.

The primary vertex distribution in x can be seen in figure 3.11. This shows a clear signal in the target region, even with these somewhat preliminary cuts.

Preliminary selection of cascade (Ξ and Ω) candidates in p-Be data is made by use of the following cuts

- The cascade decay must have cowboy topology.
- The V^0 decay must have cowboy topology.

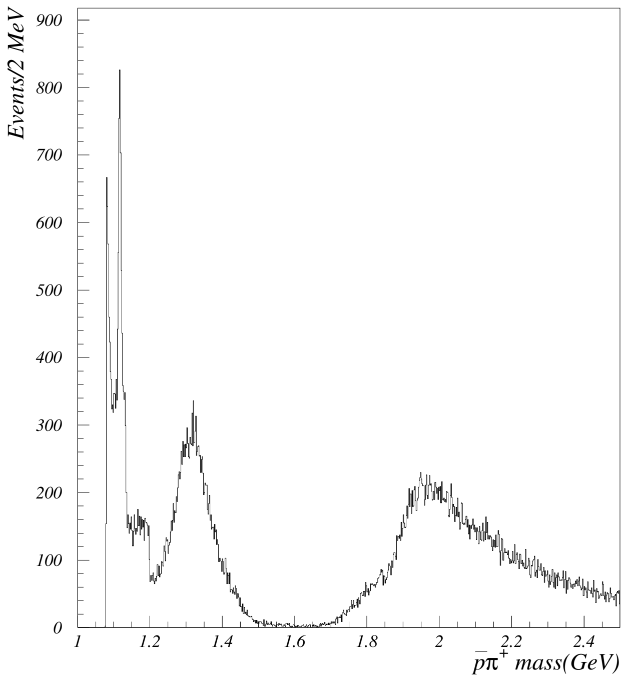

Figure 3.9: $\overline{p}\pi^+$ effective mass distribution after preliminary cuts.

- At the cascade decay vertex, the distance of closest approach between the line of flight of the V^0 and the charged decay track is less than 0.1 cm.

- The distance of closest approach of the V^0 decay tracks must be less than 0.1 cm at the V^0 vertex.

- For the V^0, $0.02 \leq q_t \leq 0.40$ GeV/c.

This gives a $\Lambda\pi$ effective mass distribution of remaining candidates as can be seen in figure 3.12. This mass plot already gives an indication that the number of combined Ξs and $\overline{\Xi}$s should total roughly five or six hundred after background subtraction. It will later be shown that this approximate number corresponds very closely to the total number remaining after final cuts.

The vertex distributions of these candidates in the x, y, and z directions can be seen in figures 3.13, 3.14 and 3.15 respectively. The next chapter will describe in more detail

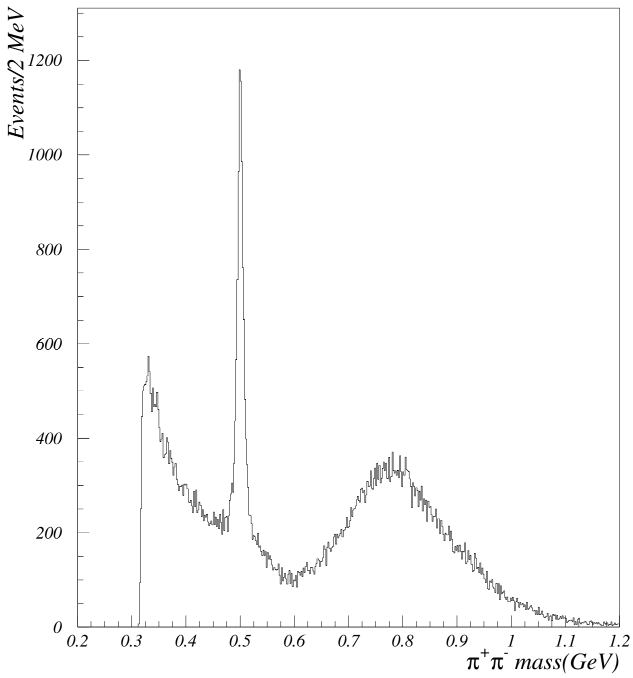

Figure 3.10: $\pi^+\pi^-$ effective mass distribution after preliminary cuts.

the final cuts required to select the"gold-plated" candidates.

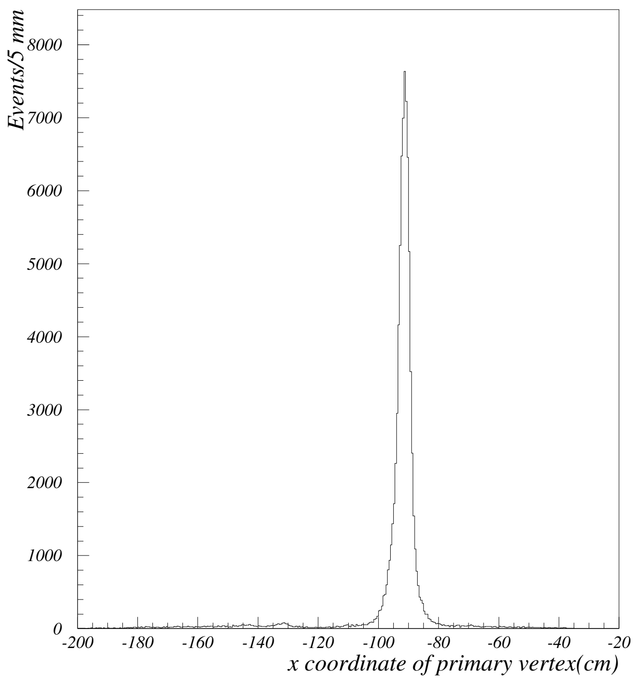

Figure 3.11: x coordinate of interaction vertex for V^0 candidates after preliminary cuts.

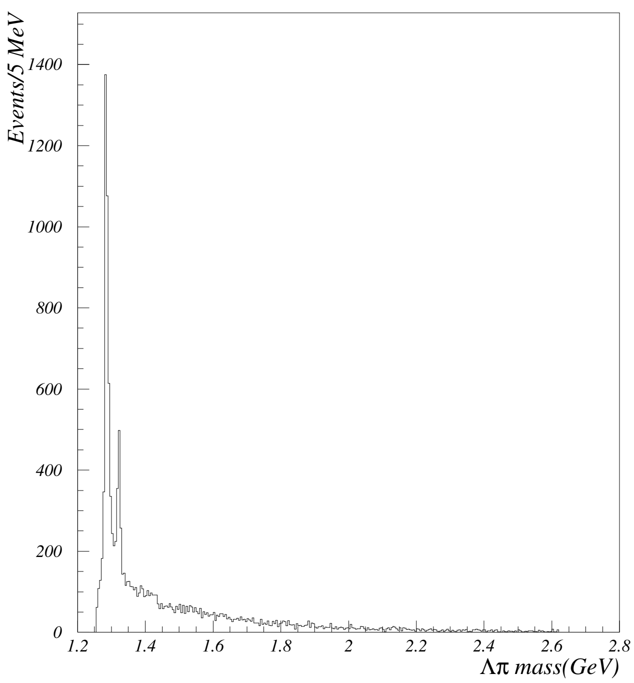

Figure 3.12: $\Lambda\pi$ effective mass distribution after preliminary cuts.

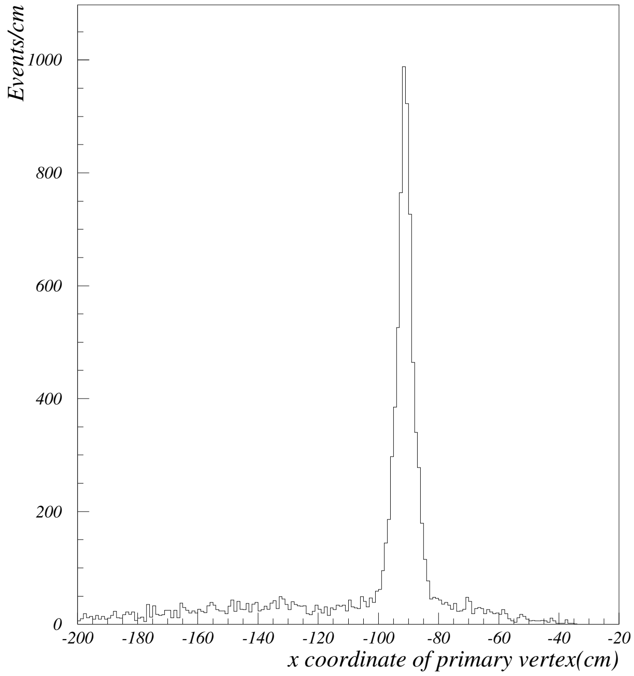

Figure 3.13: x coordinate of interaction vertex for cascade candidates after preliminary cuts.

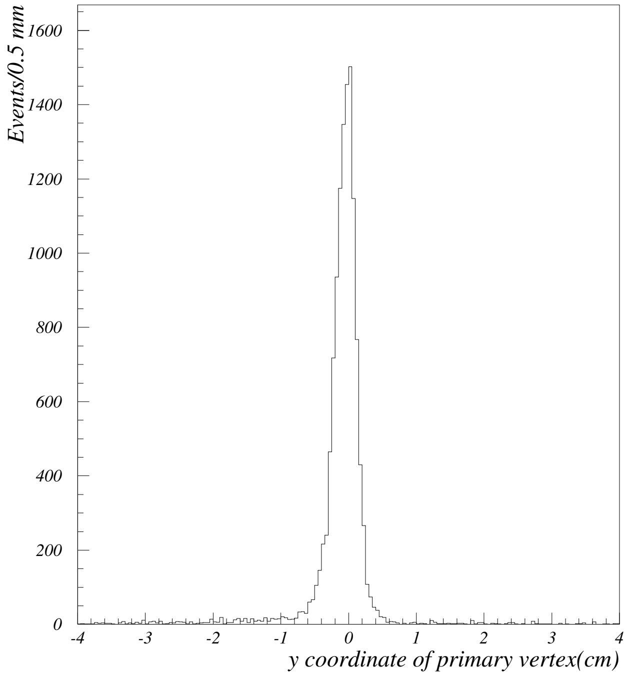

Figure 3.14: y coordinate of interaction vertex for cascade candidates after preliminary cuts.

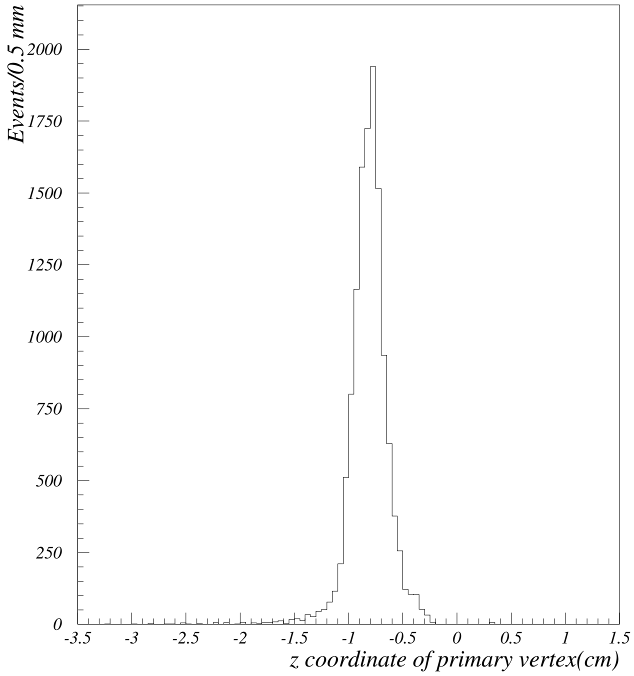

Figure 3.15: z coordinate of interaction vertex for cascade candidates after preliminary cuts.

Chapter 4

Selection of Gold-Plated Hyperon Decays

Once preliminary cuts have been performed on the V^0 and cascade candidates, it is then necessary to draw up a list of the final cuts which will be used to select the so called "gold-plated" events that form the final sample. These cuts will now be discussed for the three hyperon species, Λ, Ξ, and Ω.

4.1 The Trigger Condition

One series of cuts applied to both V^0s and cascades is the so called "Trigger Condition". This places constraints on which planes of the silicon telescope that each of the decay tracks must pass through. In this way it also ensures that any tracks taken are "good" tracks, in the sense that they have a certain minimum number of hits recorded in the detectors. The Trigger Condition cuts placed on the V^0 candidates are as follows

- Both V^0 decay tracks must pass through the first and fourth pixel planes.
- One V^0 decay track must pass through the SP and ST2 scintillators.

For cascades the situation is slightly different because there are three tracks, but essentially the same type of cuts are applied. These being

- All three cascade decay tracks must pass through the first and fourth pixel planes.
- At least one cascade decay track must pass through the SP and ST2 scintillators.

4.2 Λ Selection Cuts

Once preliminary cuts have been performed, the more stringent cuts can then be made. Although the maximum possible q_t had been set to 0.40 GeV/c in the previous chapter, the lower limit was raised to reduce background from γ conversions. The cut applied was

- $0.04 \leq q_t \leq 0.40$ GeV/c

A cut was also placed about the V^0 decay vertex in order to ensure that the candidate was not a fake V^0 formed from two oppositely charged tracks coming from the target. The cut made was

- The V^0 decay vertex lies in the region described by $-50 < x_\Omega < 0$ cm.

Figure 4.1 shows the x coordinate of the V^0 decay vertex for a sample of the remaining candidates after such a cut. As can be seen, relatively few candidates are removed in this way - since the distribution peaks near the telescope at $x_\Omega = 0$ cm.

Next came two cuts to ensure that the V^0 itself does come from the target. This is done in two ways: firstly by checking the impact parameter in y of the V^0 when it is traced back to the target plane and secondly through a cut on the vertex distributions (of the type shown at the end of the previous chapter) for the remaining candidates. Similar cuts will be described in a little more detail for cascades later in the chapter. The two cuts made in order to ensure that the V^0 comes from the target are

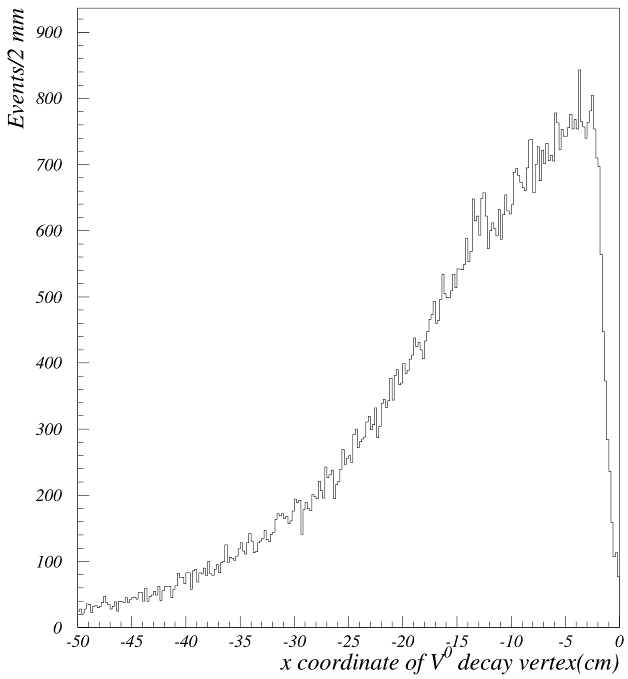

Figure 4.1: x coordinate of the V^0 decay vertex.

- The V^0 must come from the target, with the impact parameter $|B_y| \leq 0.3$ cm.
- The reconstructed primary vertex must lie within 0.3 cm in y and z and 5 cm in x from the mean position for that run.

A problem was also found with low q_t events that had a sailor vertex near to the silicon telescope. Figure 4.2 shows a plot of the x coordinate of the Sailor vertex for those candidates that survive the loose cuts described in the previous chapter. A peak is clearly visible near $x_\Omega = 0$ cm (ie. where the silicon telescope begins).

The interesting thing now comes when one plots exactly the same events, separated into two categories - one with q_t greater than 0.065 GeV/c and the other for q_t less than 0.065 GeV/c. The Sailor vertex for the events with q_t greater than 0.065 GeV/c is shown in figure 4.3. The erroneous peak appears to be completely removed by this cut. The Sailor vertex for the other candidates (ie. those with q_t less than 0.065 GeV/c) is shown in figure 4.4. The events that form the extra peak in figure 4.2 appear to come almost

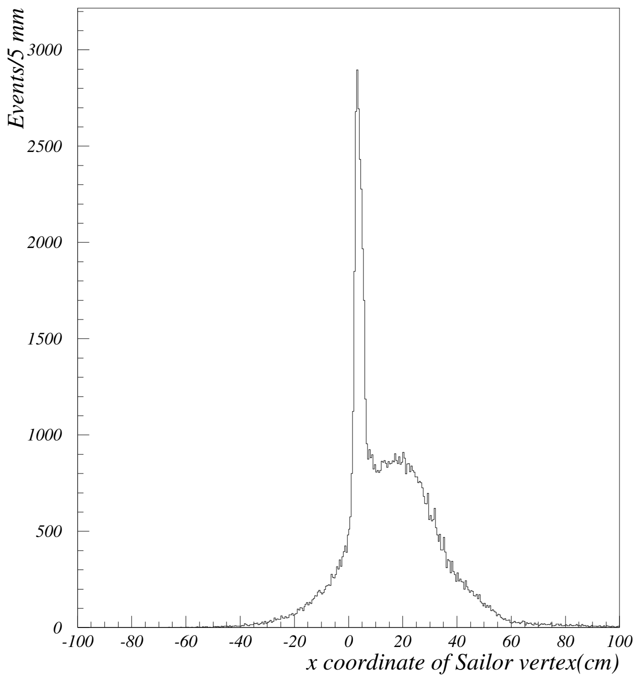

Figure 4.2: x coordinate of the V^0s' Sailor vertex.

exclusively from this sample. Since these events appear to have a Sailor vertex close to the telescope and also have a low value of q_t, it is suspected that they may be the result of γ conversions in the planes of the telescope, creating an e^+e^- pair that appear to be the charged tracks of a V^0 decay. The following cut is then made

- The sailor vertex of the V^0 must lie outside the region given by $3 < x_\Omega < 7$ cm for $q_t < 0.065$ GeV/c.

The V^0 sample now only needs final mass cuts to select out the final gold-plated events. With a mass cut placed about the K^0 mass (such that a candidate is required to have a reconstructed mass as a K^0 which lies more than 23 MeV from the PDG value), the $p\pi^-$ and $\overline{p}\pi^+$ effective mass distributions shown in figures 4.5 and 4.6 respectively were obtained. Of course there are more Λs than $\overline{\Lambda}$s, and hence the apparent asymmetry in the two plots.

The cut on the K^0 mass was tightened slighty, so that it now reads

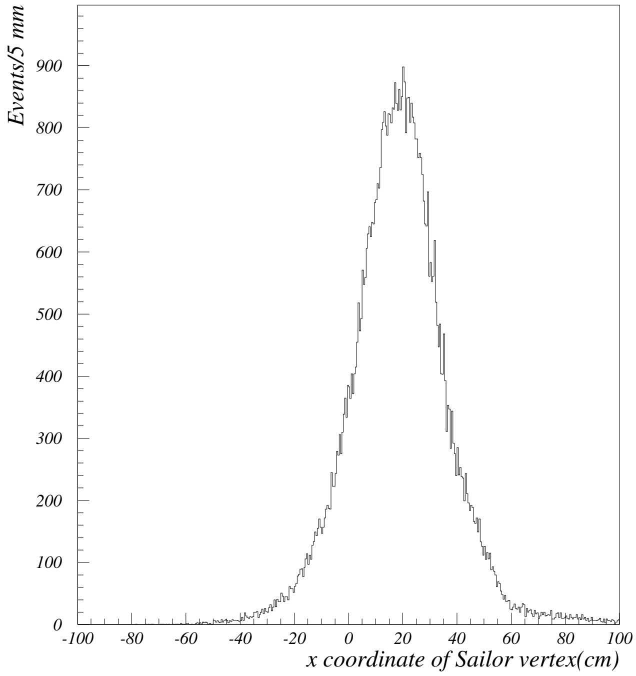

Figure 4.3: x coordinate of the V^0s' Sailor vertex for those events with q_t greater than 0.065 GeV/c.

- The reconstructed mass as a K^0 must differ from the PDG value by more than 30 MeV.

The q_t versus $\alpha_{Armenteros}$ plot for the remaining candidates is shown in figure 4.7. Separating the remaining candidates into those with $\alpha_{Armenteros}$ greater than zero, and those with α Armenteros less than zero, the effective mass of $p\pi^-$ was plotted on the left of figure 4.8 for those candidates with $\alpha > 0$, and the effective mass of $\overline{p}\pi^+$ was plotted on the right of figure 4.8 for those candidates with $\alpha < 0$.

This led to the following final mass cuts

- If α Armenteros is greater than 0.45, then the reconstructed Λ mass must lie within 15 MeV of the PDG value.

- If α Armenteros is less than -0.45, then the reconstructed $\overline{\Lambda}$ mass must lie within 15 MeV of the PDG value.

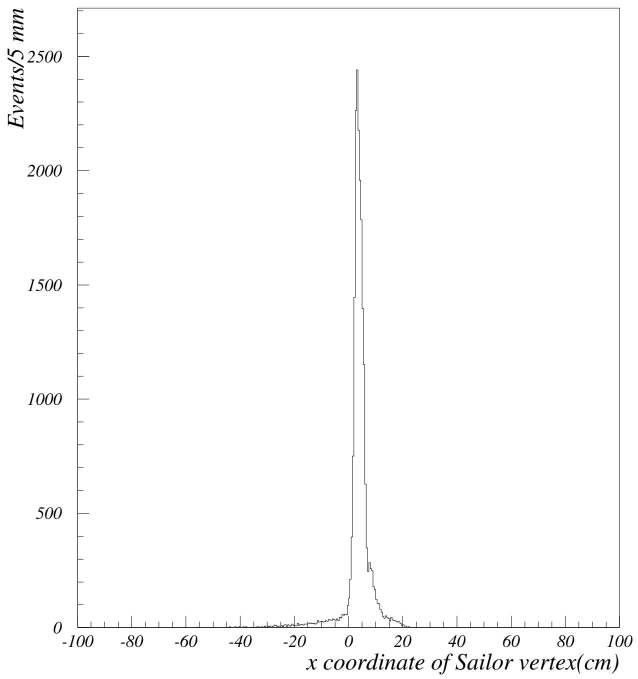

Figure 4.4: x coordinate of the V^0s' Sailor vertex for those events with q_t less than 0.065 GeV/c.

After these final cuts, the remaining candidates with positive α Armenteros are considered to be gold-plated Λs, and those with negative α Armenteros are considered to be gold-plated $\overline{\Lambda}$s. There were a total of 119,320 gold-plated Λs and 34,349 gold-plated $\overline{\Lambda}$s found in the p-Be data.

4.3 Cascade Selection

4.3.1 Ξ Selection Cuts

Once all of the information is available on the loosely cut cascade candidates shown in the previous chapter, it is then possible to proceed to the more detailed selection cuts, as will be described now. One reconstruction problem commonly found by the experiment and its software is the reconstruction of fake candidates with a cascade decay vertex close to

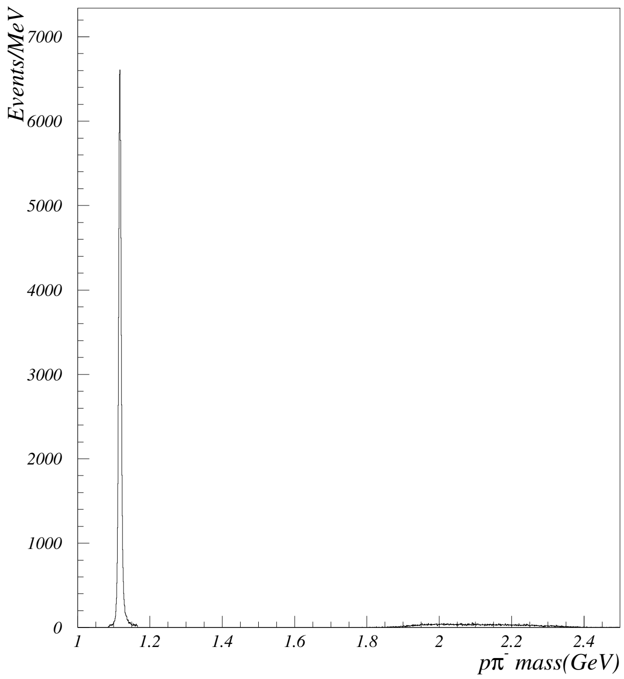

Figure 4.5: $p\pi^-$ effective mass spectrum before mass cuts, with a 23 MeV mass cut about the PDG K^0 mass.

the silicon telescope. Figure 4.9 shows the distribution of $\Lambda\pi$ effective mass as a function of the x coordinate of the cascade decay vertex. This clustering close to the telescope can be clearly seen for the fake candidates, whereas for candidates with a good value of the Ξ mass the distribution is very evenly spread with respect to the cascade decay vertex. This leads to the following cascade selection cut

- The cascade decay vertex lies in the region described by $-80 < x_\Omega < -2.5$ cm.

Since the V^0 is produced from the cascade decay, causality also requires that the V^0 decay vertex must occur after the cascade decay vertex. This places the following two requirements on the V^0 decay vertex

- The V^0 decay vertex lies downstream of the cascade decay vertex (ie. $x_{V^0} - x_{cas}$ > 0).

- The V^0 decay vertex lies in the region described by $-80 < x_\Omega < 0$ cm.

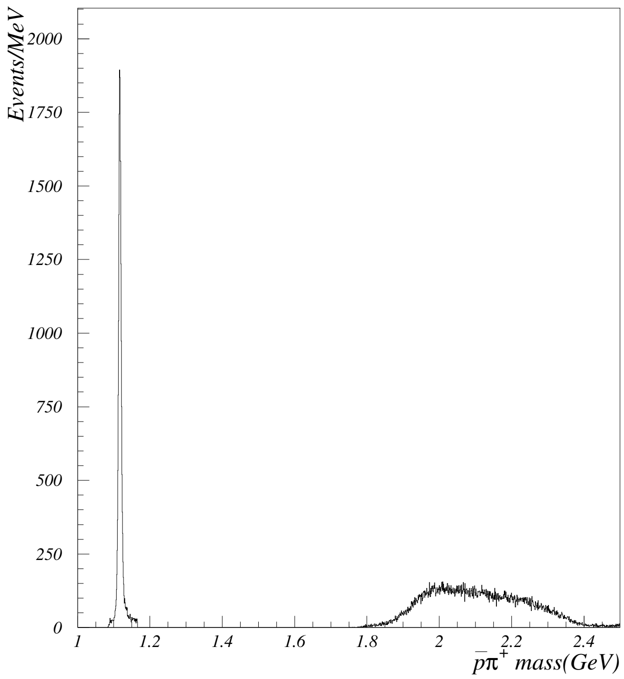

Figure 4.6: $\overline{p}\pi^+$ effective mass spectrum before mass cuts, with a 23 MeV mass cut about the PDG K^0 mass.

Now we come onto the somewhat more elegant cuts which consider the topology of the decay and how this places constraints on certain parameters for the genuine cascades. The first two of these consider the cascade itself. Assuming that the primary vertex is being calculated correctly, what one would expect to see is that when the cascade is traced back to the primary vertex position its y and z coordinates at that point should compare favourably with the calculated y and z coordinates of the primary vertex. To test this, a plot of the $\Lambda\pi$ mass against the impact parameter in y (ie. the difference between the traced back cascade and the primary vertex point) can be plotted. Such a plot is shown in figure 4.10 for all candidates which survived the previous cuts on the decay vertices. This plot confirms that the vertex finding seems good, because it quite clearly shows the true Ξ candidates clustered in a tight circle about zero impact parameter. Cutting on this quantity is therefore a very powerful tool when removing background and leads to the following cut in B_y

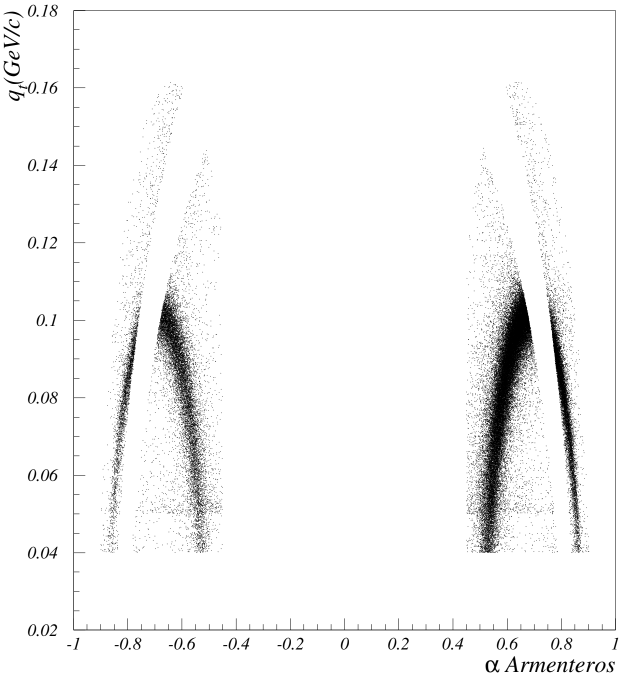

Figure 4.7: Armenteros-Podolanski plot of q_t versus α Armenteros for remaining Λ and $\overline{\Lambda}$ candidates before final mass cuts.

- The cascade must trace to within 0.3 cm of the primary vertex in y.

A similar plot can be performed in the z direction. A plot of the $\Lambda\pi$ mass as a function of impact parameter in the z direction is shown in figure 4.11. This leads to a similar cut in the value of B_z

- The cascade must trace to within 0.13 cm of the primary vertex in z.

These impact parameter cuts provide a good test of which events were true Ξ and Ω decays, but other useful cuts can be performed on the two cascade decay tracks. Since both the V^0 and charged track come from the cascade decay rather than the interaction vertex, one would expect that, in general, both decays tracks would miss the primary vertex by some distance when traced back. Once again, the bend direction tends to provide the best means of selecting out good candidates and so both the V^0 and charged track can be traced back to the x coordinate of the primary vertex and their impact parameters in

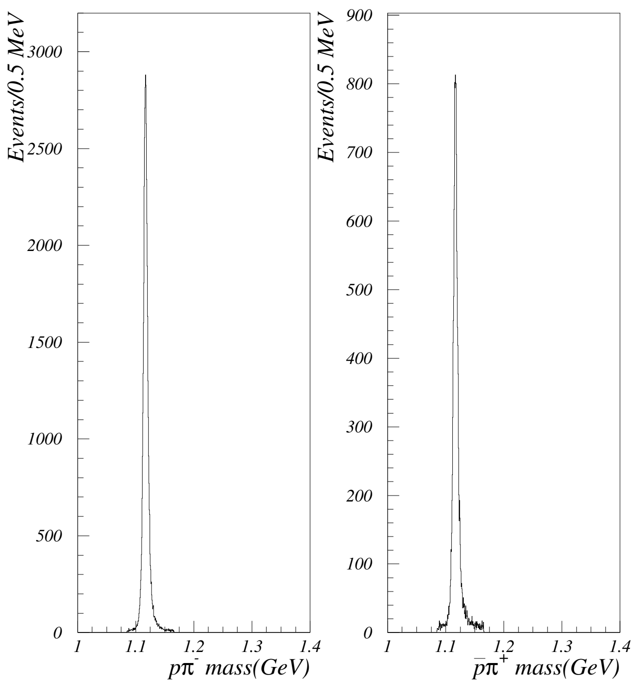

Figure 4.8: $p\pi^-$ effective mass spectrum for $\alpha > 0$ (left), and $\overline{p}\pi^+$ effective mass spectrum for $\alpha < 0$ (right).

y found. Figure 4.12 shows the $\Lambda\pi$ effective mass distribution as a function of the impact parameter B_y of the V^0 track for those remaining candidates after the impact parameter cuts on the cascade itself have been made. Figure 4.13 shows the same plot, except that on the horizontal scale the impact parameter is that for the charged track rather than for the V^0.

At this stage of the selection cuts a fairly high proportion of the remaining candidates are good Ξs, and a number of interesting features are visible in the two plots. Firstly, it can be seen that the band of good candidates (ie. those with a reconstructed $\Lambda\pi$ mass close to the PDG Ξ mass) is indeed spread over a wide range of impact parameters for the V^0 and charged track. This of course corresponds to the respective tracks missing the point of origin of the cascade when they trace back to the primary vertex. Since some of these impact parameters are quite large, it therefore also proves that for most of the good candidates the V^0 definitely does not originate from the primary vertex and

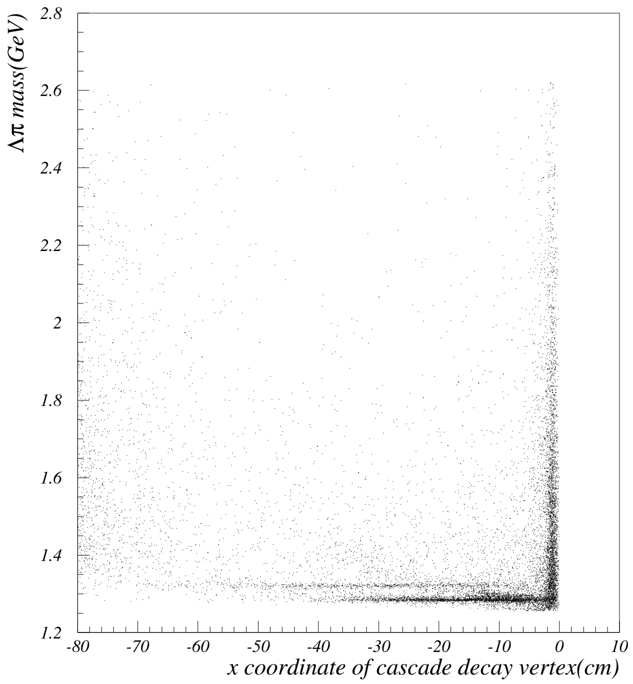

Figure 4.9: $\Lambda\pi$ effective mass against x coordinate of the cascade decay vertex.

that the remaining background events seem to be from a track configuration where both the fake cascade and its decay tracks have very little opening angle between them. The other main interesting feature of the horizontal bands is that they are not symmetric either side of zero: for the V^0 track the distribution is more heavily weighted (in terms of number of events) on the negative side and for the charged track the distribution is more heavily weighted on the positive side. This is due simply to the decay topologies taken, the fact that only cowboy decays are considered, and the restrictions this then places on which side of the primary vertex the two decay tracks will fall for particles and anti-particles respectively. It turns out that for a cascade decay the charged track tends to fall on the positive side of zero when it gets traced back. For an anti-cascade decay on the other hand, the charged track falls on the negative side of zero (and vice versa for the V^0 track). This unequal weighting, therefore, simply reflects the grouping of particles and anti-particles respectively. The two final cuts on these parameters to remove most of the remaining background are

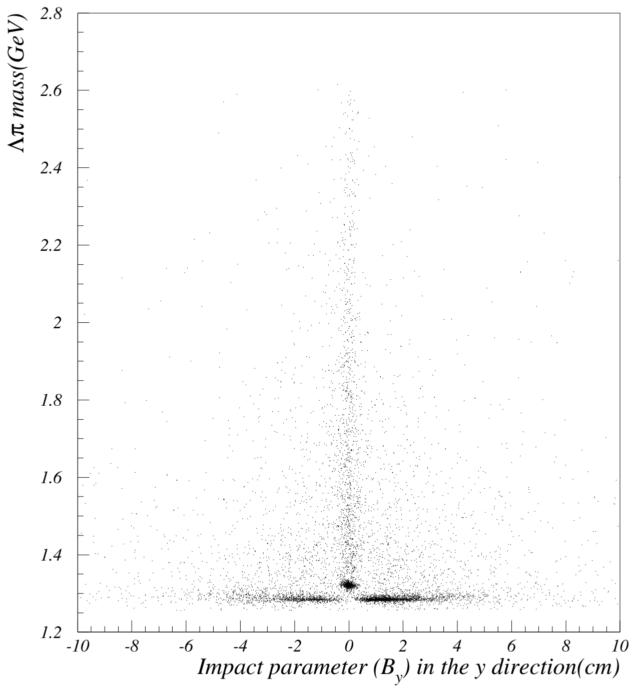

Figure 4.10: $\Lambda\pi$ effective mass against impact parameter B_y.

- The V^0 must miss the primary vertex by more than 0.14 cm in y (ie. $|B_y(V^0)| > 0.14$ cm).

- The charged decay track must miss the primary vertex by more than 0.4 cm in y (ie. $|B_y(track)| > 0.4$ cm).

At this stage the remaining signal of Ξs is fairly clean, as can be seen in figure 4.14, where the PDG value of the Ξ mass lies between the two most populated bins. Of those events that appear to be background, a reasonable proportion are actually the Ωs and so only a few further cuts are needed to define the Ξ sample.

The last type of cuts required are those that ensure the cascade candidates come from the target itself. Of course for the majority of events this will be the case, but a small trace of events can come from interactions with the atoms in air molecules and so on, which makes this cut neccessary. Figure 4.15 shows the vertex distribution in the x direction for the remaining cascade candidates. This distribution is both more narrow, and also has

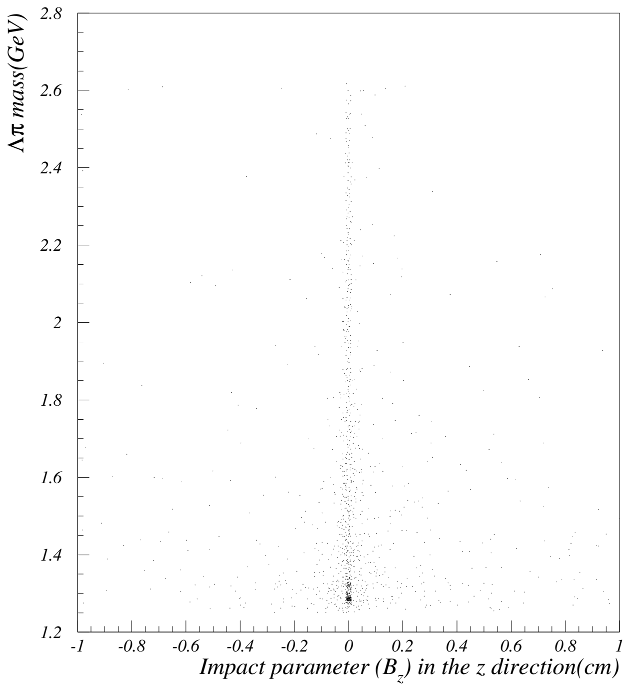

Figure 4.11: $\Lambda\pi$ effective mass against impact parameter B_z.

a much lower proportion of background than the plot that was shown at the end of the previous chapter. A small trace of events appear to come from outside of the target, but in general this number is small and a reasonable cut can be made on this quantity.

The vertex distributions in the other two directions can now also be looked at. Of course in these directions the respective distributions should both be small in size due to the size of the beam spot. The distribution in the y direction is shown in figure 4.16 and figure 4.17 shows the distribution in the z direction.

Given these distributions, the following cuts are then applied to ensure that the cascade comes from the target

- The x coordinate of the reconstructed primary vertex must lie within 5 cm of the database value in x (x_Ω = -91.6 cm).
- The y coordinate of the reconstructed primary vertex must lie within 0.4 cm of the database value in y ($y_\Omega = 0$ cm).

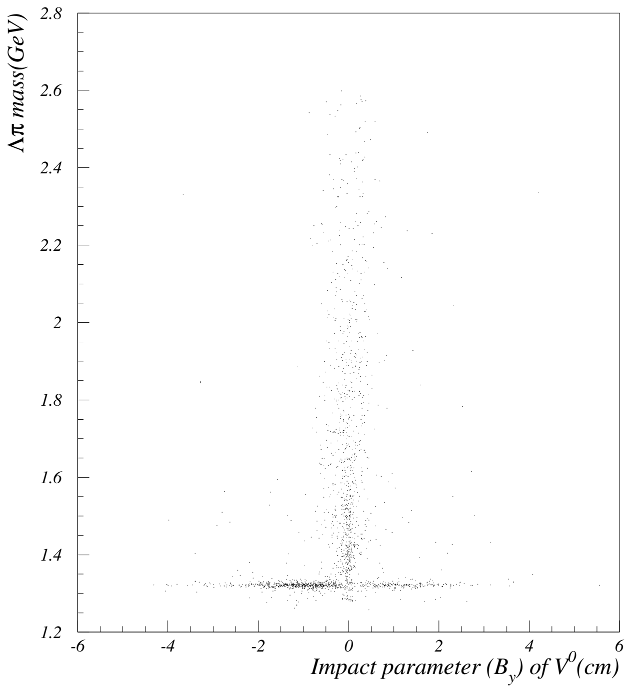

Figure 4.12: $\Lambda\pi$ effective mass against impact parameter B_y of the V^0.

- The z coordinate of the reconstructed primary vertex must be less than $z_\Omega =$ 0.2 cm.

At this stage a number of checks can be performed on the remaining sample. Since the beam passes through the target in the x direction, one would expect the width of the primary vertex distribution in x for the remaining candidates to be comparable to the real width of the target. Figure 4.18 shows a Gaussian fit to this distribution. While the distribution itself is not quite a true Gaussian, such a fit still gives a reasonable measure of the distribution thickness. The fit gives a full width at half height of 3.6 cm, which compares fairly well to the actual 3.2 cm thickness of the target, especially given the approximate nature of the fit. Indeed, the true width (at a half height of about 26 on the vertical scale) seems from the plot to be closer to 3.0 cm. The peak's mean value of -91.5 cm also agrees well with the value that was chosen for the nominal (ie. database) target position in x, which was -91.6 cm.

Similar plots can be made in the y and z directions, except that this time one would

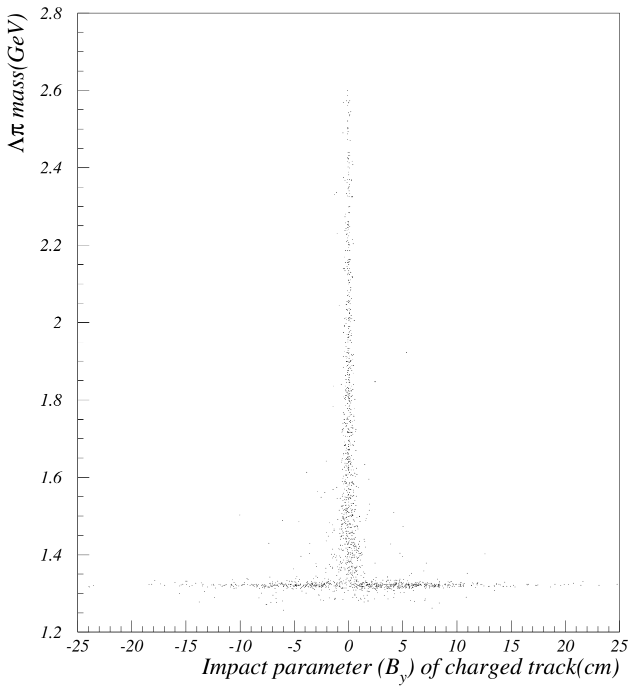

Figure 4.13: $\Lambda\pi$ effective mass against impact parameter B_y of the charged track.

expect the distributions to be comparable to the width of the beam as it enters the target. Figures 4.19 and 4.20 show the widths of the distributions for the remaining candidates in y and z respectively. The widths of both peaks are around 2.5 mm at FWHM, and this corresponds well to the known size of the beam spot. The vertex finding was also checked by two other separate methods to ensure its validity. These methods used fitting tracks to helices or elipses and then minimising the closest approach between the beam track and hyperon. Both methods were found to give almost identical values for both the width and mean values of the vertex distributions. Most individual events also agreed closely on an event-by-event basis.

Once the final vertex cuts have been performed, this gives a final $\Lambda\pi$ effective mass distribution as shown in figure 4.21. The sample is now fairly clean and has relatively little background. Therefore, a mass cut can now be applied to select out the gold-plated Ξ sample. Gold-plated Ξs are taken as those remaining candidates which have a reconstructed $\Lambda\pi$ mass that lies within 20 MeV of the PDG value for the Ξ mass (1.321

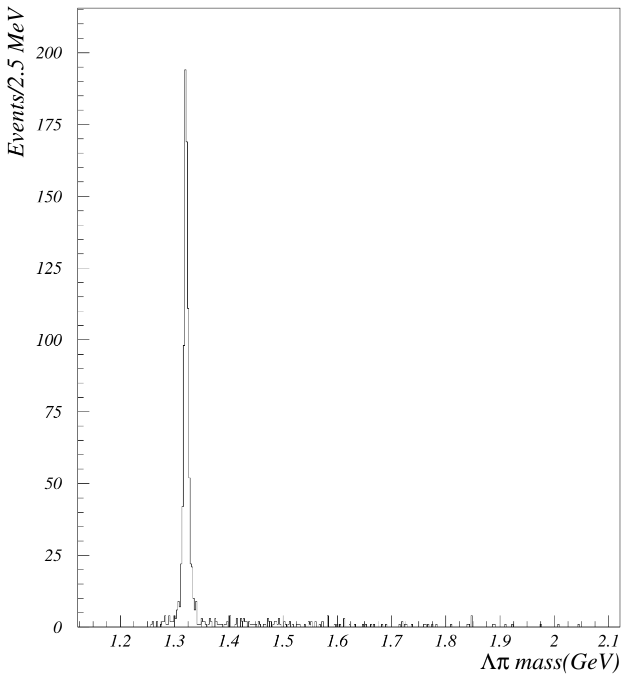

Figure 4.14: $\Lambda\pi$ effective mass spectrum after the application of all previous cuts.

GeV).

4.3.2 Ω Selection Cuts

Now that the gold-plated Ξ signal has been selected, a reasonable Ω signal (possibly still with a little background) should be visible from the remaining events in the sample. Figure 4.22 shows a plot of the ΛK effective mass against the $\Lambda\pi$ effective mass for those events shown in figure 4.21. This of course shows the huge vertical Ξ peak shown in figure 4.21, but a horizontal Ω signal is also visible, albeit with some background.

A plot of the ΛK effective mass for those candidates which are not considered gold-plated Ξs is shown in figure 4.23. This shows the Ω peak at the right mass, but with some background. Looking at the plot one would expect maybe 30 to 35 events to remain after background subtraction. To attempt to do this, three further cuts on Armenteros variables are then used to clean up the remaining Ω signal. These cuts are

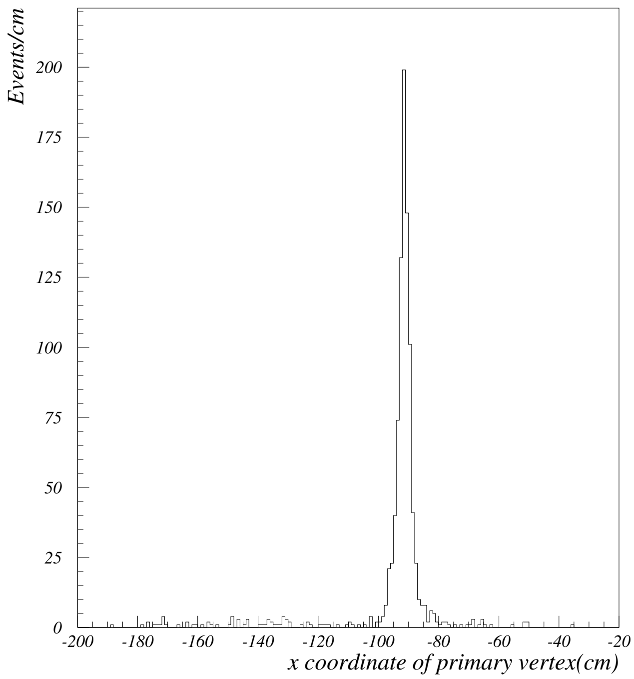

Figure 4.15: Primary vertex distribution in the x direction before vertex cuts.

- For the cascade, $0.2 \leq |\alpha| \leq 0.6$.
- For the cascade, $0.12 \leq q_t$.
- For the V^0, $0.032 \leq q_t$.

This leaves a ΛK effective mass spectrum as can be seen in figure 4.24. Note that there now appears to be very little background. A final mass cut is then applied to the Ωs, requiring that the reconstructed ΛK mass lies within 30 MeV of the PDG value for the Ω mass. The final number of gold-plated $\Omega^- + \overline{\Omega}^+$ in the sample is 33.

By use of the Armenteros-Podolanski variable α, it is also possible to separate cascades from anti-cascades and so make separate mass plots for Ξs and $\overline{\Xi}$s respectively. Figure 4.25 shows the $\Lambda\pi$ effective mass plot for cascades on the left and anti-cascades on the right, after all cuts have been performed except for explicit mass cuts. After a mass cut is applied about the PDG value of the Ξ mass, 397 gold-plated Ξ^- events remain in the

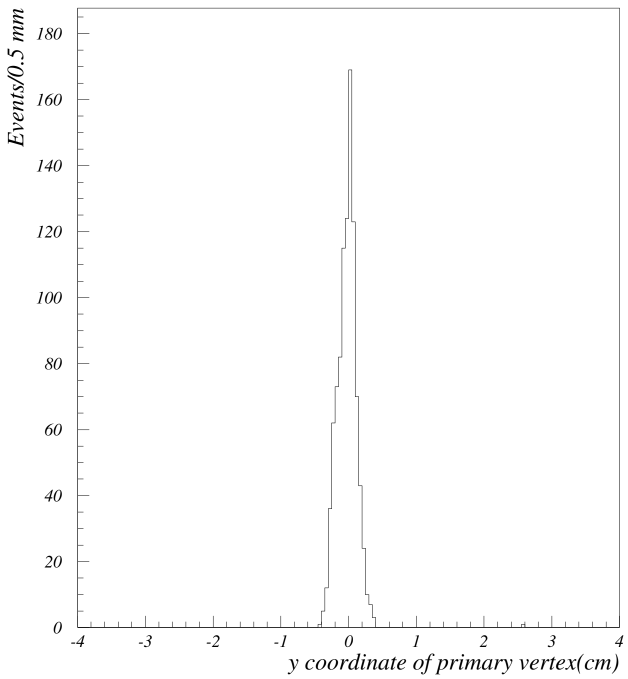

Figure 4.16: Primary vertex distribution in the y direction before vertex cuts.

cascade sample and 157 gold-plated $\overline{\Xi}^{+}$ events remain in the anti-cascade sample. Note this compares well with the original estimate of approximately 550 $\Xi^{-} + \overline{\Xi}^{+}$ predicted at the end of the previous chapter, which indicates that the additional cuts have removed background without losing signal. Table 4.1 shows a comparison of these numbers with the numbers of such events found in the p-Pb and Pb-Pb samples. The numbers in brackets indicate the full data sample has not yet been processed for that particle type. It also indicates the approximate increase in statistics expected from the full sample (eg. "$\times$ 2" indicates that the number quoted comes from having processed half of the data that is available on tape). The final chapter of this thesis will go on to discuss how physics results are extracted from these final samples of events. It will also look at the implications these results have when compared to the results presented in chapter 1.

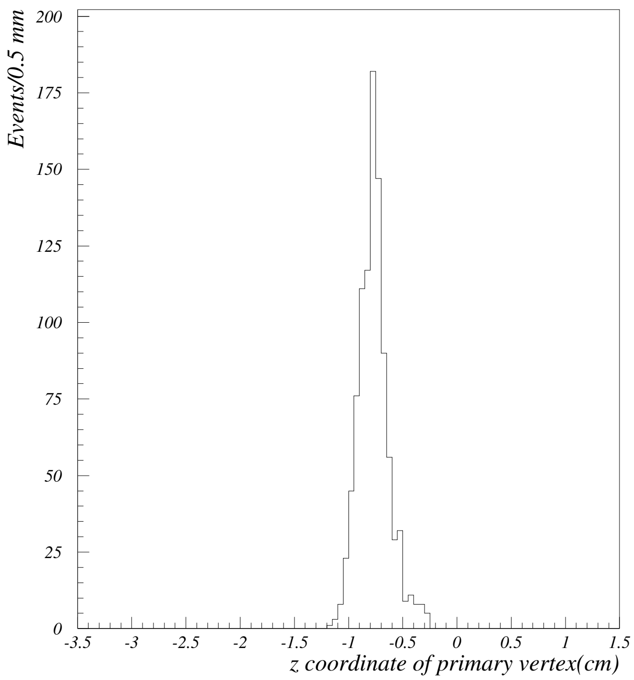

Figure 4.17: Primary vertex distribution in the z direction before vertex cuts.

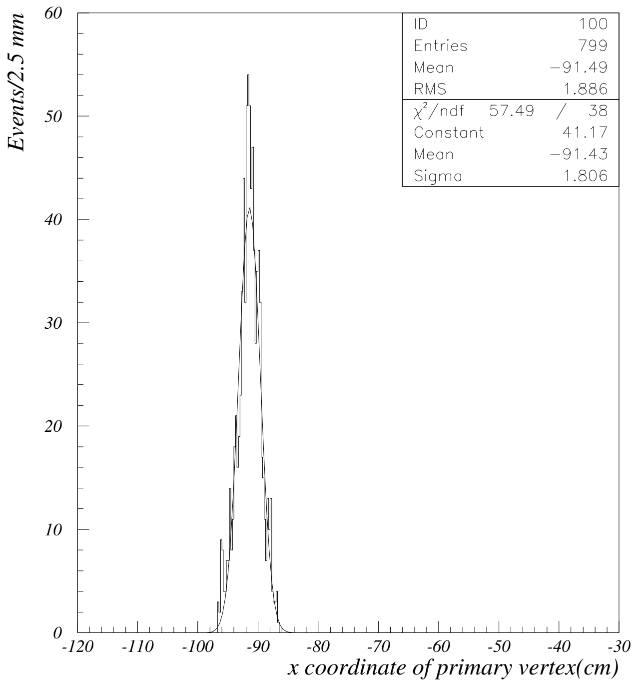

Figure 4.18: Primary vertex distribution in the x direction after vertex cuts.

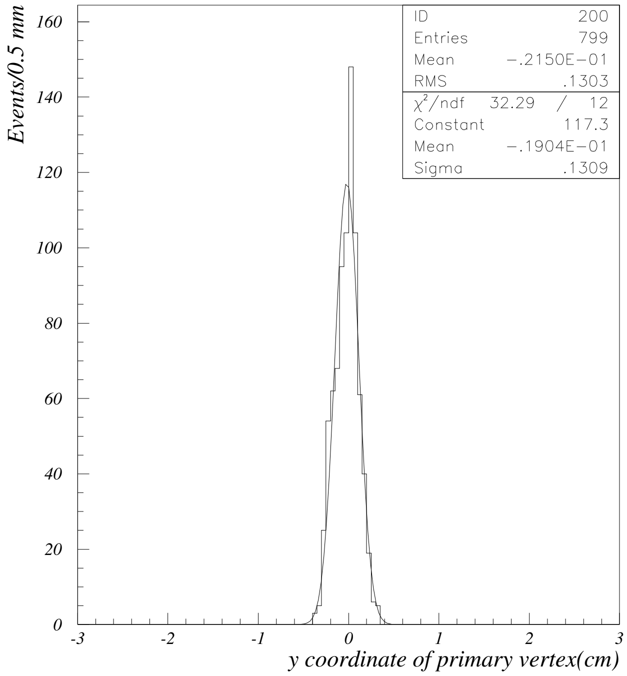

Figure 4.19: Primary vertex distribution in the y direction after vertex cuts.

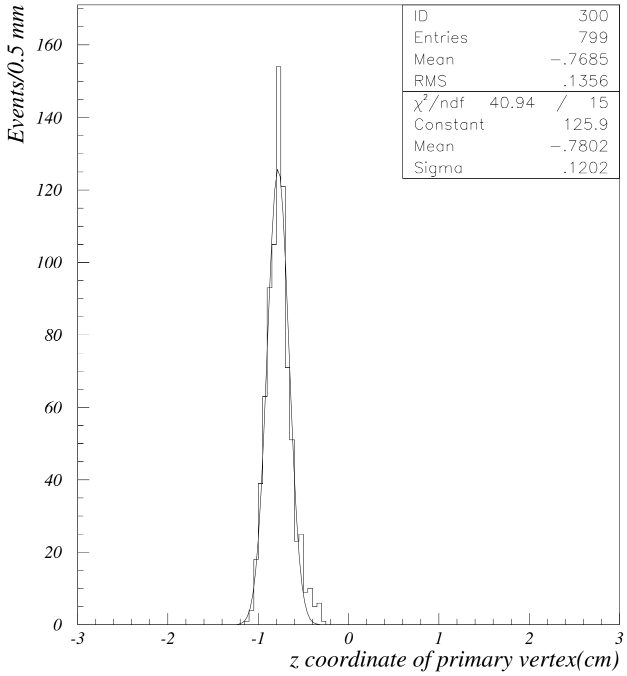

Figure 4.20: Primary vertex distribution in the z direction after vertex cuts.

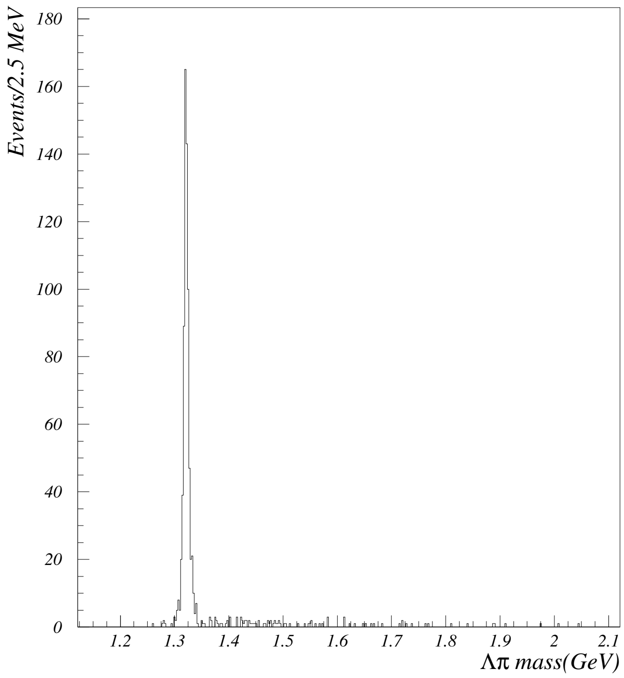

Figure 4.21: $\Lambda\pi$ effective mass spectrum before final mass cut.

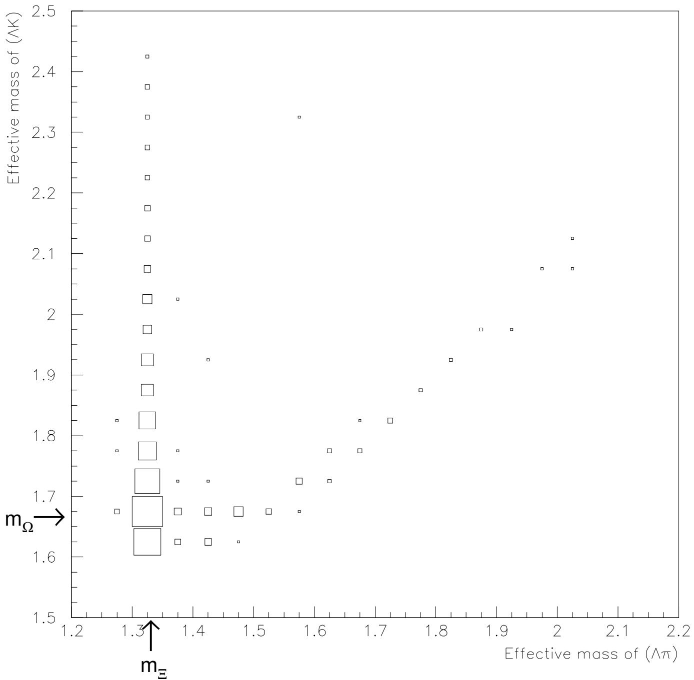

Figure 4.22: ΛK effective mass versus $\Lambda\pi$ effective mass for the events in figure 4.21.

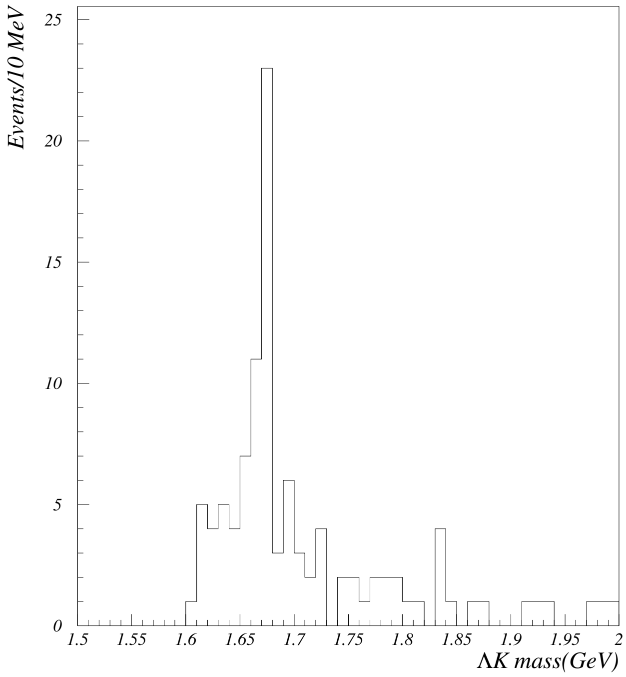

Figure 4.23: ΛK effective mass spectrum after gold-plated Ξs are removed from the sample.

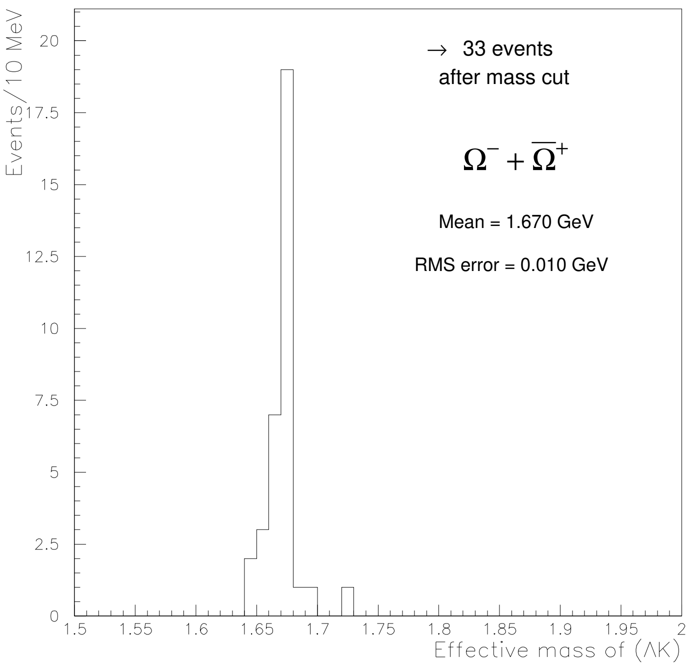

Figure 4.24: ΛK effective mass spectrum before final mass cut.

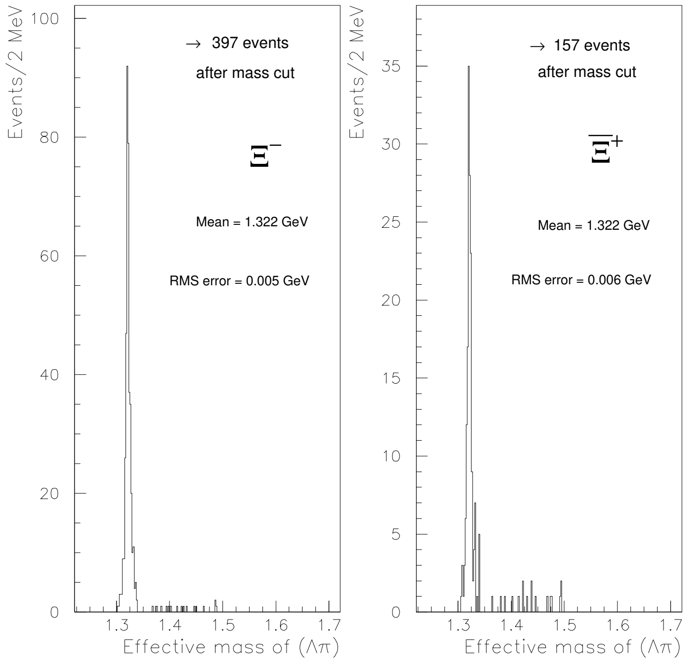

Figure 4.25: $\Lambda\pi$ effective mass spectrum for cascades (left) and anti-cascades (right).

Table 4.1: Number of hyperons found in the different data samples.

	p-Be	p-Pb	Pb-Pb
$\Omega^- + \overline{\Omega}^+$	33	19	203 ($\times$ 2)
Ξ^-	397	275	1346 ($\times$ 2)
$\overline{\Xi}^+$	157	101	339 ($\times$ 2)
Λ	119,320	1056 ($\times$ 100)	1868 ($\times$ 350)
$\overline{\Lambda}$	34,349	243 ($\times$ 100)	669 ($\times$ 150)

Chapter 5

Strangelets and the Ω Hyperon

This chapter takes a more detailed look at two of the somewhat more exotic particles that may be produced in heavy ion collisions; strangelets (discussed briefly in chapter 1), and the triply-strange Ω baryon. Although a signal of Ωs is visible in the proton data discussed in the previous chapter, a truly good signal can only be obtained when one goes to heavy ion interactions, where one can more quickly build up the necessary statistics. The first part of this chapter, therefore, concentrates on strangelets and a search for the H^0 dibaryon in the WA85 S-W data. The second part of the chapter concentrates on the WA97 Pb-Pb data and the Ω hyperon.

5.1 Strangelets

Work from Witten *et al* [33] has shown that strange quark matter may be inherently more stable than ordinary nuclear matter. Indeed, bag model calculations have shown that droplets of nuclear matter of relatively low baryon number may be stable. Such droplets are known as *Strangelets.* Although a multitude of such objects could exist, the simplest is the H^0 dibaryon proposed by Jaffe [48], which consists of six quarks (two up, two down and two strange). Such particles could be formed in a Quark-Gluon Plasma with non-zero baryon number. Therefore, heavy-ion collisions at the CERN fixed target experiments form an ideal environment in which to search for such particles.

However, the search for the H^0 is dependent on its decay modes, which are themselves dependent on the mass of the particle. If the H^0 has a mass greater than twice the Λ mass, then it should decay strongly via the mode $H^0 \rightarrow \Lambda\Lambda$. If its mass is lower than the $\Lambda\Lambda$ threshold, however, then it should decay weakly into $\Sigma^- p$, $\Sigma^0 n$, or Λn.

Therefore, if the H^0 decays strongly (ie. has a mass $> 2m_\Lambda$) a resonance should be seen in the effective mass of $\Lambda\Lambda$ for those events in which two Λs were found. One would also expect an increase in the number of such dilambda events relative to the background from two Λs being produced independently.

5.2 A Search for H^0 using WA85 Experimental Data

From a selection of 60 million central S-W triggers, 57069 Λs were found. Therefore, the probability of a single Λ being reconstructed is $\frac{57069}{60\times10^6} \sim 10^{-3}$ or 0.1%. The probability of two such Λs occuring randomly, therefore, should be this number squared (ie. 10^{-6}, or 0.0001%), which means that from 60 million triggers one would expect $\sim$ 60 events to contain two Λs merely from statistics. If the H^0 is being produced with significant cross section, one would expect an enhancement in the number of events containing two Λs (i.e. more than 60). However, a search through the 60 million triggers revealed only 31 events containing two Λs, so no enhancement was seen. The other thing one might expect is a resonance in the $m_{\Lambda\Lambda}$ from those events which contained two Λs. Figure 5.1 shows the $\Lambda\Lambda$ effective mass spectrum for the 31 events which were actually found in the data.

This should be compared with the expected phase space background. This is done by plotting the effective masses for completely *uncorrelated* Λs (i.e. those from different events) and so can be done from the single Λ events by combining the Λ found in the first of the 57069 events with the Λ found in the second of these events and plotting their

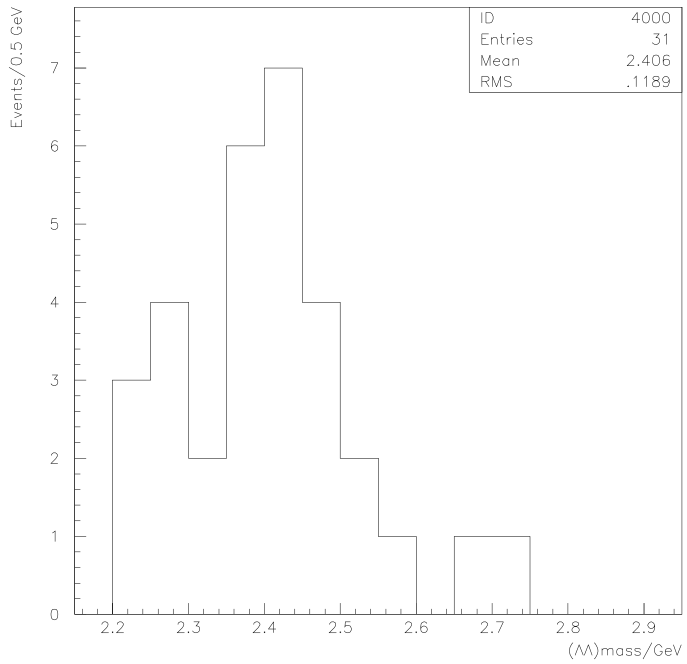

Figure 5.1: $m_{\Lambda\Lambda}$ for the 31 $\Lambda\Lambda$ events found in the WA85 S-W data sample.

effective mass, then doing the same for the 2nd and 3rd, 3rd and 4th, and so on. Figure 5.2 shows the effective mass of two Λs by using the 57069 single Λ events in this manner.

In order to compare the two plots, they must be normalised to contain the same area. Therefore, the phase space background was normalised to contain 31 events as in the actual data and the two plots were overlaid for comparison. Figure 5.3 shows the two plots on the same scale.

Of course because of the low number of events it is almost impossible to draw definite conclusions, but, within errors, no resonance can be claimed. That, combined with no enhancement in the number of events containing two Λs indicates that no evidence for the H^0 dibaryon has been found in these data. This would indicate that the cross-section for H^0 production in these events is lower than that required to observe it with these statistics, or that its mass is less than twice the Λ mass. Obviously greater statistics are desirable, although a similar analysis on the WA97 data has thus far also yielded null results [49].

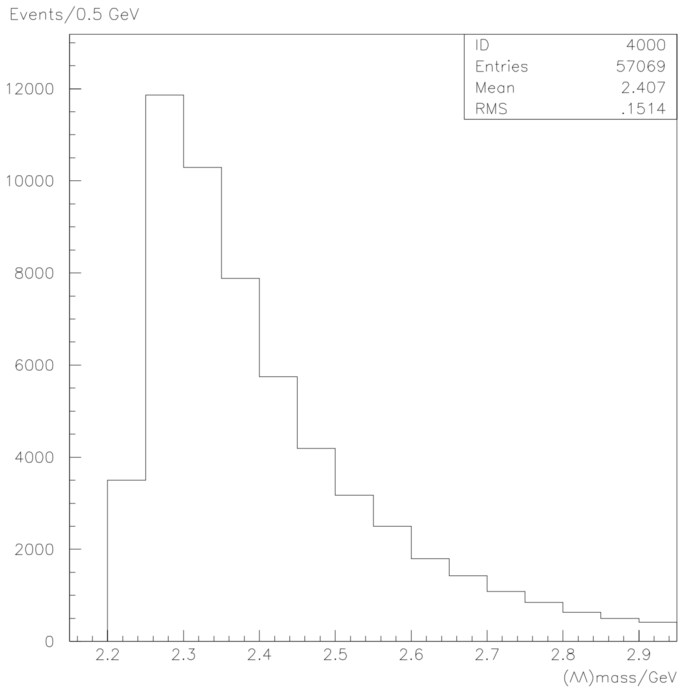

Figure 5.2: $m_{\Lambda\Lambda}$ found by mixing the 57069 uncorrelated single Λs.

5.3 The Ω Hyperon

The WA97 experiment concerns itself with identification of the strange hyperons Λ, Ξ^- and Ω^-, and their corresponding anti-particles. As has already been mentioned, the Ξ^- and Ω^- themselves decay weakly into a Λ and either a pion (for the Ξ), or a kaon (for the Ω). The Ξ^- and Ω^- particles are also collectively known as "cascades", and their anti-particles as "anti-cascades". Figure 5.4 shows an effective mass plot for WA97 cascade candidates from the 1995 Pb-Pb run, with loose cuts similar to those in Chapter 3 applied. On the horizontal axis is plotted the effective mass of the candidate as if it were a Ξ, and on the vertical axis the corresponding effective mass as if it were an Ω. The resulting plot shows several interesting features, including the lower limits governed by minimum masses, and the straight line to which the plot tends at higher effective masses, when the difference between m_Ξ and m_Ω becomes less significant.

Cuts can be performed on this plot in order to separate the Ξ and Ω candidates out

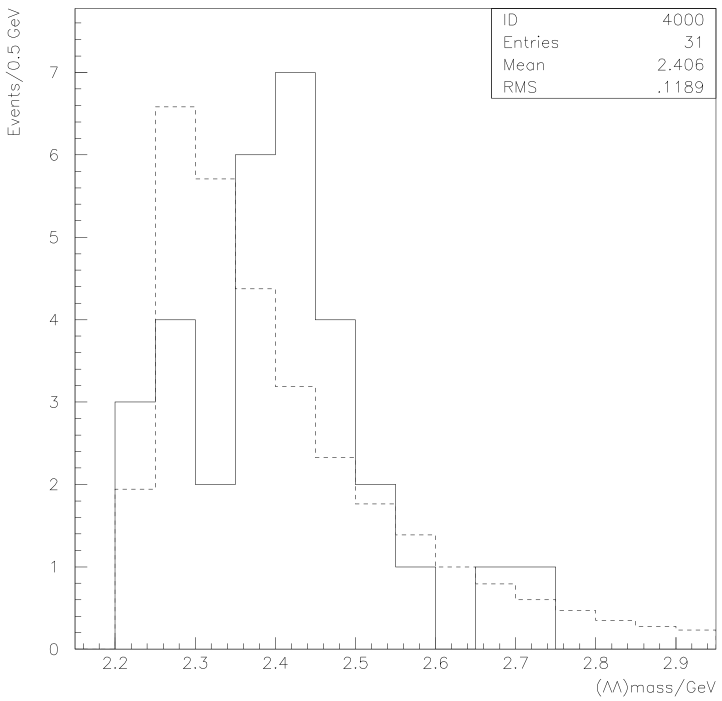

Figure 5.3: The two $m_{\Lambda\Lambda}$ plots normalised to contain the same area and superimposed.

into distinct bands, as shown in the previous chapter for the p-Be data. A list of these cuts follows, along with the reason for using each one

- The x coordinate of the cascade decay vertex is greater than -40 cm.
- The x coordinate of the V^0 decay vertex is greater than -30 cm.
- The x coordinate of the V^0 decay vertex is greater than that of the cascade decay vertex.

These cuts ensure that the decay vertices occur downstream of the target and, moreover, that the V^0 decay occurs downstream of (ie. after) the cascade decay. Note that for the Pb-Pb data the target was located closer to the silicon telescope than for the p-Be data (x_Ω = -60 cm, as opposed to x_Ω = -90 cm for p-Be).

- For a cascade decay, the reconstructed Λ mass lies within 7.5 MeV of the PDG value.

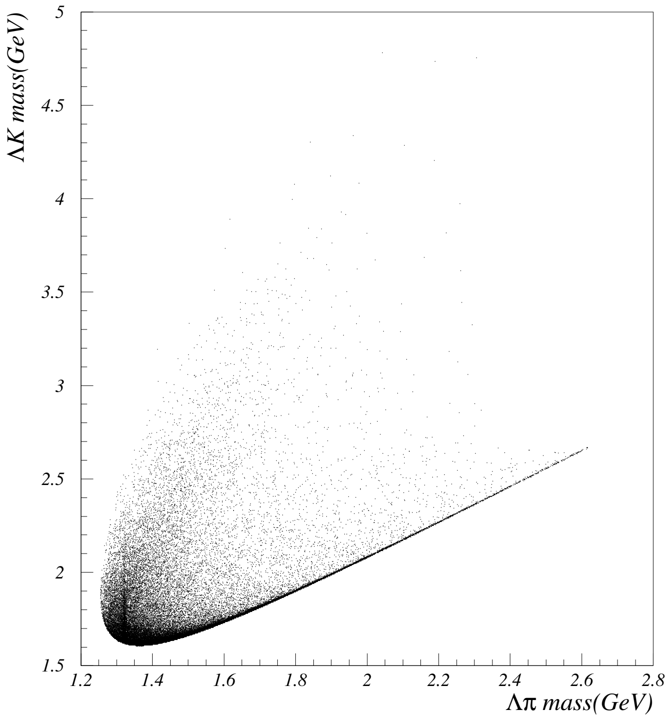

Figure 5.4: ΛK effective mass versus $\Lambda\pi$ effective mass for loosely cut cascade candidates from the 1995 Pb-Pb run.

- For an anti-cascade decay, the reconstructed $\overline{\Lambda}$ mass lies within 7.5 MeV of the PDG value.

Hence these two cuts compare the mass of the V^0 to the accepted value for a Λ or $\overline{\Lambda}$, ensuring a "good" V^0.

- The y impact parameter of the cascade must be less than 0.4 cm.

- The z impact parameter of the cascade must be less than 0.4 cm.

These form a selection of cuts to ensure that the cascade comes from the target, as with several of the cuts in the previous chapter.

- The charged decay track misses the nominal y position of the target by at least 0.5 cm.

- The V^0 decay track misses the nominal y position of the target by at least 0.1 cm.

These last two cuts ensure that the cascade decay tracks miss the primary vertex, even though the cascade itself is required to trace back to the vertex. This minimises any problems that might be caused by V^0s coming from the target, which is more of a problem with the Pb-Pb data than it is with the p-Be, simply because of the much higher multiplicities. The y direction is of course the magnetic bend direction, meaning that the signs change according to whether we have positive or negative charged particles.

Applying these cuts to the data in figure 5.4 gives the plot shown in figure 5.5. This shows that the data points separate into distinct bands - those which are Ξs with a high likelihood and those which we can say are Ωs with a high likelihood. The WA85 experiment was the first heavy ion experiment to reconstruct Ωs among its cascade particles [50] and now much greater statistics are available from the WA97 data - particularly of course in Pb-Pb collisions.

One further cut can then be applied in order to produce a separate mass plot for the Ω. Obviously this needs to be a cut which will remove most of the Ξs, as was shown in the previous chapter. This can be accomplished by making a cut about the mass of the Ξ as given in the PDG. Thus the final cut is

- The reconstructed $\Lambda\pi$ mass lies more than 20 MeV from the PDG value.

This cuts out cascade candidates whose $\Lambda\pi$ effective mass is within 20 MeV of the accepted Ξ mass, so it should leave candidates which are almost exclusively Ωs. Figure 5.6 shows the plot with this final cut applied. Only the Ω band can now be seen clearly, so all that is left to do is project this onto the ΛK axis (ie. plot the effective mass as a reconstructed Ω for these remaining events).

The final Ω mass plot is shown in figure 5.7 and shows a clear peak at the PDG value of the Ω mass with little background. Such plots are difficult to obtain with proton

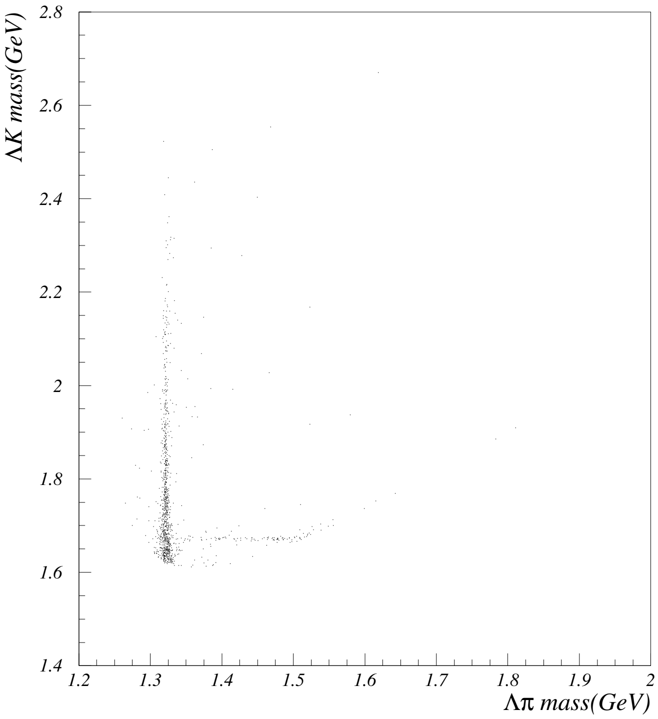

Figure 5.5: ΛK effective mass versus $\Lambda\pi$ effective mass.

induced interactions because of the much increased running time required to integrate up the same level of statistics for the Ω. Analysis of the proton induced interactions is still vital as a control sample, however, because without them there can be no comparison with conventional hadronic interactions.

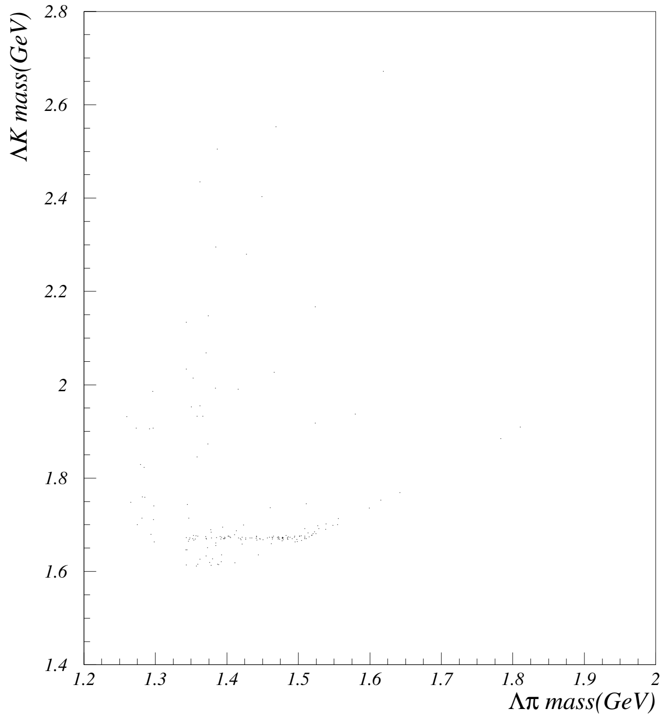

Figure 5.6: ΛK effective mass versus $\Lambda\pi$ effective mass after cuts to leave only Ω candidates remaining.

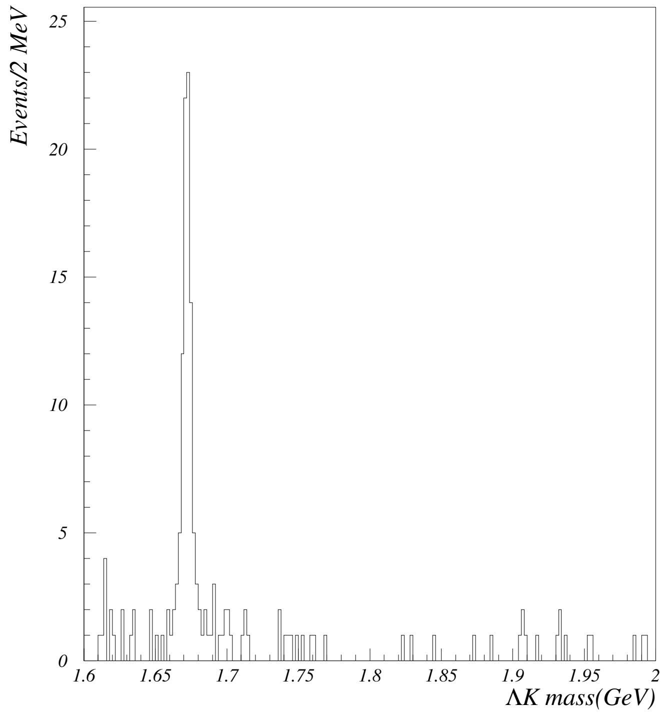

Figure 5.7: ΛK effective mass plot obtained from projecting the Ω candidates onto the $m_{\Lambda K}$ axis.

Chapter 6

Results

Once final gold-plated events have been obtained, the next stage of data processing is to correct for those events which have not been found by the analysis chain or by the detector. There are obviously many hyperons which will not pass through the small solid angle subtended by the silicon telescope and so corrections for geometrical acceptance are needed. Likewise, there will be some hyperons which will pass through the silicon telescope but may not be reconstructed successfully by the WA97 track finding routines and other aspects of the analysis chain. This leads to the need for a reconstruction efficiency for each event and the concept of event "weighting". Two other points which need to be considered in such calculations are the efficiency of the detectors and the unseen decay modes (eg. $\Lambda \rightarrow n\pi^0$). While it is true that WA97 uses a small detector, it is by virtue of this detector and the WA97 trigger that the WA97 experiment has managed to obtain such high statistics of the rare Ξ and Ω events. In fact, at the time of writing, WA97 has more than 10 times as many Ωs as all of the other heavy ion experiments in the world put together. This is crucial, because one of the clear predictions of QGP theory is that Ωs should be enhanced more than Ξs when one goes from a hadron gas to a QGP scenario, and similarly, that Ξs should be enhanced more than Λs. Therefore, lacking statistics for Ωs (or even Ξ events, which tend to be quite rare in their own right), no other heavy ion experiment can test this hierarchy in the same way that WA97 can.

6.1 The WA97 Weighting Chain

Weights correct for effects such as geometrical acceptance or reconstruction efficiency, by assigning a "true" value to the number of particles that were produced in an interaction. For example, if a particle of a given rapidity and p_T had a weight of 10, it means that for every particle detected of that same rapidity and p_T there were 9 others which were not found due to geometrical acceptances, other decay modes, detector efficiencies, reconstruction efficiencies, and so on. Therefore, once weighting has been performed, one can obtain a value for the total number of particles found in any given acceptance region by summing the weights of all the particles that lie within that region. What follows is a brief description of each part of the WA97 weighting chain.

6.1.1 The GEANT Event Generator

The first part of the weighting chain is to generate Monte Carlo particles of the appropriate type, with the same p_T and rapidity as an event that was found in the real data sample (although some smearing of p_T and rapidity are allowed, to account for the resolution of the detector and multiple scattering). A GEANT based simulation of the apparatus is then used to let the generated particles decay, and pass their decay tracks through the silicon telescope, implanting hits in the telescope's pixel planes. Planar efficiencies for the pixel planes are calculated, previous to this, by calculating how often real tracks have a hit in a given plane.

6.1.2 The MC-TO-RAW Event Mixing Program

The generated Monto Carlo particles (or rather, their hits in the silicon telescope) are then implanted into raw background data that come from events close to the run number in which the real particle was found. Therefore, the output from this stage of the weighting chain is a data file of the same format as the background data, but with the hits from the generated particles implanted on top of it.

6.1.3 ORHION Track Finding

After the Monte Carlo events have been implanted into background events to give files of the same format as real data, the next two stages of the weighting chain are the same as those used in normal data processing. First comes the track finding program ORHION, which reconstructs tracks from the hits in the data file and will reconstruct the generated particles' decay tracks in a number of cases. The data now consists of tracks, but no reconstructed particles at this stage.

6.1.4 ANALYZE or CASCADE Particle Finding

As with the real data, the ORHION output is then passed onto the V^0 and cascade finding programs. These programs attempt to form V^0s and cascades from the tracks that were reconstructed by ORHION. At the weighting chain stage they also contain all of the cuts for selecting out gold-plated candidates. If one of the Monte Carlo particles is included in the output, it has passed successfully through the entire weighting chain, taking into account geometrical acceptance, detector efficiency, and reconstruction efficiency.

6.1.5 Particle Weighting

The final stage of the weighting chain is the assignment of the weight itself. The program WGTCAL looks at the number of particles generated by the GEANT program, and the number of these that were actually found at the end of the analysis chain (ie. in the ANALYZE or CASCADE program output). The weight of a particle is then defined by the formula

$$weight = \frac{n_{gen}}{n_{found}}$$

where n_{gen} is the number of events that were generated at the GEANT stage of the weighting chain and n_{found} is the number of events that were successfully reconstructed and found in the respective output file at the end of the chain. Of course, the actual weight values vary considerably depending on the particle species, since a negative track is considerably easier to find and reconstruct than a cascade decay. Table 6.1 gives an indication of the approximate size of weights for various different particle species.

Table 6.1: Approximate size of weights for negative hadrons, Λs, Ξs, and Ωs.

	Approximate weight
h^-	~ 20
Λ	~ 800
Ξ^-	~ 1300
Ω^-	~ 1400

6.2 Acceptance Regions

After all of the events have been weighted, the window of good acceptance in p_T and rapidity can then be plotted. Figure 6.1 shows such a plot for the WA97 p-Be Ξ particles on the left, and the Ω particles on the right.

As can be seen, the acceptance windows in p_T and rapidity form a shape which is commonly referred to as an acceptance region. This shape is related to the area of the telescope, and the solid angle which it subtends with respect to the target. The edges of the acceptance window also correspond to the edges of the telescope and for this reason events which occur near to these edges tend to have higher weights associated with them. This is because for these events tracks are slicing through the edges of the detector and,

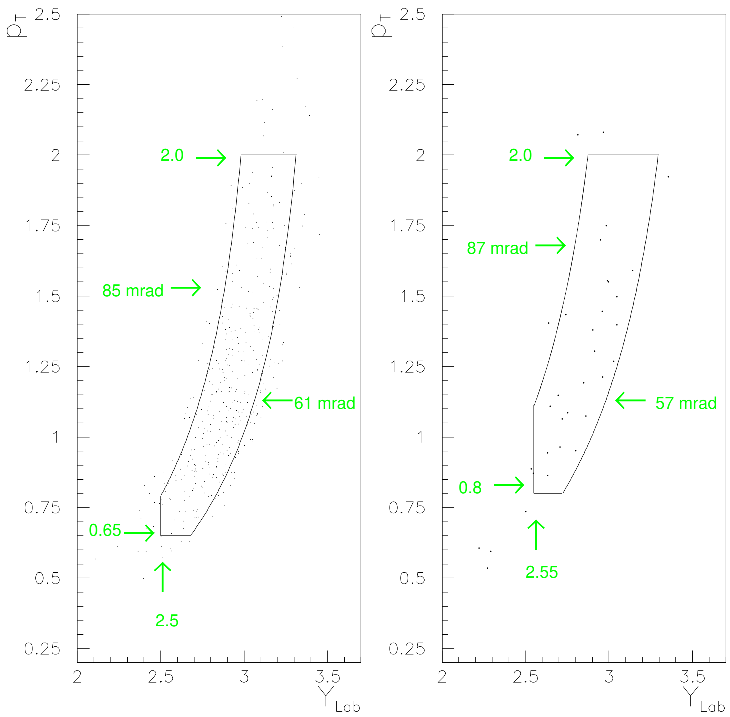

Figure 6.1: Regions of good acceptance for Ξs (left), and Ωs (right).

therefore, will tend to be reconstructed badly when Monte Carlo events are generated. In order to take a good acceptance region, around which to base physics results, it is necessary to form a criterion with which to exclude these events which lie close to the edges. This is done by defining a region of "good acceptance" as one in which the largest weight is up to ten times the size of the smallest weight. This ensures that the weights in the chosen region are fairly uniform and do not vary by more than a factor of ten. The regions of good acceptance are defined by five parameters, namely p_{Tmin}, p_{Tmax}, and y_{min} (which form straight line maxima and minima cuts on the axis values), and the angles θ_{min} and θ_{max}, which are related to the angle of inclination of the telescope. These angles, along with the mass of the respective particle, produce contours in p_T and rapidity space. A derivation of the equation that describes these contours can be found in Appendix C. Table 6.2 shows the parameters that were used in the WA97 Pb-Pb analysis to define the acceptance regions for Λs, Ξs, and Ωs respectively. Table 6.3

shows the corresponding parameters for the p-Be analysis and, in the case of Ξs and Ωs, corresponds to the acceptance regions outlined in figure 6.1.

Table 6.2: y, p_T and θ cuts for Λ, Ξ, and Ω candidates in the WA97 Pb-Pb data.

	θ_{min}	θ_{max}	y_{min}	p_{Tmin}	p_{Tmax}
Λ	47	95	2.45	0.4	2.1
Ξ	48	90	2.45	0.6	2.6
Ω	50	95	2.45	0.7	2.8

Table 6.3: y, p_T and θ cuts for Λ, Ξ, and Ω candidates in the WA97 p-Be data.

	θ_{min}	θ_{max}	y_{min}	p_{Tmin}	p_{Tmax}
Λ	54	84	2.42	0.42	2.7
Ξ	61	85	2.5	0.65	2.0
Ω	57	87	2.55	0.8	2.0

6.3 Fitting of m_T Distributions

Once the regions of good acceptance have been defined for the various particle species it is possible to start obtaining physics results from the data. The fitting of transverse mass distributions give an indication of the temperature reached in the collision since the inverse slope is equivalent to the temperature plus the transverse flow. The transverse mass spectra for Ξ and Ω hyperons were parametised by

$$\frac{dN}{dm_T} \propto m_T^{\alpha} exp(-\frac{m_T}{T})$$

where the transverse mass, m_T, is given by $m_T = \sqrt{p_T^2 + m^2}$, and the value of α is set to either 1 or $\frac{3}{2}$. The fit is performed using the method of maximum likelihood. This fit takes into account the shape of the acceptance window. Figures 6.2 and 6.3 show the p-Be m_T distributions with $\alpha = 1$ for Ξs and $\overline{\Xi}$s respectively. Figure 6.4 shows the corresponding distribution for Ωs and $\overline{\Omega}$s combined.

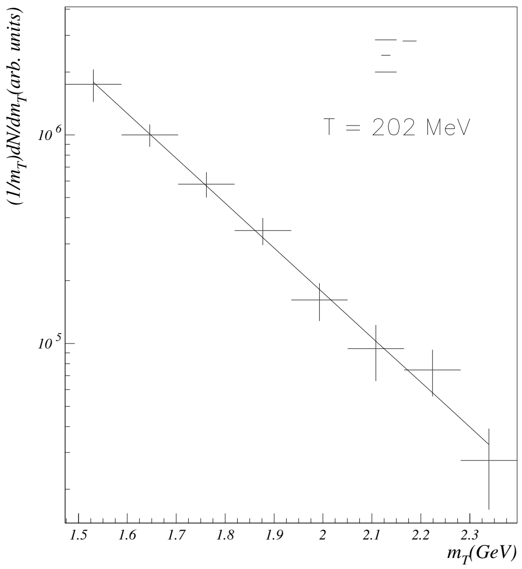

Figure 6.2: Transverse mass distribution for Ξ^- in p-Be interactions.

The inverse slope parameters for Λ, $\overline{\Lambda}$, Ξ^-, $\overline{\Xi}^+$, and $\Omega^- + \overline{\Omega}^+$ in the p-Be, p-Pb, and Pb-Pb data are shown in table 6.4 for $\alpha = 1$, and table 6.5 for $\alpha = \frac{3}{2}$.

Table 6.4: Inverse slopes (in units of MeV) with $\alpha = 1$.

	p-Be	p-Pb	Pb-Pb
Λ	180 ± 3	203 ± 9	291 ± 18
$\overline{\Lambda}$	157 ± 2	180 ± 15	280 ± 20
Ξ^-	202 ± 13	235 ± 14	286 ± 9
$\overline{\Xi}^+$	182 ± 17	224 ± 21	284 ± 17
$\Omega^- + \overline{\Omega}^+$	169 ± 40	334 ± 99	251 ± 19

There appears to be a clear increase in the inverse slope parameter as one moves from proton on light nucleus, to proton on heavy nucleus, and then to heavy nucleus on heavy nucleus. This suggests that somewhat greater temperatures are reached in the bigger collision systems, although one might well expect transverse flow to be greater in those systems as well. It is also interesting to note that the inverse slope for an anti-particle of a particular species tends to lie approximately 10-20 MeV below that for the corresponding

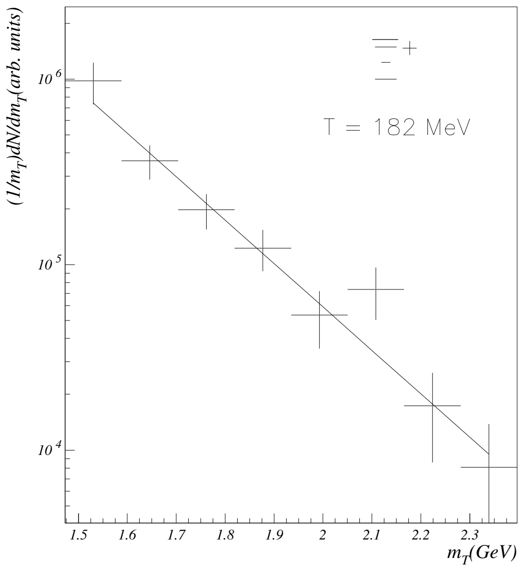

Figure 6.3: Transverse mass distribution for $\overline{\Xi}^+$ in p-Be interactions.

Table 6.5: Inverse slopes (in units of MeV) with $\alpha = \frac{3}{2}$.

	p-Be	p-Pb	Pb-Pb
Λ	170 ± 2	191 ± 8	267 ± 15
$\overline{\Lambda}$	151 ± 2	170 ± 14	257 ± 17
Ξ^-	191 ± 12	222 ± 12	266 ± 8
$\overline{\Xi}^+$	173 ± 16	211 ± 19	265 ± 15
$\Omega^- + \overline{\Omega}^+$	163 ± 36	312 ± 86	238 ± 17

particle of that species, along with the apparently low value of the Ω inverse slope (within statistics). A possible explanation for these effects hinges around the theory that particles with certain resonances (notably with pions, which form the bulk of the emitted particles) tend to be swept along more with the flow - resulting in a higher inverse slope for those particular species.

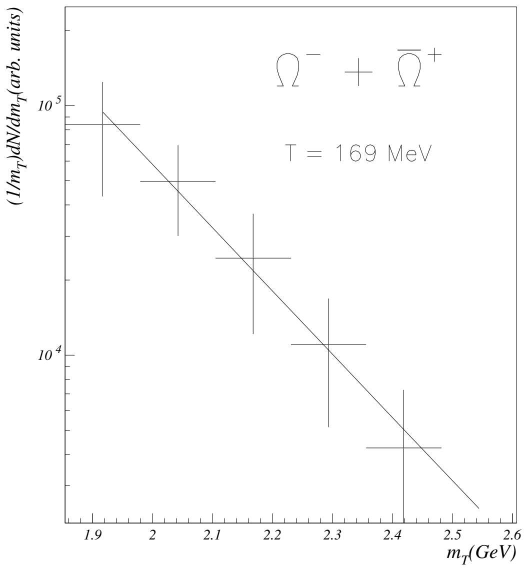

Figure 6.4: Transverse mass distribution for $\Omega^- + \overline{\Omega}^+$ in p-Be interactions.

6.4 Particle Yields

In order to obtain a measure of the average number of particles that are actually produced per interaction, it is first neccessary to extrapolate the data into a common acceptance window that includes those areas about mid-rapidity which are not covered by the experimental acceptance. This extrapolation is performed by binning data in the region of good acceptance, and then extrapolating it while assuming an exponential distribution with respect to p_T, and a flat distribution with respect to rapidity in the central rapidity region. Where the collision system is symmetric (eg. Pb-Pb) the data can also be reflected about mid-rapidity, as is shown in figure 6.5. It can be seen in this figure how the distribution of particles appears to be constant as a function of rapidity in the central rapidity region, and also decreases exponentially as a function of increasing p_T. The particle weights in the good acceptance window were extrapolated to a region $\mid y - y_{cm} \mid < 0.5$ and $p_T > 0$ GeV/c, where y_{cm} is the centre-of-mass rapidity for the nucleon-nucleon system viewed in the lab, and corresponds to Y_{LAB}=2.92. The sum of weights in the original regions of good acceptance, as shown in figure 6.1, correspond to approximately 10% of the size of the weights after extrapolation to this new window about central rapidity, and all of p_T.

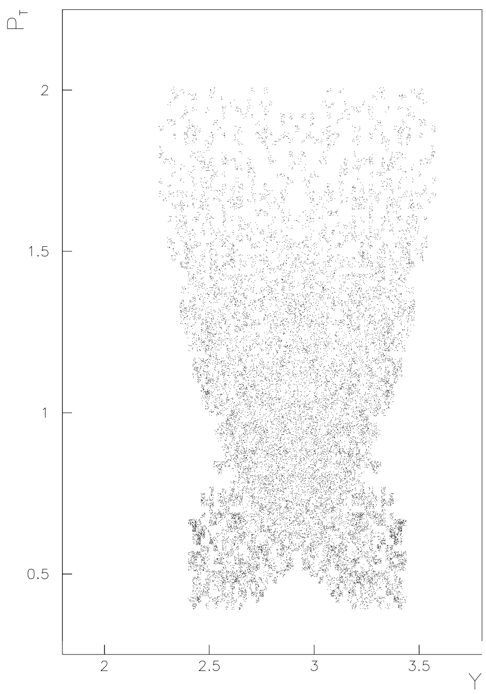

Figure 6.5: p_T versus rapidity in the lab system, for weighted Λ events from the WA97 Pb-Pb data, reflected about mid-rapidity because of the symmetry of Pb-Pb collisions in the centre-of-mass frame.

6.4.1 The Calculation of Yields

After the data have been extrapolated, the total number of particles of each species that were produced in the interactions is known. The particle yield per interaction is then calculated from the formula

$$\textit{yield per interaction} = \textit{sum of weights} \ / \ (\textit{branching ratio} \times \textit{number of interactions})$$

where the respective branching ratios account for unseen decay modes, and the number of interactions is worked out from the number of good events triggered on. It also contains a factor that accounts for the thickness of the target in interaction lengths (so that Pb beam data with a 1% target can be compared with proton beam data with an 8% target).

The final yields contain a further factor of $\frac{1}{0.78}$ (the inverse of the beam reconstruction efficiency), to account for events which were not used for weighting because the beam was not reconstructed and, therefore, no vertex could be found. The efficiency of the relative triggers was also checked using Monte Carlo and normalised to the Pb-Pb data to ensure that no bias was caused due to the different triggers and set-ups used in different experimental runs.

6.4.2 Feed-Down Corrections

One final factor that must be considered when calculating hyperon yields is the feed-down correction from cascade decays. Feed-down is the name used to describe the contamination of Λs or $\overline{\Lambda}$s from cascade decays or, in the case of the Ξ^- or $\overline{\Xi}^+$, contamination due to an Ω^- or $\overline{\Omega}^+$ decaying into a Ξ^- or $\overline{\Xi}^+$ respectively. For example, it is quite possible that a Λ particle from a Ξ^- or Ω^- decay could have a momentum four-vector such that it satisfies all of the cuts required for a gold-plated Λ. Since the Λ was not in fact a true Λ from the target, however, its inclusion in any further analysis represents contamination due to one type of feed-down decay. This is shown pictorially in figure 6.6. Fortunately, feed-down correction is less of a problem for the WA97 geometry than it is for other experiments which have detectors situated much further from the target. The data shown in the following plots and tables have not been corrected for feed-down decays, but within the experiment's geometry such corrections are expected to be of minor importance. The feed-down for both Ξ^- and $\overline{\Xi}^+$ from Ω decays is estimated to be less than 2%. The feed-down of Λs from Ξ^- and Ξ^0 decays is estimated to be less than 5% and the feed-down of $\overline{\Lambda}$s from $\overline{\Xi}^+$ and $\overline{\Xi}^0$ decays is estimated to be less than 10% [51].

6.4.3 Final Yield Values

The final yields per interaction for the various hyperon species were calculated as a function of the number of nucleons participating in the collision. For the Pb-Pb data, the

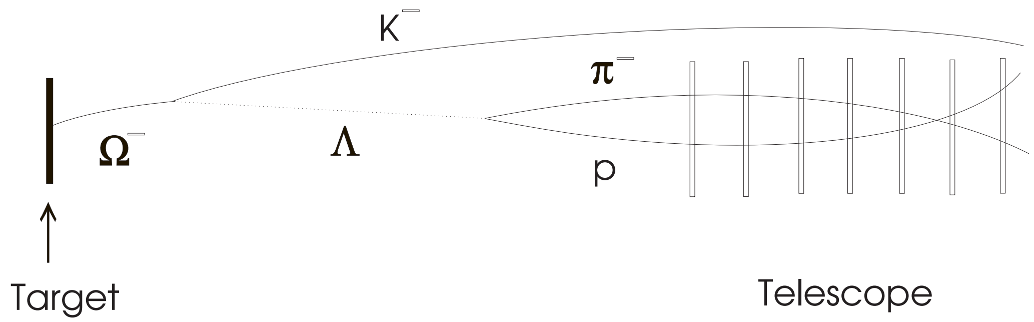

Figure 6.6: An example of how feed-down occurs.

number of participants is calculated using a Glauber model fit to the corrected multiplicity spectrum [52] coming from the multiplicity μ-strips which are situated just behind the target. The multiplicity seen by the multiplicity μ-strips is approximately 30-35% of the particles produced. The corrected multiplicity spectrum, with the fit superimposed, is shown in figure 6.7. This fit assumes that the number of participants is proportional to the multiplicity. For the proton beam data, the number of participants is calculated by averaging over all possible impact parameters.

Figure 6.8 shows the yields of Λs, Ξs and Ωs for the p-Be, p-Pb and Pb-Pb data versus the number of participants [53]. The yields re-scaled so that the p-Be value is 1 are shown in the second part of this figure. The solid line has a gradient of one and, therefore, shows where data would be expected to lie if the yields were simply proportional to the number of participants. Although this appears to be the case for the p-Be and p-Pb data, the

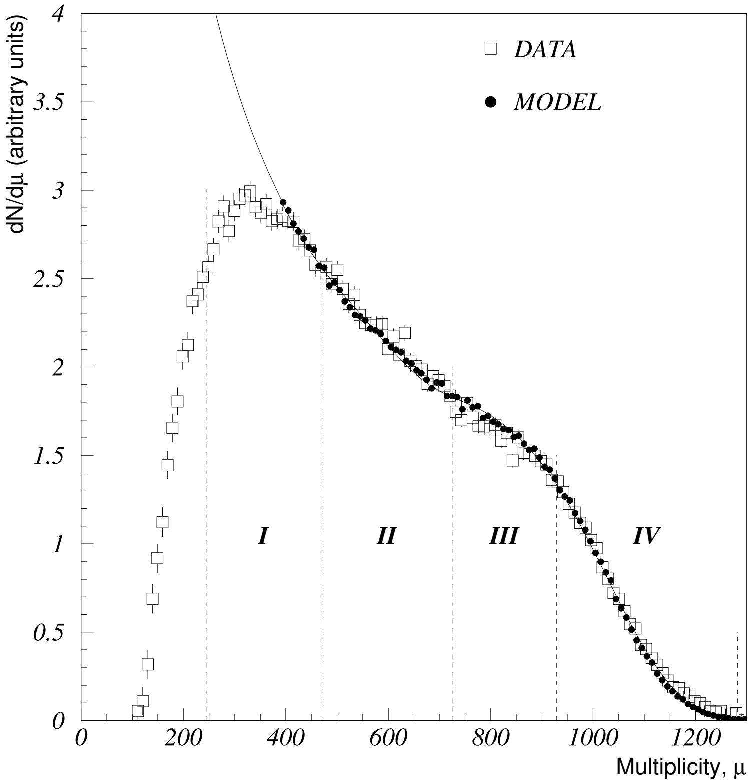

Figure 6.7: The distribution of particle multiplicity from the Pb-Pb data, with the Glauber model distribution superimposed in black dots.

Pb-Pb data shows a significant enhancement of all hyperon species and, in particular, that the enhancement follows a distinct hierarchy, such that it increases with the strangeness content of the particle. It is true that a considerable shift in the number of participants for the Pb data points would allow some of the Pb-Pb points to line up completely on this line. Such an effect would not, however, prevent the large enhancements seen in the production of the rarer strange particles with respect to those of lesser strangeness. Neither would it remove the distinct hierarchy which sees Ωs enhanced more than Ξs and Ξs enhanced more than Λs. The main conclusions from the data would, therefore, remain virtually unchanged. Figure 6.9 generalises this plot to include negative hadrons (h^-), and also shows the various hyperon yields separated in particle and anti-particle respectively. While not described in detail in this thesis, cuts to select gold-plated K^0s are in many ways similar to the cuts chosen for Λ and $\overline{\Lambda}$ selection except that one concentrates on the α Armenteros range $|\alpha| < 0.45$ where K^0s are unambiguous from Λs and $\overline{\Lambda}$s. Kaons are the lightest mesons that contain a strange quark and, since mesons are much easier to form than baryons, they provide a useful measure of overall strange quark production in the collision. They are the most abundantly produced of the strange particles. For negatives, one only requires that a reconstructed track comes from the target region (and, of course, that its charge has the correct sign). Negatives are interesting because they are related to the overall multiplicity (ie. number of tracks), and hence to the overall particle production in the collision. Negatives are chosen rather than positives due to the fact that the colliding ions already have a net positive charge, even before extra particles get produced. The negative hadrons also tend to be composed mostly of pions while the positives contain some contamination from protons. The numerical values of the yields in figure 6.9 are shown in tables 6.6 and 6.7.

Table 6.6: Numerical values for the yields shown in figure 6.9.

	p-Be ($N_{part} = 2.5$)	p-Pb ($N_{part} = 4.75$)	Pb-Pb bin1($N_{part} = 120$)
h^-	0.88 ± 0.02	1.26 ± 0.19	60.3 ± 5.0
K^0	-	0.098 ± 0.004	7.7 ± 0.8
Λ	0.0334 ± 0.0006	0.060 ± 0.002	5.1 ± 0.3
$\overline{\Lambda}$	0.0111 ± 0.0002	0.015 ± 0.001	0.71 ± 0.07
Ξ^-	0.0015 ± 0.0001	0.0030 ± 0.0002	0.45 ± 0.03
$\overline{\Xi}^+$	0.00068 ± 0.0001	0.0012 ± 0.0001	0.13 ± 0.02
$\Omega^- + \overline{\Omega}^+$	0.00016 ± 0.00006	0.000263 ± 0.000078	0.13 ± 0.02

In order to view the observed enhancement more clearly, the normalised yields can be divided by the number of participants - in which case the solid line in figure 6.8 maps onto a flat line at yield per participant = 1. This plot is shown in figure 6.10. It can be seen that while the p-Be and p-Pb points appear consistent with a yield per participant of 1, the enhancement of $\Xi^- + \overline{\Xi}^+$ in Pb-Pb is by a factor of 5, and for Ωs it exceeds an order of magnitude.

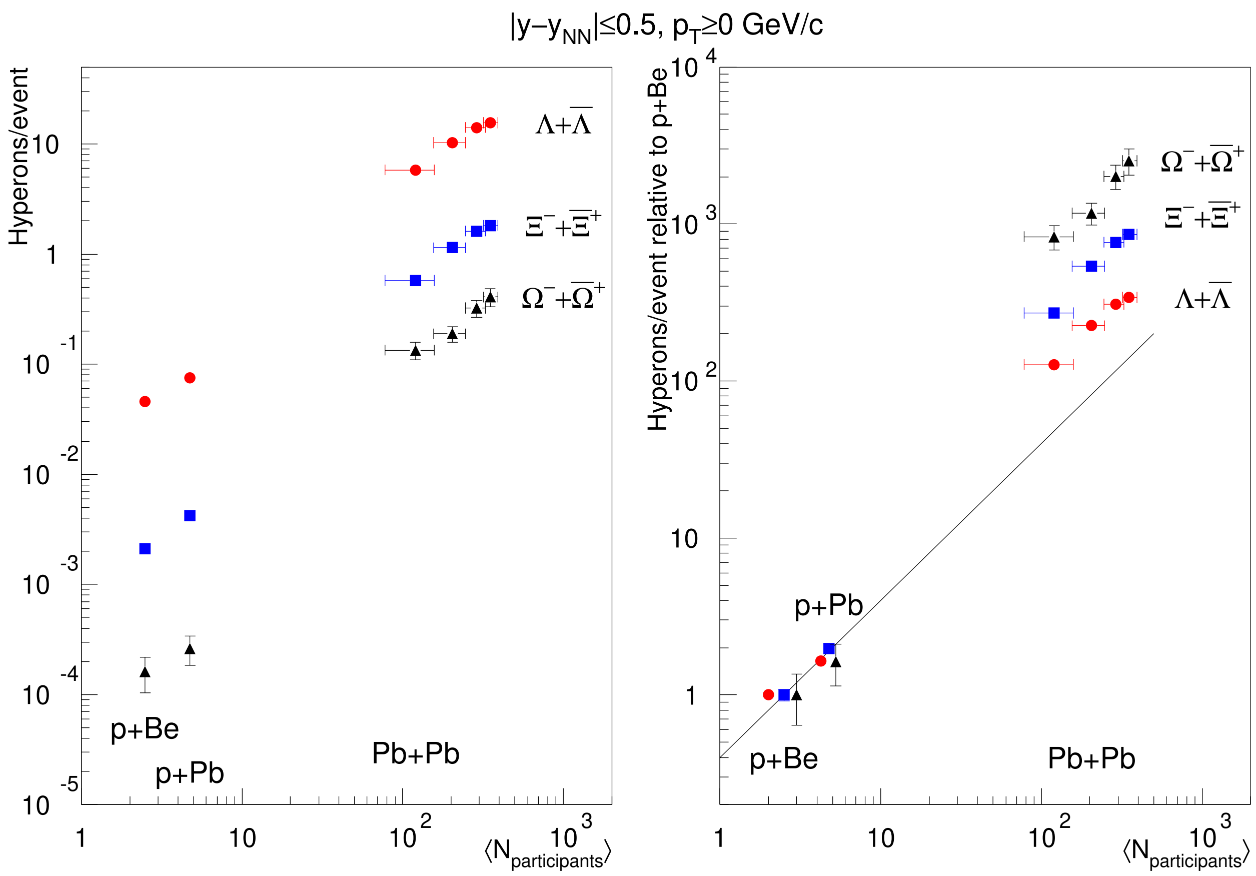

Figure 6.8: Hyperon yields per interaction (left), and hyperon yields per interaction rescaled so that the p-Be value is 1 (right).

6.5 Comparison with Other Experiments

Hyperon yields are at present fairly scarce in other heavy ion experiments, perhaps not surprisingly since many of them study signatures other than strangeness enhancement. Results on inverse slopes are much more common, however, with WA97's two predecessors, WA85 [54] and WA94 [55], forming a useful comparison. Table 6.8 summarises the results found by these two collaborations in p-S, S-S, p-W, and S-W interactions respectively [56]. It can be seen that, once again, the inverse slopes seem to increase with increasing size of the collision system, and at the lower end of the scale compare favourably to what Hagedorn found for nucleon-nucleon systems [57, 58]. Hagedorn found that N-N scattering

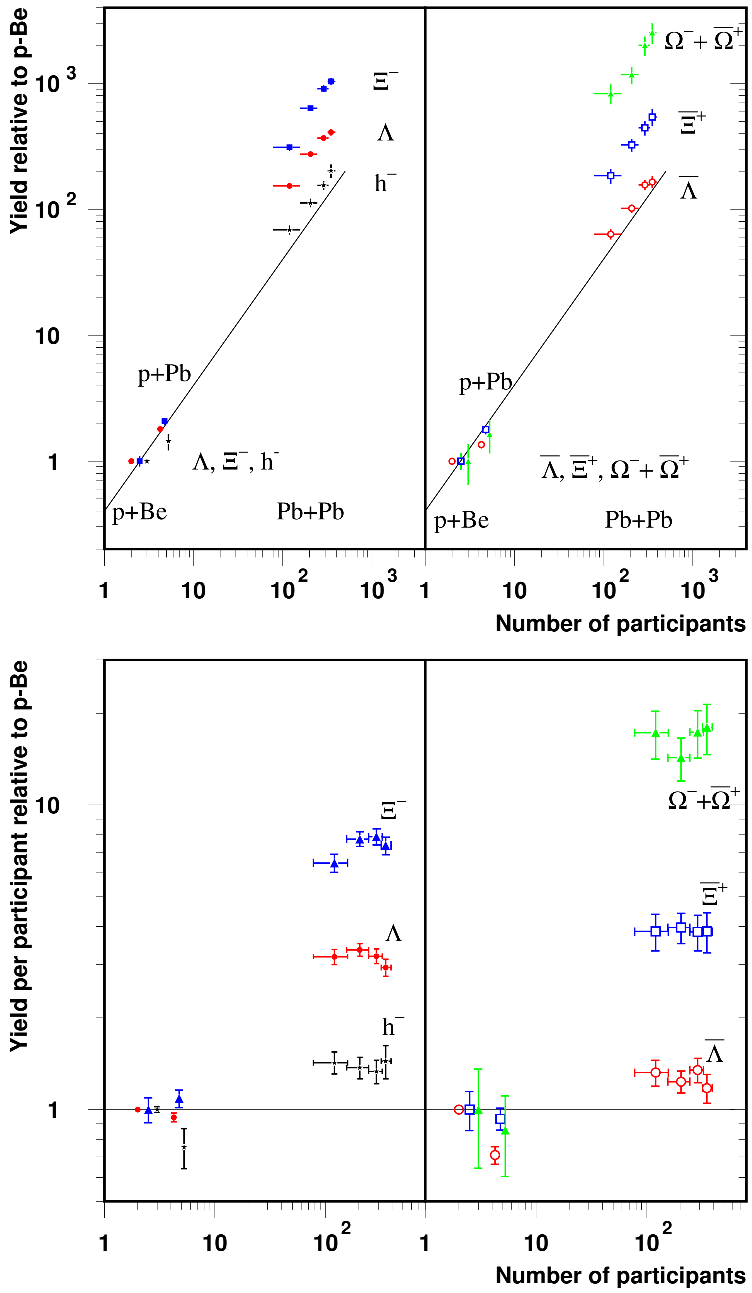

Figure 6.9: Hyperon yields per interaction for negative hadrons, Λ, $\overline{\Lambda}$, Ξ^-, $\overline{\Xi}^+$, Ω^-, and $\overline{\Omega}^+$.

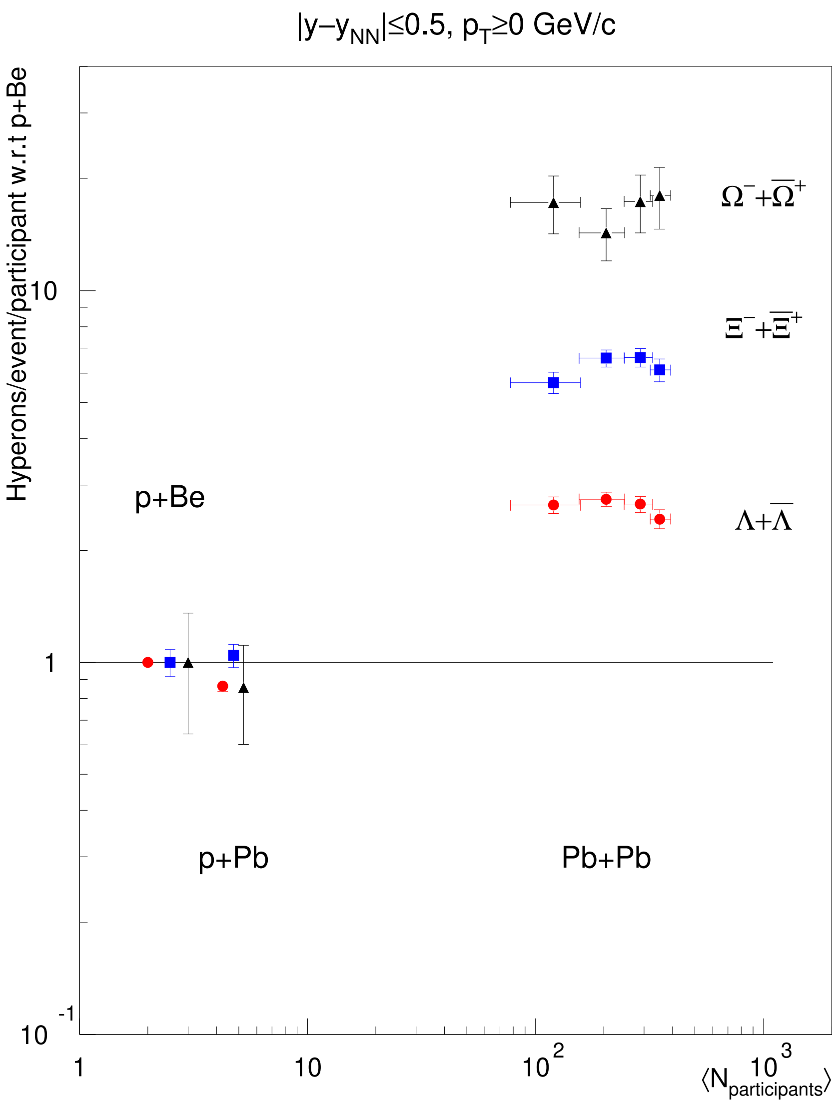

Figure 6.10: Hyperon yields per interaction, divided by the number of participants and re-scaled so that the p-Be value is 1.

Table 6.7: Numerical values for the yields shown in figure 6.9.

	Pb-Pb bin2($N_{part}=205$)	Pb-Pb bin3($N_{part}=289$)	Pb-Pb bin4($N_{part}=351$)
h^-	99.0 $\pm$ 8.0	136.0 $\pm$ 12.0	178.0 $\pm$ 22.0
K^0	14.5 $\pm$ 1.1	20.8 $\pm$ 1.8	21.9 $\pm$ 2.4
Λ	9.1 $\pm$ 0.4	12.3 $\pm$ 0.7	13.7 $\pm$ 0.9
$\overline{\Lambda}$	1.13 $\pm$ 0.09	1.7 $\pm$ 0.2	1.8 $\pm$ 0.2
Ξ^-	0.92 $\pm$ 0.05	1.32 $\pm$ 0.08	1.5 $\pm$ 0.1
$\overline{\Xi}^+$	0.22 $\pm$ 0.03	0.30 $\pm$ 0.04	0.37 $\pm$ 0.06
$\Omega^- + \overline{\Omega}^+$	0.19 $\pm$ 0.03	0.32 $\pm$ 0.06	0.41 $\pm$ 0.08

behaved like a system in apparent thermal equilibrium at around 150-180 MeV which is in good agreement with the results for proton induced interactions on light nuclei (such as the WA97 p-Be). It can also be seen that p-W and p-S inverses slopes from the WA85 and WA94 collaborations compare favourably to those found by WA97 for p-Pb interactions.

Table 6.8: Inverse slopes (in units of MeV) found by the WA85 and WA94 collaborations (all values quoted are with $\alpha = \frac{3}{2}$).

	WA85		WA94	
	p-W	S-W	p-S	S-S
h^-	196 $\pm$ 21	235 $\pm$ 5	-	-
K^0	-	219 $\pm$ 5	-	-
Λ	197 $\pm$ 2	233 $\pm$ 3	191 $\pm$ 3	213 $\pm$ 3
$\overline{\Lambda}$	185 $\pm$ 5	232 $\pm$ 7	181 $\pm$ 5	204 $\pm$ 5
Ξ^-	211 $\pm$ 14	244 $\pm$ 12	212 $\pm$ 9	222 $\pm$ 10
$\overline{\Xi}^+$	216 $\pm$ 21	238 $\pm$ 16	202 $\pm$ 12	208 $\pm$ 13

6.6 Outlook for Heavy Ion Physics

Since November 1994, the CERN fixed target experiments have had access to lead ion beams from the SPS. Using these beams of truly heavy ions, combined with new silicon pixel technology, the WA97 experiment has been able to continue the work and progress made by its predecessors and is able to reconstruct and study large numbers of the triply-strange Ω^- and $\overline{\Omega}^+$ particles. While evidence for strangeness enhancement in these heavy ion collisions appears to be both strong and convincing, perhaps the most intriguing question posed by this observation is when does this effect of strangeness enhancement switch on?

The NA57 experiment, which is currently taking data, is working to probe the region of intermediate number of participants by looking at more peripheral Pb-Pb collisions. The experiment will also run with a much lower beam momentum of 40 GeV/c per nucleon, to see whether the observed strangeness enhancement switches off with a reduced centre of mass energy of the collision system.

As far as the short term future is concerned, the STAR [59] and PHENIX [60] experiments at the Relativistic Heavy Ion Collider (RHIC) at Brookhaven will shortly begin taking data. Unlike previous heavy ion experiments, RHIC will make use of two colliding beams of gold ions rather than a beam on fixed target. The STAR experiment is designed to look for mainly hadronic signals while PHENIX will concentrate more on J/Ψ suppression and direct photon production. One powerful feature of RHIC is that the beam energy can be varied considerably, which means that points all over the QCD phase space diagram can be explored.

In the longer term, the future ALICE experiment [12] at the Large Hadron Collider at CERN plans to use colliding beams of lead ions, and also aims to cover the full 2π in azimuthal angle, and greater than 45 degrees either side of the beam. The proposed layout of the ALICE experiment is shown in figure 6.11. The ALICE experiment is the first heavy ion experiment that aims to look at a multitude of the proposed QGP signatures in a single experiment, including a number of studies on an event-by-event basis. It is interesting to look at some of the projected invariant mass distributions that come from the ALICE Monte Carlo because these show the number of events that should be required to resolve signals for the various hyperon species. A sample plot from this Monte Carlo is shown in figure 6.12. It can be seen that even after a single event a K^0 peak is visible from the background, and only 10 events are required to identify a reasonable Λ peak. Of course the multi-strange particles such as Ξs and Ωs take many more events to resolve, but it is still clear that large statistics of even rare particles such as the Ω will be available. As well as looking at charmonium supression of the J/Ψ and Ψ' states, ALICE should also be able to look at supression of the Υ, Υ', and Υ'' states. The fact that these states have much smaller bound state radii than the J/Ψ means that searching for suppression of these states will provide information on the strength of the colour field. The prediction is that ALICE will look at the high temperature and low baryon density region of the QCD phase diagram and, since this is predicted to produce much higher yields of direct photons, ALICE also intends to look at the thermal photon signal from these interactions. The conditions of temperature and baryon density that should be formed in the ALICE experiment should be much closer to the conditions that existed during the early Universe than can be reached with current experiments at the SPS.

6.7 Conclusions

While multi-strange particle yields in p-Be and p-Pb data appear to follow simple scaling with the number of participants, the yields found in central Pb-Pb collisions increase much faster than expected from direct proportionality with N_{part}. Moreover, the enhancement increases with the strangeness content of the particle and is greater than an order of magnitude for the Ω. While such enhancements are difficult to explain purely in terms of hadronic models they could, however, be explained by QGP models. This seems to indicate that the WA97 experiment is probing into the area of QGP mixed phase on the QCD phase diagram. If the theoretical predictions are accurate, then the forthcoming heavy

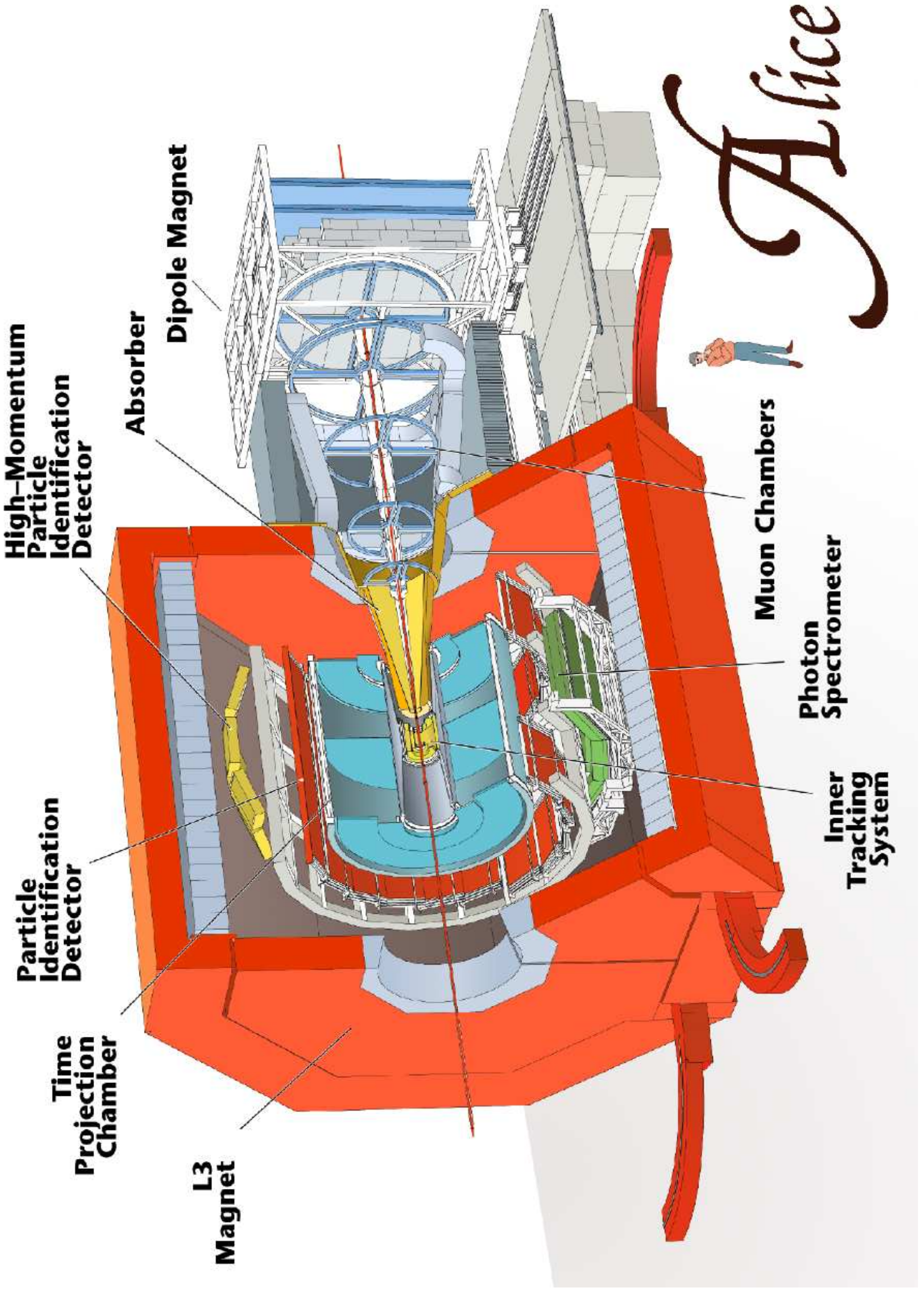

Figure 6.11: Layout of the future ALICE experiment.

ions experiments at RHIC and the CERN LHC should allow for a thorough investigation into the properties of the QGP phase of matter that existed near the very beginning of our Universe.

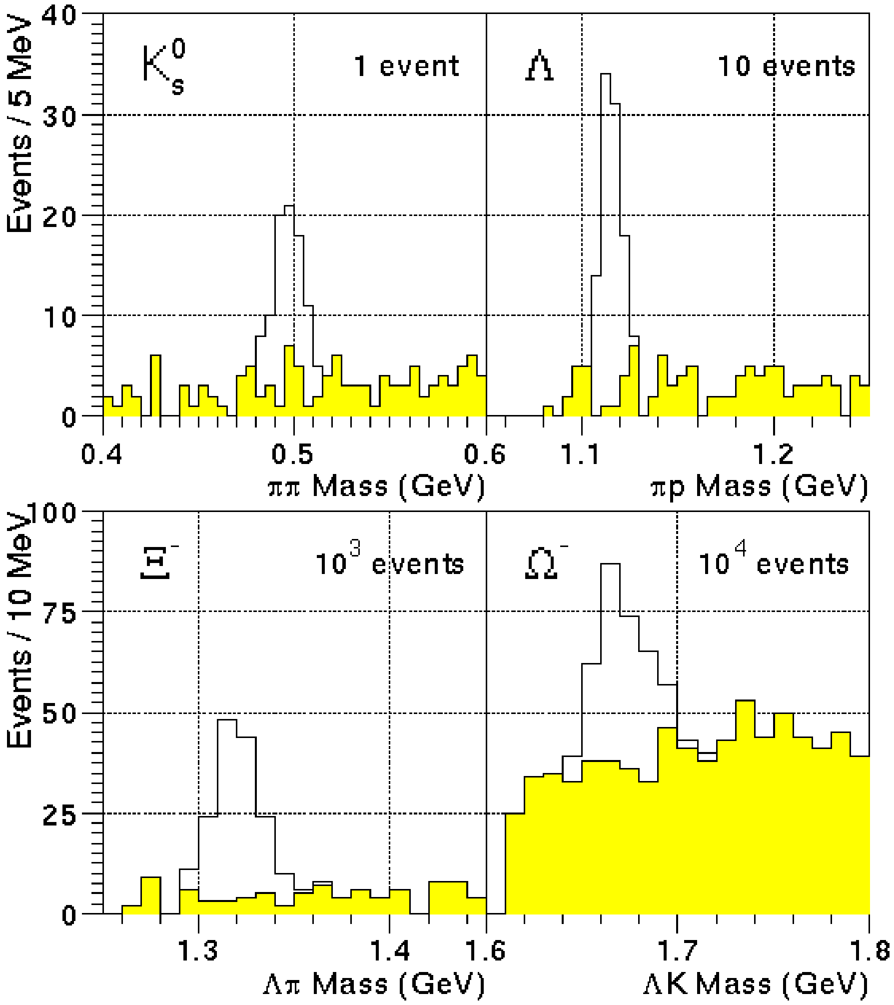

Figure 6.12: Effective mass distributions for different numbers of events from ALICE Monte Carlo studies.

Appendix A

Armenteros-Podolanski Plots

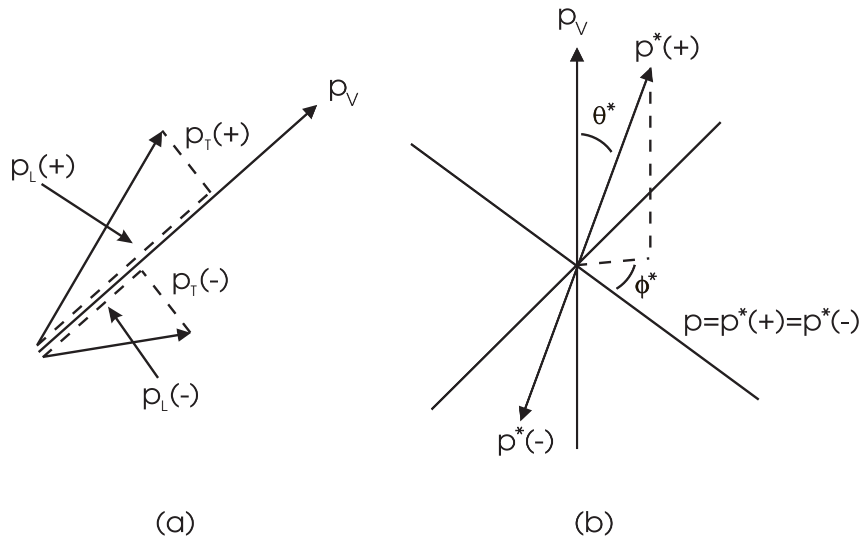

Figure A.1: Schematic representation of a V^0 decay in a) the lab frame, and b) the V^0's centre-of-mass frame.

Figure A.1 (a) illustrates a V^0 decay into a positive and negative particle. The tracks have longitudinal momentum components $p_L(+)$ and $p_L(-)$ and transverse momentum components $p_T(+)$ and $p_T(-)$ with respect to the V^0's direction of motion. Note that in the case of cascades, the formalism is the same except that one simply substitutes a charged track with a neutral track in the formulae. In the centre-of-mass frame (as shown in figure A.1 (b)), the momentum components are

$$p_L^*(+) = p^* cos\theta,$$

$$p_T^*(+) = p^* sin\theta,$$

$$E^*(+) = \sqrt{p^{*^2} + m^2(+)}$$

To transform to the lab frame requires the use of Lorentz transformations, which in matrix form are given by

$$\begin{pmatrix} E \\ p_L \end{pmatrix} = \begin{pmatrix} \gamma & \gamma\beta \\ \gamma\beta & \gamma \end{pmatrix} \begin{pmatrix} E^* \\ p_L^* \end{pmatrix}, p_T^* = p_T$$

where $\gamma = 1/\sqrt{1-\beta^2}$, and β is the velocity of the lab in the particle's rest frame. This gives

$$E^{Lab}(+) = \gamma E^*(+) + \gamma\beta p_L^*(+)$$

$$p_L^{Lab}(+) = \gamma p_L^*(+) + \gamma\beta E^*(+) = \gamma p^* cos\theta^* + \gamma\beta E^*(+)$$

$$p_T^{Lab}(+) = p_T^*(+) = p^* sin\theta^*$$

i.e.

$$p_L^{Lab}(+) = \gamma p^* cos\theta^* + \gamma\beta E^*(+)$$

$$p_L^{Lab}(-) = -\gamma p^* cos\theta^* + \gamma\beta E^*(-)$$

therefore

$$p_L^{Lab}(+) - p_L^{Lab}(-) = 2\gamma p^* cos\theta^* + \beta\gamma(E^*(+) - E^*(-))$$

$$p_L^{Lab}(+) + p_L^{Lab}(-) = p_L^{Lab}(= p_{V^0}) = \beta\gamma m_V^0 \sim \gamma m_V^0$$

The Armenteros-Podolanski variable, α, is defined as

$$\alpha = \frac{p_L^{Lab}(+) - p_L^{Lab}(-)}{p_L^{Lab}(+) + p_L^{Lab}(-)} = \frac{2p^* cos\theta^*}{m_V^0} + \frac{E^*(+) - E^*(-)}{m_V^0} = \zeta cos\theta^* + \phi$$

with

$$\zeta = \frac{2p^*}{m_V^0}, \phi = \frac{E^*(+) - E^*(-)}{m_V^0}$$

therefore

$$cos\theta^* = \frac{\alpha - \phi}{\zeta} \qquad\qquad sin\theta^* = \frac{p_T^*}{p^*}$$

and

$$cos^2\theta^* + sin^2\theta^* = 1 = (\frac{\alpha - \phi}{\zeta})^2 + (\frac{p_T^*}{p^*})^2$$

This is the equation of an ellipse with centre (ϕ,0) and semi-axis of length ζ in α, and of length p^* in p_T. Table A.1 shows the value of these variables for the decays of Λs, $\overline{\Lambda}$s and K^0s, whilst the theoretical plots for Λs, $\overline{\Lambda}$s and K^0s are shown in figure A.2.

Table A.1: Armenteros-Podolanski quantities.

Decay	ζ	p^* (GeV/c)	α_{min}	α_{max}	ϕ
$K_s^0 \rightarrow \pi^+\pi^-$	0.8282	0.206	-0.828	+0.828	0.
$\Lambda \rightarrow p\pi^-$	0.179	0.101	+0.515	+0.873	0.694
$\overline{\Lambda} \rightarrow p\pi^+$	0.179	0.101	-0.873	-0.515	-0.694

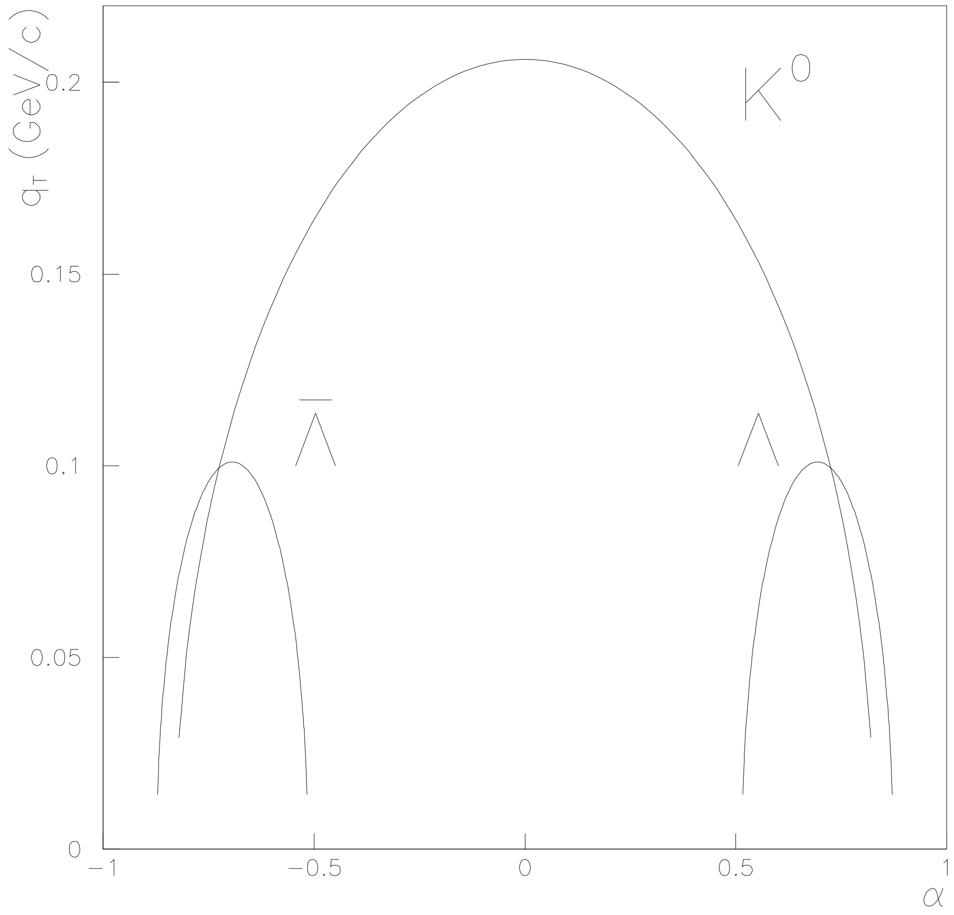

Figure A.2: Armenteros-Podolanski regions for different V^0 candidates.

Appendix B

Calculation of the Primary Vertex

In the xz (non-bend) plane the equation of the beam is defined as

$$z_{beam} = m_1 x_{beam} + c_1 \tag{B.1}$$

where m_1 and c_1 are the standard gradient and intercept of a straight line fit. The equation of the cascade (or indeed V^0) is likewise defined as

$$z_{cas} = m_2 x_{cas} + c_2 \tag{B.2}$$

where m_2 and c_2 represent the gradient and intercept that correspond to the cascade. Therefore, the intersection of the beam and cascade occurs at the x coordinate defined by

$$x_{int} = \frac{c_2 - c_1}{m_1 - m_2} \tag{B.3}$$

The z coordinate of the interaction point can then be found by substituting this definition of x_{int} into equation B.1 or B.2, like so

$$z_{int} = m_1 x_{int} + c_1 = m_2 x_{int} + c_2 \tag{B.4}$$

The circular equation of the beam is defined by the expression

$$(x_{beam} - x_0)^2 + (y_{beam} - y_0)^2 = R^2 \tag{B.5}$$

where x_0 and y_0 are the x and y coordinates at the centre of the circle, and R is its radius. Equation B.3 tells us the equation of $x_{beam} = x_{int}$ at the interaction point, so we want to be able to plug that into this equation and find the value of y_{beam}. Before this can be done, however, the values of x_0 and y_0 must first be determined. The WA97 beam telescope can give us information on two points of the circle at the beam reference planes (ie. we know two coordinates on the beam's path, (x_1,y_1) and (x_2,y_2)). This therefore gives us two simultaneous equations which we can solve for x_0 and y_0

$$(x_1 - x_0)^2 + (y_1 - y_0)^2 = R^2 \tag{B.6}$$

$$(x_2 - x_0)^2 + (y_2 - y_0)^2 = R^2 \tag{B.7}$$

Rearranging in terms of y_0, we obtain

$$y_0 = y_1 \pm \sqrt{R^2 - (x_1 - x_0)^2} = y_2 \pm \sqrt{R^2 - (x_2 - x_0)^2} \tag{B.8}$$

Plugging the second of these expressions into equation B.6 gives the formula

$$(x_1 - x_0)^2 + (y_1 - y_2 \pm \sqrt{R^2 - (x_2 - x_0)^2})^2 = R^2 \tag{B.9}$$

This only contains one unknown quantity (x_0), since the radius is fixed and determined by the momentum of the beam, which is a known quantity. For the next few stages of calculation, we will abreviate the expression $\sqrt{R^2 - (x_1 - x_0)^2}$ with a simple $\surd$. This formula must still be rearranged to give an expression in terms of x_0, however, so we then take equation B.9 and rearrange it to read

$$x_1^2 - 2x_1x_0 + (y_1 - y_2)^2 - x_2^2 + 2x_2x_0 \pm 2(y_1 - y_2)\surd = 0 \tag{B.10}$$

Doing a little further rearrangement gives

$$2(x_2 - x_1)x_0 + (x_1^2 - x_2^2) + (y_1 - y_2)^2 = \mp 2(y_1 - y_2)\surd \tag{B.11}$$

We can then simplify this expression by making the following definitions

$$\alpha = 2(x_2 - x_1)$$

$$\beta = (x_1^2 - x_2^2) + (y_1 - y_2)^2$$

$$\gamma = 2(y_1 - y_2)$$

in which case the equation takes the much simpler looking form

$$\alpha x_0 + \beta = \mp\gamma\sqrt{} \tag{B.12}$$

Squaring both sides gives

$$\alpha^2 x_0^2 + 2\alpha\beta x_0 + \beta^2 = \gamma^2(R^2 - (x_2 - x_0)^2) \tag{B.13}$$

which then simplifies to

$$(\alpha^2 + \gamma^2)x_0^2 + 2(\alpha\beta - \gamma^2 x_2)x_0 + \beta^2 + \gamma^2(x_2^2 - R^2) = 0 \tag{B.14}$$

By making the definitions

$$a = \alpha^2 + \gamma^2$$

$$b = 2(\alpha\beta - \gamma^2 x_2)$$

$$c = \beta^2 + \gamma^2(x_2^2 - R^2)$$

this then reduces to a standard quadratic equation of the form

$$ax_0^2 + bx_0 + c = 0 \tag{B.15}$$

which, of course, has the solution

$$x_0 = \frac{-b \pm \sqrt{b^2 - 4ac}}{2a} \tag{B.16}$$

Therefore, we can solve for x_0. The value of y_0 can then be found by plugging the value of x_0 back into equation B.8. Note that because the expressions for both x_0 and y_0 have plus or minus square roots in them, there are two possible values of both x_0 and y_0. The physical interpretation of these two roots is that they correspond to two possible circles (both of radius R) which pass through the two fixed points we have in the beam telescope. This is shown pictorially in figure B.1(a). We know which solution to take, of course, because we know which way the beam will be curving due to the magnetic field. Once the equation of the beam is completely defined, the only remaining step is to calculate y_{int} by plugging x_{int} into the now fully defined beam equation, so that we have

$$y_{int} = y_0 \pm \sqrt{R^2 - (x_{int} - x_0)^2} \tag{B.17}$$

where, again, we know which solution to take because we know from the beam curvature whether the true solution lies on the positive or negative side of the circle's centre point (this is shown in figure B.1(b)).

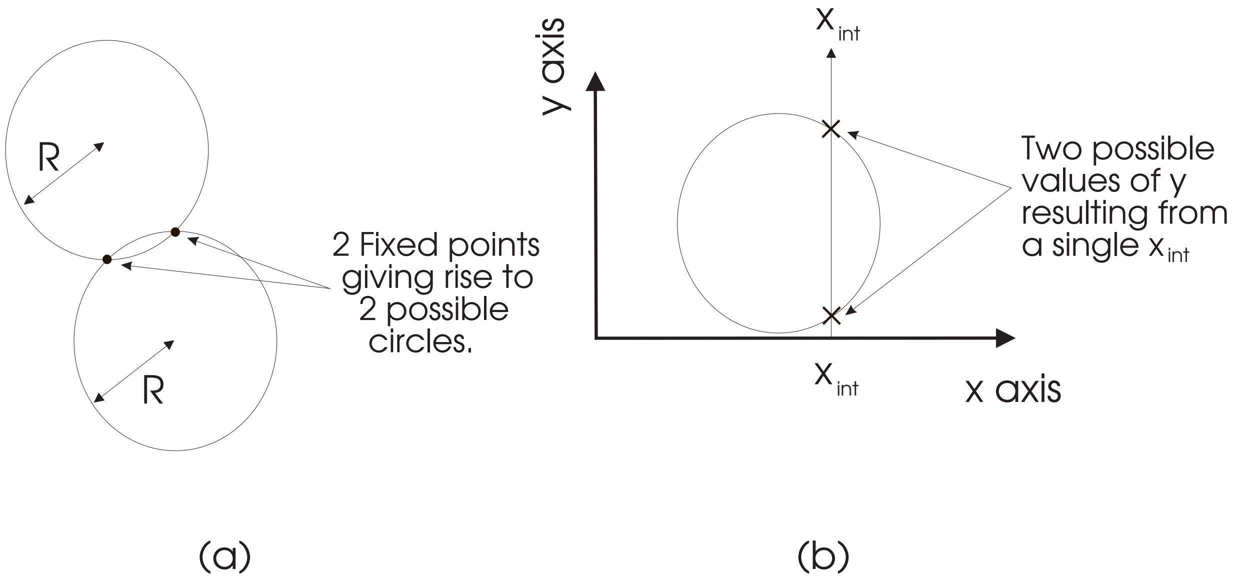

Figure B.1: How the two roots correspond to circles curving in different directions (a), and how two points on the circle lie at a given x position (b).

Appendix C

Calculation of Acceptance Windows

While the straight line maxima and minima cuts on p_T and rapidity that define the various acceptance windows are relatively easy to select, the curving contours that are related to the angle of inclination of the telescope are much less simplistic. In terms of the total momentum, p, we can define the longitudinal and transverse momentum components as

$$p_T = psin\theta \tag{C.1}$$

$$p_L = pcos\theta \tag{C.2}$$

We can then express the rapidity as

$$y = \frac{1}{2}ln(\frac{E + p_L}{E - p_L}) = \frac{1}{2}ln(\frac{E + pcos\theta}{E - pcos\theta}) \tag{C.3}$$

This gives us expressions for both p_T and y in terms of the overall momentum, p. What we now want to do, is write p_T itself in terms of the rapidity, y, and the angle, θ. We first concentrate on the formula

$$sinh(y) = \frac{e^y - e^{-y}}{2} \tag{C.4}$$

and since

$$y = \frac{1}{2}ln(\frac{E + p_L}{E - p_L}) \tag{C.5}$$

we can use

$$e^{ab} = (e^b)^a \tag{C.6}$$

to write this as

$$sinh(y) = \frac{1}{2}[(\frac{E + p_L}{E - p_L})^{\frac{1}{2}} - (\frac{E + p_L}{E - p_L})^{-\frac{1}{2}}] \tag{C.7}$$

which, with a little rearrangement gives

$$sinh(y) = \frac{p_L}{\sqrt{E + p_L}\sqrt{E - p_L}} = \frac{p_L}{\sqrt{E^2 - p_L^2}} \tag{C.8}$$

therefore

$$pcos\theta = p_L = \sqrt{E^2 - p_L^2} sinh(y) \tag{C.9}$$

We can then use the formula

$$E^2 - p_L^2 = m^2 + p_T^2 \tag{C.10}$$

to write this as

$$pcos\theta = \sqrt{m^2 + p^2 sin^2\theta} sinh(y) \tag{C.11}$$

Squaring both sides gives

$$p^2 cos^2\theta = (m^2 + p^2 sin^2\theta) sinh^2(y) \tag{C.12}$$

Collecting p^2 terms on the left, we have

$$p^2(cos^2\theta - sin^2\theta sinh^2(y)) = m^2 sinh^2(y) \tag{C.13}$$

Which allows us to finally write p in terms of y and θ, as

$$p = \sqrt{\frac{m^2 sinh^2(y)}{cos^2\theta - sin^2\theta sinh^2(y)}} \tag{C.14}$$

Using equation C.1 we then write p_T in terms of y and θ

$$p_T = \sqrt{\frac{m^2 sinh^2(y)}{cos^2\theta - sin^2\theta sinh^2(y)}} sin\theta \tag{C.15}$$

Which is the equation followed by the curving contours in the p_T vs. y acceptance region plots of Chapter 6.

Bibliography

[1] B. Müller, *The Physics of the Quark Gluon Plasma*, Springer-Verlag, (1985).

[2] L. van Hove, *Quark Gluon Plasma and Multiparticle Production*, CERN-TH 5236/88.

[3] R. P. Feynman, *Quantum Electrodynamics*, Addison-Wesley Publishing Company, Third Edition (1987) 291-297.

[4] F. Halzen and A. D. Martin, *Quarks and Leptons: An Introductory Course in Modern Particle Physics*, John Wiley and Sons (1984).

[5] D.H. Perkins, *Introduction to High Energy Physics*, Addison-Wesley Publishing Company, Third Edition (1987) 291-297.

[6] D. J. Gross and F. Wilczek, Phys. Rev. D **8**, (1973) 3633.

[7] J. Rafelski and B. Müller, Phys. Rev. Lett. **48** (1982) 1066.

[8] J. Rafelski and B. Müller, Phys. Rev. Lett. **56** (1986) 2334.

[9] Dr D.C. Dunbar, Dr J. Forshaw, Dr E.W.N. Glover and Dr T.R. Morris, *Proceedings of the School for Young High Energy Physicists*, RAL-TR-1998-023, March 1998.

[10] WA97 Collaboration: G. Alexeev, *et al.*, Nucl. Phys. **A590** (1995) 139c.

[11] NA57 Proposal, CERN/SPSLC/96-40 SPSLC/P300. 1996.

[12] ALICE - Technical Proposal for A Large Ion Collider Experiment at the CERN LHC, CERN/LHCC/95-71, December 1995.

[13] U. Heinz, Nucl. Phys. **A566** (1994) 205c.

[14] P. Koch. J. Müller and J. Rafelski, Phys. Rep. **142** (1986) 167.

[15] M. Jacob, *In Search of Quark Matter*, CERN-TH 7343/94.

[16] CERN preprint CERN-EP/99-29 (WA97 collaboration), to be published in Physics Letters B.

[17] *Production of multi-strange particles in Pb-Pb interactions at 158 A GeV/c*, Presented by A.K. Holme for the WA97 collaboration. Contribution to proceedings of International Symposium on Strangeness in Quark Matter, 14-18 April 1997, Thera (Santorini), Greece.

[18] *Strange Baryon Production in Pb-Pb Collisions at 158 A GeV/c*, Presented by A. Jacholkowski for the WA97 collaboration. Contribution to proceedings of International Europhysics Conference on High Energy Physics, 19-26 August 1997, Jerusalem, Israel.

[19] Thesis of M. Venables, *Hyperon Production in Proton-Sulphur Interactions at 200 GeV/c at the CERN OMEGA Spectrometer*, The University of Birmingham (1997).

[20] T. Matsui and H. Satz, Phys. Lett. **178B** (1986) 416.

[21] S. Ramos (NA38 Coll.), Nucl. Phys. **A590** (1995) 117c-126c.

[22] M. C. Abreu *et al.*, Nucl. Phys. **A610** (1996) 404c-417c.

[23] C. Gerschel and J. Hüfner, Z. Phys. **C56** (1992) 71.

[24] T. C. Awes (WA80 Coll.), Nucl. Phys. **A590** (1995) 81c-92c.

[25] P. Wurm, Nucl. Phys. **A590** (1995) 103c-116c.

[26] R. Albrecht *et al.*, Z. Phys. **C51** (1991) 1.

[27] M. Masera (HELIOS Coll.), Nucl. Phys. **A590** (1995) 93c-102c.

[28] NA45 technical proposals, SPSC/CERN/88-25, SPSC/P237; CERN/SPSC/94-01.

[29] J. Letessier, A. Tounsi, U. Heinz, J. Sollfrank and J. Rafelski, Phys. Rev. Lett. **70** (1993) 3530.

[30] CERN EMU05 Collaboration.

[31] G. L. Shaw, M. Shin, R. Dalitz and M. Desai, Nature Vol. **377** (1987) 436.

[32] B. S. Kumar, Nucl. Phys. **A590** (1995) 29c-46c.

[33] E.Witten, Phys. Rev. Lett. **71** (1993), 332

[34] E. Fahri and R. L. Jaffe, Phys. Rev. D **30** (1984), 2379.

[35] WA85 Collaboration: S. Abatzis *et al.*, Nucl. Phys. **A590** (1995) 307c-315c

[36] WA94 Collaboration: S. Abatzis *et al.*, Nucl. Phys. **A590** (1995) 317c-331c

[37] F. Antinori *et al.*, Nucl. Phys. **A590** (1995) 139c-146c.

[38] E.H.M. Heijne *et al.*, Nucl. Instr. Meth. **A349** (1994) 138

[39] F. Antinori *et al.*, Nucl. Instr. Meth. **A360** (1995) 91.

[40] *A new VME trigger processor for the NA57 experiment*, Presented by O. Villalobos Baillie for the NA57 collaboration. Contribution to proceedings of the Third Workshop on Electronics for LHC Experiments, London, September 22-26, 1997.

[41] H. Grote and I. McLaren, *EPIO User's Guide*, CERN Program Library (1993).

[42] J.-C. Lassalle *et al., TRIDENT User's Manual*, DD/EE/79-2.

[43] ORHION Documentation and Software notes, WA97 experiment.

[44] Thesis of R. P. Barnes, *Production of Strange and Multistrange Baryons in Ultra-Relativistic Heavy Ion Collisions*, The University of Birmingham (1993).

[45] *NAGLIB Manual FORTRAN Mark 13 Volume 4*, NAGLIB (1988).

[46] J. Podolanski and R. Armenteros, Phil. Mag **45** (1954) 13.

[47] Particle Data Group, *July 1998 Particle Physics Booklet*, extracted from the *Review of Particle Physics* C. Caso *et al.*, The European Physical Journal **C3** (1998) 1.

[48] R. L. Jaffe, Phys. Rev. Lett. **38** (1977), 195.

[49] A. Jacholkowski et al.: Di-V0 events in Pb-Pb collisions at 158 A GeV/c, J.Phys. G: Nucl.Part.Phys. **25** (1998) 423.

[50] D. Evans, in *International Symposium on Strangeness and Quark Matter*, World Scientific Publishing Co. Pte. Ltd., (1995) 91-109.

[51] E. Andersen *et al.* (WA97 Coll.), CERN Preprint CERN-EP/99-29, to be published in Phys. Lett. B.

[52] *Λ, Ξ and Ω production in Pb-Pb and p-Pb interactions at 158 A GeV/c*, Presented by R. Caliandro for the WA97 collaboration. Contribution to proceedings of the XXXIIIth Recontres de Moriond, Les Arcs 1800, France, 21-28 March 1998.

[53] *Multi-strange particle production in p-Be, p-Pb, and Pb-Pb collisions at 158 A GeV/c*, Presented by P. I. Norman for the WA97 collaboration. Contribution to proceedings of the XXXIVth Recontres de Moriond, Les Arcs 1800, France, 20-27 March 1999.

[54] S. Abatzis *et al.* (WA85 Coll.), Phys. Lett. **B447** (1999) 178.

[55] S. Abatzis *et al.* (WA94 Coll.), Phys. Lett. **B400** (1997) 239.

[56] D. Evans, Acta Physica Slovaca, Vol. **47** No. 1 (1997), 35-52.

[57] R. Hagedorn, Suppl. Nuovo Cimento **3** (1965) 147.

[58] R. Hagedorn, Riv. Nuovo Cimento **6** (1983) 1.

[59] RHIC letter of intent for an experiment on Particle and Jet production at Midrapidity, The STAR collaboration, LBL reports 29651 and 31040.

[60] PHENIX conceptual design report: an experiment to be performed at the Brookhaven National Laboratory Relativistic Heavy Ion Collider, edited by Nagamiya, S., Aronson, S., Young, G., and Paffrath, L., publ. Upton, Brookhaven, N.Y. 1993.